



**NAVAL
POSTGRADUATE
SCHOOL**

MONTEREY, CALIFORNIA

THESIS

**QUANTIFYING ELECTROMAGNETIC WAVE
PROPAGATION ENVIRONMENT USING
MEASUREMENTS FROM A SMALL BUOY**

by

Andrew E. Sweeney

June 2017

Thesis Advisor:
Second Reader:

Qing Wang
Wendell Nuss

Approved for public release. Distribution is unlimited.

THIS PAGE INTENTIONALLY LEFT BLANK

REPORT DOCUMENTATION PAGE			<i>Form Approved OMB No. 0704-0188</i>
Public reporting burden for this collection of information is estimated to average 1 hour per response, including the time for reviewing instruction, searching existing data sources, gathering and maintaining the data needed, and completing and reviewing the collection of information. Send comments regarding this burden estimate or any other aspect of this collection of information, including suggestions for reducing this burden, to Washington headquarters Services, Directorate for Information Operations and Reports, 1215 Jefferson Davis Highway, Suite 1204, Arlington, VA 22202-4302, and to the Office of Management and Budget, Paperwork Reduction Project (0704-0188) Washington, DC 20503.			
1. AGENCY USE ONLY (Leave blank)	2. REPORT DATE June 2017	3. REPORT TYPE AND DATES COVERED Master's thesis	
4. TITLE AND SUBTITLE QUANTIFYING ELECTROMAGNETIC WAVE PROPAGATION ENVIRONMENT USING MEASUREMENTS FROM A SMALL BUOY		5. FUNDING NUMBERS	
6. AUTHOR(S) Andrew E. Sweeney			
7. PERFORMING ORGANIZATION NAME(S) AND ADDRESS(ES) Naval Postgraduate School Monterey, CA 93943-5000		8. PERFORMING ORGANIZATION REPORT NUMBER	
9. SPONSORING /MONITORING AGENCY NAME(S) AND ADDRESS(ES) N/A		10. SPONSORING / MONITORING AGENCY REPORT NUMBER	
11. SUPPLEMENTARY NOTES The views expressed in this thesis are those of the author and do not reflect the official policy or position of the Department of Defense or the U.S. Government. IRB number <u>N/A</u> .			
12a. DISTRIBUTION / AVAILABILITY STATEMENT Approved for public release. Distribution is unlimited.		12b. DISTRIBUTION CODE	
13. ABSTRACT (maximum 200 words) This thesis work is part of a major research effort, the Coupled Air Sea Processes and Electromagnetic (EM) ducting Research (CASPER), to understand air-sea interaction processes and their representation in prediction models in order to quantify abnormal propagations of EM signals through the atmosphere. This thesis work focuses on the evaluation of the measurements from a small buoy, the Marine Air-Sea Flux (MASFlux) buoy, for obtaining evaporation duct properties. MASFlux was deployed during CASPER-Pilot and CASPER-East field campaigns and was analyzed. This thesis demonstrated the measurement capability of MASFlux in revealing the near-surface gradient in scalars and wind together with atmospheric turbulence and surface waves in minimally disturbed marine environment. The use of the MASFlux measurements as input to a Monin-Obukhov Similarity Theory (MOST) evaporation duct model, such as the modified Coupled Ocean-Atmosphere Response Experiment (COARE) model, was systematically evaluated using both CASPER-Pilot and East datasets. Finally, the value of MASFlux measurements to reveal the near surface vertical profiles is demonstrated by employing data from multiple research platforms that provided concurrent/co-located data at different altitudes. This increased resolution at the air-sea interface provides greater accuracy for determining evaporation duct profiles, which is vital for producing accurate EM propagation models.			
14. SUBJECT TERMS evaporation duct, CASPER, modified refractivity, air-sea interaction			15. NUMBER OF PAGES 107
16. PRICE CODE			
17. SECURITY CLASSIFICATION OF REPORT Unclassified	18. SECURITY CLASSIFICATION OF THIS PAGE Unclassified	19. SECURITY CLASSIFICATION OF ABSTRACT Unclassified	20. LIMITATION OF ABSTRACT UU

THIS PAGE INTENTIONALLY LEFT BLANK

Approved for public release. Distribution is unlimited.

**QUANTIFYING ELECTROMAGNETIC WAVE PROPAGATION
ENVIRONMENT USING MEASUREMENTS FROM A SMALL BUOY**

Andrew E. Sweeney
Lieutenant, United States Navy
B.S., Florida State University, 2005

Submitted in partial fulfillment of the
requirements for the degree of

**MASTER OF SCIENCE IN METEOROLOGY
AND PHYSICAL OCEANOGRAPHY**

from the
NAVAL POSTGRADUATE SCHOOL
June 2017

Approved by: Qing Wang
 Thesis Advisor

Wendell Nuss
Second Reader

Wendell Nuss
Chair, Department of Meteorology

THIS PAGE INTENTIONALLY LEFT BLANK

ABSTRACT

This thesis work is part of a major research effort, the Coupled Air Sea Processes and Electromagnetic (EM) ducting Research (CASPER), to understand air-sea interaction processes and their representation in prediction models in order to quantify abnormal propagations of EM signals through the atmosphere. This thesis work focuses on the evaluation of the measurements from a small buoy, the Marine Air-Sea Flux (MASFlux) buoy, for obtaining evaporation duct properties. MASFlux was deployed during CASPER-Pilot and CASPER-East field campaigns and was analyzed. This thesis demonstrated the measurement capability of MASFlux in revealing the near-surface gradient in scalars and wind together with atmospheric turbulence and surface waves in minimally disturbed marine environment. The use of the MASFlux measurements as input to a Monin-Obukhov Similarity Theory (MOST) evaporation duct model, such as the modified Coupled Ocean-Atmosphere Response Experiment (COARE) model, was systematically evaluated using both CASPER-Pilot and East datasets. Finally, the value of MASFlux measurements to reveal the near surface vertical profiles is demonstrated by employing data from multiple research platforms that provided concurrent/co-located data at different altitudes. This increased resolution at the air-sea interface provides greater accuracy for determining evaporation duct profiles, which is vital for producing accurate EM propagation models.

THIS PAGE INTENTIONALLY LEFT BLANK

TABLE OF CONTENTS

I.	INTRODUCTION.....	1
A.	OVERVIEW	1
B.	SIGNIFICANCE OF THESIS WORK.....	2
C.	OBJECTIVES	3
D.	MILITARY APPLICATION.....	3
II.	BACKGROUND	5
A.	ATMOSPHERIC EFFECTS ON EM PROPAGATION.....	5
B.	EVAPORATION DUCT	8
C.	EVAPORATION DUCT MODELS.....	8
D.	MONIN-OBUKHOV SIMILARITY THEORY (MOST).....	9
E.	CASPER OVERVIEW	11
III.	DATA COLLECTION.....	13
A.	MASFLUX BUOY	13
B.	CASPER MASFLUX DEPLOYMENTS	17
1.	CASPER-Pilot	18
2.	CASPER-East.....	20
C.	SENSOR ACCURACY AND DATA QUALITY CONTROL	23
1.	Sensor Accuracy.....	23
2.	Data Quality Control	23
IV.	DATA ANALYSIS	25
A.	CASPER-PILOT.....	25
1.	Observed Near-Surface Variability.....	25
2.	MASFlux Measurements vs MOST Profiles	34
3.	Surface Flux, Evaporation Duct Properties, and SST Correction.....	49
B.	CASPER-EAST	56
1.	Gulf Stream and continental shelf analysis	56
2.	Ship and MASFlux Measurements vs. MOST Profiles over the Gulf Stream	65
3.	Vertical Profiles from Multiple Platform Measurements	80
V.	SUMMARY AND CONCLUSIONS	83
	LIST OF REFERENCES	85

INITIAL DISTRIBUTION LIST	89
--	-----------

LIST OF FIGURES

Figure 1.	Illustration of the Vertical Variation of Modified Refractivity, M in Different Ducting Conditions.	6
Figure 2.	The Four Categories for Atmospheric EM Propagation. Source: Turton et al. (1988)	7
Figure 3.	Schematic of the NPS MASFlux Buoy. Source: Alappattu (2017).	16
Figure 4.	An Example of the NPS MASFlux Buoy when Deployed During CASPER-East. Source: Alappattu (2017).....	17
Figure 5.	CASPER-Pilot Measurement Area.	19
Figure 6.	CASPER-East Measurement Area.....	21
Figure 7.	Locations of MASFlux deployments during CASTER-East.	22
Figure 8.	Temporal Variations of Air Temperature and Sea Temperature Measured by the MASFlux Buoy on April 26–27, 2015. (a) Original Data, (b) 2-Minute Low-Pass Filtered Data.....	25
Figure 9.	Temporal Variations of Air Temperature and Sea Temperature Difference Measured by the MASFlux Buoy on April 26–27, 2015.....	27
Figure 10.	Temporal Variation of Wind Speed (a) and Direction (b) Measured by the MASFlux Buoy on April 26–27, 2015.....	28
Figure 11.	Temporal Variation of Pressure Measured by the MASFlux Buoy on April 26–27, 2015.	29
Figure 12.	Temporal Variation of Specific Humidity as Measured by the MASFlux Buoy on April 26–27, 2015.	30
Figure 13.	Temporal Variation of Significant Wave Height (SWH) Measured by the MASFlux Buoy on April 26–27, 2015.....	30
Figure 14.	Temporal Variation in Heat Flux (a) and Frictional Velocity (b) Calculated from the MASFlux Buoy Measurements on April 26–27, 2015.....	32
Figure 15.	Temporal Variation in (a) Wind Speed, (b) θ and SST, (c) Specific Humidity, and (d) Modified Refractivity, as Measured and Calculated from MASFlux April 26–27, 2015.	33

Figure 16.	COARE Profiles during a Period of Stable Thermal Stratification (01:00) with Inputs from Measurement Levels One to Three. (a) Wind Speed, (b) Potential Temperature, (c) Specific Humidity, (d) Modified Refractivity.....	35
Figure 17.	COARE Profiles during a Period of Unstable Thermal Stratification (11:00) with Inputs from Measurement Levels One to Three. (a) Wind Speed, (b) Potential Temperature, (c) Specific Humidity, (d) Modified Refractivity.....	37
Figure 18.	Example Error Plot Calculation.....	40
Figure 19.	COARE Profile Error in Temperature. (a) Level One Input, (b) Level Two Input, (c) Level Three Input.	41
Figure 20.	COARE Profile Error in Specific Humidity. (a) Level One Input, (b) Level Two Input, (c) Level Three Input.	42
Figure 21.	COARE Profile Error in Wind Speed. (a) Level One Input, (b) Level Two input, (c) Level Three Input.....	44
Figure 22.	COARE Profile Error in Modified Refractivity. (a) Level One Input, (b) Level Two input, (c) Level Three Input.....	46
Figure 23.	Comparison of Measured and COARE Parameterized Surface Fluxes. (a) Momentum Flux, (b) Sensible Heat Flux, (c) Latent Heat Flux.	50
Figure 24.	Evaporation Duct Height (a) and Duct Strength (b) Derived from the Modified COARE Algorithm; and Corresponding Wind Speed Variability (c), and Turbulent Kinetic Energy (d).	53
Figure 25.	SHF from the COARE Model with and without Correction of the SST.....	56
Figure 26.	CASPER-East Deployment Map. (a) Legs 7 – 12, (b) Legs 10 – 12	57
Figure 27.	CASPER-East Deployments 7 – 16 Wind Comparison.	58
Figure 28.	CASPER-East Deployments 7 - 16 Temperature Comparison.....	60
Figure 29.	CASPER-East Deployments 7 - 16 Specific Humidity Comparison.....	62
Figure 30.	CASPER-East Deployments 7 – 16 Modified Refractivity Comparison.....	63
Figure 31.	CASPER-East Deployments 7 – 16 Sensible Heat Flux Comparison.....	64

Figure 32.	Frictional Velocity in CASPER-East Deployments 7 – 16.	65
Figure 33.	Potential Temperature for CASPER-East Observations and COARE Model Output for Deployments 7 – 12.	68
Figure 34.	Specific Humidity for CASPER-East Observations and COARE Model Output for Deployments 7 – 12.	69
Figure 35.	Wind Speed for CASPER-East Observations and COARE Model Output for Deployments 7 – 12.	70
Figure 36.	Modified Refractivity for CASPER-East Observations and COARE Model Output for Deployments 7 – 12.	71
Figure 37.	CASPER-East Error for each Variable Plotted Versus Height. (a) θ , (b) Specific Humidity, (c) Wind Speed, (d) Modified Refractivity.....	79
Figure 38.	Measured Sea Surface Temperature from CTV (Long Northwest-Southeast Line) and from R/V Sharp (Short lines) on November 1, 2015.....	82
Figure 39.	CASPER-East Leg 12 MASFlux Buoy, R/V HRS, Tethered Balloon and CTV Observations. (a) Temperature (b) Specific Humidity.....	82

THIS PAGE INTENTIONALLY LEFT BLANK

LIST OF TABLES

Table 1.	MASFlux Buoy Configurations for CASPER-Pilot. Adapted from Zuniga (2013).....	14
Table 2.	MASFlux Buoy Configurations for CASPER-East. Adapted from Zuniga (2013).....	15
Table 3.	CASPER-Pilot Deployment Time/Day and Durations.....	19
Table 4.	CASPER-East Deployment Time/Day and Durations.....	21
Table 5.	Level One (a), Two (b), and Three (c) Mean Error Compared with other Levels for the Stable and Strong Wind Condition, Stable and Weak Wind Condition, and Unstable Condition.	48
Table 6.	Mean wind speed, SST and potential temperature from R/V Sharp and MASFlux during CASPER-East.....	59
Table 7.	CASPER-East COARE Profile Errors with Level One Input.	72
Table 8.	CASPER-East COARE Profile Errors with Level Two Input.....	73
Table 9.	CASPER-East COARE Profile Errors with Level Three Input.....	74
Table 10.	CASPER-East COARE Profile Errors with Level Four Input.....	75
Table 11.	CASPER-East COARE Profile Errors with Ship Level Input.....	76
Table 12.	CASPER-East Mean Error of COARE Profiles for θ (K) for All Input Levels.	76
Table 13.	CASPER-East Mean Error of COARE Profiles for Specific Humidity (g kg^{-1}) for All Input Levels.	77
Table 14.	CASPER-East Mean Error of COARE Profiles for Wind Speed (m s^{-1}) for All Input Levels.	77
Table 15.	CASPER-East Mean Error of COARE Profiles for Modified Refractivity (M Units) for All Input Levels.....	78
Table 16.	CASPER-East Evaporation Duct Height.....	80

THIS PAGE INTENTIONALLY LEFT BLANK

LIST OF ACRONYMS AND ABBREVIATIONS

ABL	Atmospheric Boundary Layer
ASI	Air-Sea interaction
ASL	Above sea level
ASTD	Air-sea temperature difference
CASPER	Coupled Air-Sea Processes and Electromagnetic ducting Research
COARE	Coupled Ocean-Atmosphere Response Experiment
CTV	Controlled Towed Vehicle
EDH	Evaporation duct height
EDS	Evaporation duct strength
EM	Electromagnetic wave
EMS	Electromagnetic wave spectrum
EMW	Electromagnetic Maneuver Warfare
LHF	Latent heat flux
M	Modified refractivity
MF	Momentum flux
MABL	Marine atmospheric boundary layer
MASFlux	Marine Air-Sea Flux buoy
MASL	Marine atmospheric surface layer
MGB	Musson-Genon-Gauthier-Bruth
MOST	Monin-Obukhov Similarity Theory
N	Index of refractivity
NAVSLaM	Navy Atmospheric Vertical Surface Layer Model
NPS	Naval Postgraduate School
ONR	Office of Naval Research
PJ	Paulus-Jeske
RH	Relative humidity
R/V	Research Vessel
SWH	Significant wave height
SST	Sea surface temperature
SSST	Skin sea surface temperature

T

Temperature

TKE

Turbulent kinetic energy

I. INTRODUCTION

A. OVERVIEW

The atmosphere and the ocean are each very complex in their thermodynamics and dynamic structure. They affect each other in many different time scales, often referred to as air-sea interaction (ASI). Understanding these interactions is critical for producing accurate forecasts for the essentially coupled air-sea systems. Additionally, precise and accurate data collection is vital to furthering our understanding of the atmosphere, ocean, their interactions, and how they should be modeled. In the past 25 years, many advances in understanding air-sea interaction processes and their representations in prognostic models have been made including better parameterizations of the air-sea exchange of momentum, sensible and latent heat fluxes as well as the complex wave-air-sea interaction and the wave affected boundary layers (Fairall et al. 1996, 2003, Donelan et al. 1993; Drennan et al. 2003; Sullivan et al. 2008, etc.). However, many fundamental issues still exist that require extensive research using all possible resources including new measurement, modeling, and analyses techniques.

In response to the increasing need of understanding the atmospheric effects that impact optical, radio, radar propagation and cyber, the U.S. Navy has established new strategies in dealing with exploiting and safeguarding the electromagnetic (EM) spectrum and increasingly networked systems as part of Electromagnetic Maneuver Warfare (EMW). The atmospheric effects on EM propagation are largely tied to air-sea interaction processes to include near surface turbulence and its vertical variation. Additionally temperature and specific humidity gradients in the Marine-Atmospheric Surface Layer (MASL) are key in determining EM propagation. Unfortunately, these topics were not the central focus of many of the past research efforts on air-sea interaction. New initiatives in recent years, such as the Coupled Air-Sea Processes and EM ducting Research (CASPER), intend to address these EM propagation related scientific issues. The goal of CASPER is to better understand the surface layer and boundary layer physics, to understand the effects of atmospheric refractivity on EM propagation on different length scales, and to evaluate and improve evaporation duct models and mesoscale models for

EM propagation. This thesis work is part of the CASPER effort with the focus on new capabilities in revealing evaporative duct characteristics. The measurements near the air-sea interface taken during the CASPER project have provided a useful opportunity for in-depth analyses of the air-sea interaction processes to address specific issues in evaporation duct modeling.

One of the most important EM ducting types is the evaporation duct, which is a result of the strong gradients of water vapor content adjacent to the air-sea interface. Quantifying the evaporation duct, mainly its height and strength, is challenging over the ocean because of the lack of data. The Marine Air-Sea Flux (MASFlux) buoys were developed at the Naval Postgraduate School (NPS) to address the data needs near the sea surface. These buoys create only minimal distortion to the atmosphere and ocean, which allows for data to be collected as close to the true air/ocean environment as possible. This thesis will examine data collected from the MASFlux buoys during CASPER field campaigns and demonstrate its application in studying the characteristics of air-sea interactions over different maritime environments and their impacts on atmospheric refractivity and hence EM wave propagation in support of EMW. Since temperature, humidity, and wind speed near the surface are critical aspects of the atmosphere affecting refractivity, this research aims to achieve a better understanding of these environmental variables and their impacts on the propagation of EM waves.

B. SIGNIFICANCE OF THESIS WORK

This thesis investigates measurements from a small buoy and how the collected data can be used to quantify the atmospheric effects on EM propagation over the ocean. Anomalous propagation over the ocean is mostly commonly caused by evaporation ducts (Babin et al. 1997). The use of the MASFlux buoys in CASPER provides important data from an undisturbed air-sea interface which has not been previously collected. Compared to research vessels that induced modifications to the low-level atmospheric properties in the immediate vicinity of the ships, the MASFlux buoys minimize distortions and allow for an accurate depiction of the marine atmospheric surface layer characteristics.

The Monin-Obukhov Similarity Theory (MOST), which is described in detail in Chapter II, Section D, is the basic theory that describes the atmospheric surface layer thermodynamics. The validity of this theory remains questionable over the ocean (Edson et al. 1999) as most of the parameters in MOST were originally developed from measurements over land. In general, MOST-based models have been successful over the ocean in unstable conditions, while significant issues have been identified over the ocean in stable conditions (Fredrickson et al. 2003). With the large amount of coordinated measurements, CASPER provides an excellent opportunity to improve our understanding of fluxes over the ocean, the near surface refractivity profiles, and how they impact EM propagation.

C. OBJECTIVES

MASFlux buoy measurements include concurrent atmospheric and oceanographic conditions on both sides of the interface as they evolved over time, including air temperature, sea surface temperature, and wind speed at multiple levels, and fluxes of momentum and sensible heat near the surface. The main objective of this thesis work is to determine how these measurements can improve our understanding of the MASL and how the measurements close to the surface can be used to characterize evaporation ducts. A better understanding of the MASL will allow for more accurate model prediction of refractivity profiles as well as surface fluxes to be used in operational forecasts of the marine atmosphere phenomena and their impact on radar and communication signals propagating in the lower atmosphere. CASPER is the first major field campaign emphasizing on concurrent atmosphere, ocean, and EM ducting measurements. The analysis of MASFlux data can be aided by many other measurements in CASPER.

D. MILITARY APPLICATION

Rapid technological development in recent years substantially altered the way military forces engage and defeat the enemy through broad involvement of the electromagnetic wave spectrum (EMS), which led to EMW. In this era of EMW, it is more important for the warfighter to understand the battlespace environment with a high level of detail, both spatially and temporally (Edson et al. 1999) due to the significant

impact of the atmosphere on EM propagation that eventually affects command, control, and communications. Rear Admiral Tim Gallaudet, commander, Naval Meteorology and Oceanography Command stated the importance of EMW in 2016. The three major goals in the EMW strategy of the Naval Meteorology and Oceanography Command are to “(1) Influence development of the Navy’s electromagnetic maneuver warfare capabilities, (2) Improve Naval Oceanography’s environmental sensing and prediction capabilities (3) Integrate electromagnetic environmental impacts into the Navy’s decision-making process” (Gallaudet 2016). This thesis will specifically contribute to the second goal of improving environmental sensing and prediction capabilities through a better understanding of EM propagation above the surface of the ocean.

Communication and the use of sensors are critical aspects of naval operations. EM ducting can affect communications between ships and from ship to shore, and affect radar detection that are both land and sea based (Babin et al. 1997). By gaining a better understanding of the atmosphere near the surface of the ocean, the warfighters will be in a better position to tactically exploit the EM spectrum. Small changes in humidity and temperature within the atmospheric boundary layer (ABL) can have significant impacts on naval activity at sea, ranging from communications to EM warfare and detection (Edson et al. 1999). This thesis work will evaluate sensitivities of the evaporation duct properties by choosing observation altitudes for EM ducting condition assessment in addition to gaining basic understanding of MOST for the marine atmospheric surface layer.

II. BACKGROUND

A. ATMOSPHERIC EFFECTS ON EM PROPAGATION

Atmospheric temperature, pressure, and water vapor amount are key components in determining the propagation of electromagnetic waves through the atmosphere (Babin et al. 1997). These parameters are used in determining the refractivity index, N .

$$N = (n - 1) \times 10^6 = \frac{77.6}{T} (p + \frac{4810e}{T})$$

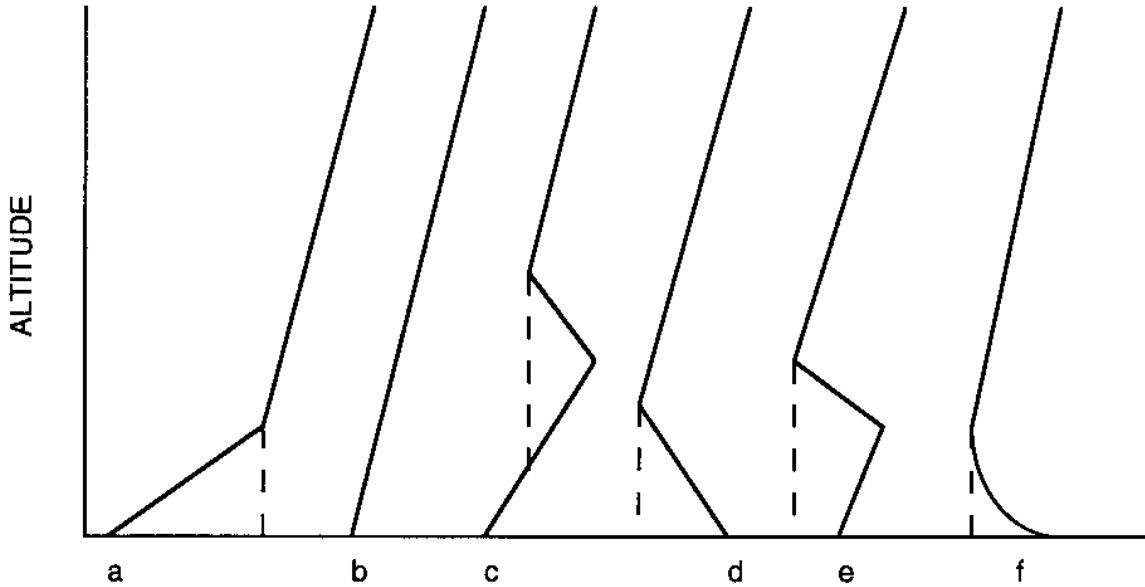
where T is temperature measured in Kelvin, p is atmospheric pressure measured in hecto-pascals, and e is the water vapor pressure also measured in hecto-pascals. The modified refractivity, M , is defined in the following equation to take consideration of the earth's curvature (Edson et al. 1999).

$$M = N + \frac{z}{10^{-6} R_e} \approx N + 0.157z$$

In this case, z is height in meters and R_e is the radius of the earth.

The shape of the M profile, or the vertical gradient of M , determines the type of horizontal propagation path of the EM waves in the atmosphere. Examples of modified refractivity profiles related to different ducting conditions are given in Figure 1 (From Babin et al. 1997)

EXAMPLES OF MODIFIED REFRACTIVITY PROFILES



MODIFIED REFRACTIVITY M

In this image from Babin et al. (1997), “plots of modified refractivity M versus altitude: (a) subrefractive layer denoted by dashed line; (b) normal refraction; (c) elevated duct denoted by dashed line; (d) surface duct denoted by dashed line; (e) surface duct (dashed line) due to elevated region of strongly negative vertical M gradient; (f) evaporation duct denoted by dashed line.”

Figure 1. Illustration of the Vertical Variation of Modified Refractivity, M in Different Ducting Conditions.

The shape of the M profile leads to normal or abnormal refractive conditions. Abnormal refraction refers to both super-refraction and sub-refraction (Babin et al. 1997). The different types of atmospheric propagation, based on M profiles, corresponding to conditions in Figure 1 are given in Figure 2 (Turton et al. 1988), with different thresholds for dM/dz and dN/dz in different propagation regimes. Sub-refraction describes the regime in which EM waves bend upward and away from the surface of the earth. An example of sub-refractive profile is shown in Figure 1a. During standard refraction energy will typically not bend away or towards the surface of the earth. An example of this M profile is seen in Figure 1b. Super-refraction describes the regime in which EM waves bend downward toward the surface of the earth. This can lead to propagation over the horizon (Babin et al. 1997).

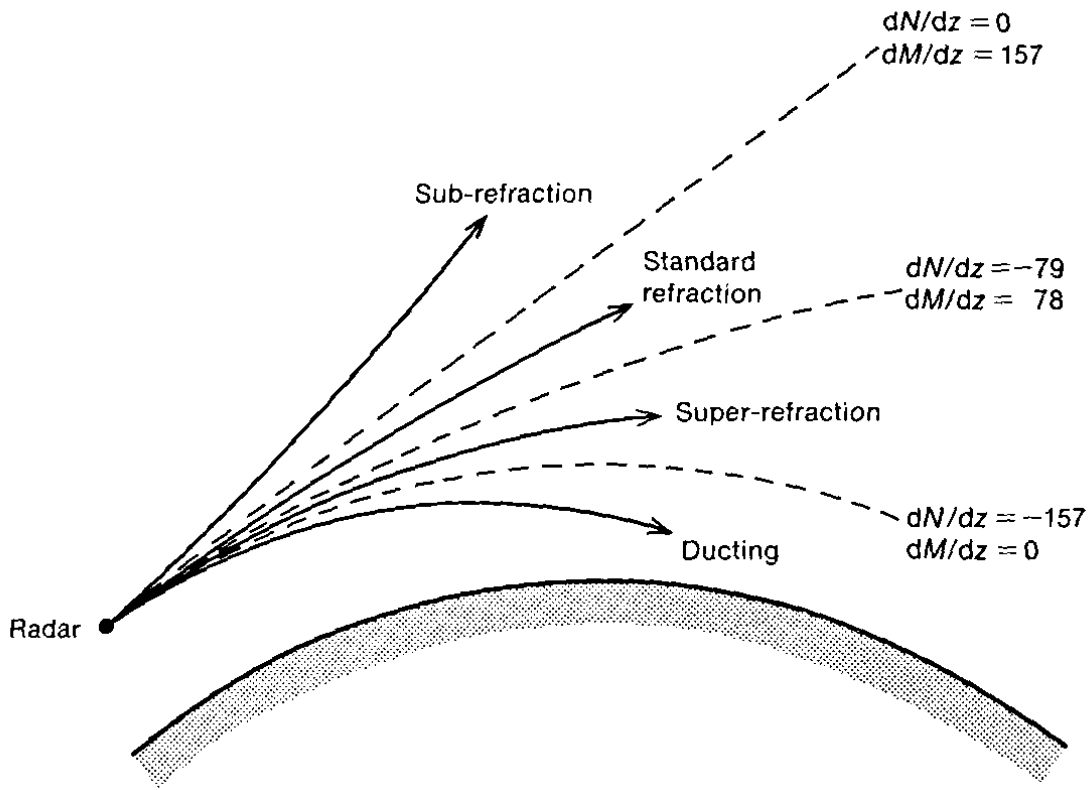


Figure 2. The Four Categories for Atmospheric EM Propagation.
Source: Turton et al. (1988)

The most frequently occurring abnormal refractive condition is ducting, the final type of refraction depicted in Figure 2. Ducting can occur at the surface or it can be elevated. Ducting occurs when there exists a layer of decreasing modified index of refraction, normally referred to as the trapping layer, that results in a duct layer in which energy can be trapped (Bean et al. 1968). The duct is thus a layer of concentrated energy at the expense of decreasing in energy either above or below the duct; this is described as a radar “hole” (Turton et al. 1988). The EM ducting can be caused by various atmospheric processes. They are summarized by Turton et al. (1988). Basically, ducts are typically associated with five types of weather or surface processes to include evaporation over the sea, synoptic scale anticyclonic subsidence, post-frontal and frontal subsidence, longwave radiation induced nocturnal cooling over a land surface, and advection of warm and dry air masses (Turton et al. 1988). These processes result in a

layer of decreasing water vapor with height, which is the primary factor in determining the gradient of the M-profile (Fredrickson 2003). While all type of refraction and ducting are important, this thesis specifically focuses on the evaporation duct, which is located immediately above the sea surface (Turton et al. 1988). The evaporation duct is part of the Marine Atmospheric Surface Layer (MASL). The evaporation duct structures based on input from the MASFlux measurements will be examined in Chapters IV and V.

B. EVAPORATION DUCT

The evaporation duct is of critical importance to Naval operations because it is present nearly all of the time at sea and often overland. An evaporation duct occurs because of the large humidity gradient directly above the sea surface (Wang 2017). The evaporation duct height (EDH) is determined at the altitude where dM/dz , the change in modified refractivity with respect to height, is equal to zero. This EDH can vary greatly in space and time (Babin et al. 1997). However, it generally effects EM propagation within 40 meters of the surface of the ocean (Babin et al. 2001).

Evaporation duct height is perhaps the most important characteristics of an evaporation duct. It was found that significant errors in EM propagation prediction can occur when the error in EDH is greater than two meters (Konstanzer 1994). However, it is extremely difficult to sample the MASL to directly obtain evaporation duct height from M-profiles derived from measurements until CASPER-East. Obtaining EDH mostly relied on evaporation duct models with several bulk meteorological variables in the surface layer as input. These variables include, wind speed, air temperature, relative humidity from a single level, and sea surface temperature (Paulus 1989). Accurately predicting EDH is critical for accurately prediction EM propagation. Several evaporation duct models have been used in the past to generate an evaporation duct M-profile. These models are briefly described in the following.

C. EVAPORATION DUCT MODELS

Models capable of producing modified refractivity (M-profiles) in the MASL or major evaporation duct properties (e.g., EDH or EDS) are referred to as the evaporation duct models. They are needed to determine the surface layer M-profiles as input to the

EM propagation models to assess the effects of such profiles on EM propagation (Babin et al. 2001). There are several different evaporation duct models. The United States Navy started using the Paulus-Jeske (PJ) model in 1978, which has now been replaced by the Navy Atmospheric Vertical Surface Layer Model (NAVSLaM) as the Navy's current operational evaporation duct model (Fredrickson 2010). Additional models include the Musson-Genon-Gautheir-Bruth or MGB model (Musson et al. 1992) and the Babin model (Babin 1997). While all above models employ the surface layer similarity theory, the nondimensional empirical gradient functions surface layer scalars (temperature and water vapor) and wind may take different forms, which resulted in rather different M-profiles of the evaporation duct (Babin 1997). Notably, the Babin model and NAVSLaM both used the empirical relationship from the Coupled Ocean-Atmosphere Response Experiment (COARE) surface flux algorithm (Fairall et al. 1996, 2003) with some slight modifications. Alternatively, the COARE flux algorithm itself can be modified to output profiles of temperature and water vapor specific humidity from which the M-profile can be derived (Cherrett 2015). Hence, the COARE algorithm itself can be used as an evaporation duct model, which is the case in this thesis work. We will refer to this model as the COARE model.

The PJ model introduced a new quantity called potential refractivity that was considered a conserved quantity in the surface layer. This quantity was derived from temperature, water vapor, and mean wind at a single level (6 m) and sea surface temperature while assuming that the surface layer pressure is a constant of 1000 hPa (Paulus 1985). It was later found that potential refractivity was not a conserved quantity (Cook and Burk 1992). In addition, the PJ model assumes a constant aerodynamic roughness length, which is certainly not true anywhere over the ocean or land surfaces (e.g., Fairall 1996).

D. MONIN-OBUKHOV SIMILARITY THEORY (MOST)

The Monin-Obukhov similarity theory assumes that the structure of the atmospheric surface layer is controlled by two basic forcing mechanisms: mechanical and thermal forcing of turbulence. Under this assumption and utilizing the Pi theory, the

surface layer nondimensional gradients for wind speed, temperature, and humidity can be expressed in terms of height (z) scaled by the Monin-Obukhov length (L) to form a nondimensional height. Monin-Obukhov length, L , is defined as

$$L = -\frac{u_*^3}{\kappa \frac{g}{T_o} \frac{Q}{c_p \rho}}$$

where u_* is the dynamic velocity, κ is the von Karman constant (between 0.35 and 0.4), g is gravity, T_o is temperature, Q is the vertical turbulent heat flux, c_p is the specific heat of air under constant pressure, and ρ is density (Monin 1954). The original empirical dimensionless functions in MOST were obtained from data collected in the Kansas experiment and described by Businger et al. (1971).

The dimensionless wind shear, $\phi_m(\frac{z}{L})$ and dimensionless temperature gradient $\phi_h(\frac{z}{L})$ are piece-wise functions for unstable ($\frac{z}{L} < 0$), stable ($\frac{z}{L} > 0$) and neutral ($\frac{z}{L} = 0$) thermal stratifications given below (Businger et al. 1971). However, many field campaigns were made after the 1968 Kansas experiment in an attempt to gain greater accuracy. Grachev et al. (2000), for example, modified the formulation to match the observed profiles in free convection, while Beljaars and Holtslag (1991) modified the stable formulation based on measurements from the Arctic. The work by Fairall et al. (1996 and 2003) combined the state-of-art representation of the empirical functions, the surface roughness, and skin temperature correction and many other factors affecting the MSL into the COARE surface flux algorithm.

$$\phi_m(\frac{z}{L}) = \begin{cases} (1 - 15 \frac{z}{L})^{-1/4} & \frac{z}{L} < 0 \quad \text{unstable} \\ 1 & \frac{z}{L} = 0 \quad \text{neutral} \\ (1 + 4.7 \frac{z}{L}) & \frac{z}{L} > 0 \quad \text{stable} \end{cases}$$

$$\phi_h\left(\frac{z}{L}\right) = \begin{cases} 0.74(1 - 9\frac{z}{L})^{-1/2} & \frac{z}{L} < 0 \text{ unstable} \\ 0.74 & \frac{z}{L} = 0 \text{ neutral} \\ (0.74 + 4.7\frac{z}{L}) & \frac{z}{L} > 0 \text{ stable} \end{cases}$$

Additionally, MOST is limited in its application to surfaces, such as ocean waves, that have their own dynamic structures (Hill 1989). Foken (2006) described MOST as limited to the surface layer and that it was most likely not valid above tall vegetation. “Furthermore, even under ideal conditions, the theory has an accuracy of only about 10–20%” (Foken 2006).

E. CASPER OVERVIEW

CASPER is an Office of Naval Research (ONR) Multidisciplinary University Research Initiative (MURI) Project that began in 2014 and will continue through 2019. There are four primary objectives of CASPER as described by Wang (2017). These include (1) to gather a dataset that is both comprehensive and cohesive to aid in the modeling and analyses of critical air-sea interaction processes related to EM propagation, (2) to improve MASL models with regards to temperature and water vapor profiles and how these profiles are affected by waves and swells, (3) to obtain a better understanding of the MABL and its impact on EM propagation, (4) to explore new and different approaches in EM propagation modeling in varying atmospheric conditions.

CASPER involves three field campaigns, the CASPER-Pilot experiment was conducted in Monterey Bay from April 20, 2015, to May 5, 2015. CASPER-East was conducted off the coast of Duck, NC from October 9, 2015, to November 6, 2015. CASPER-West will be conducted offshore of Point Mugu, CA, in September and October of 2017. The CASPER-East location provides a variety of conditions due to strong sea surface temperature (SST) variability associated with the continental shelf and the Gulf Stream (GS). This allowed for measurements over cool SST regions at ~20°C,

warm SST regions at 26 °C, and the gradient in between. Additionally, the proximity to the coast allowed for study of the impact of coastal thermal circulation. In this thesis work, data collected during CASPER-Pilot and CASPER-East will be analyzed. In particular, the measurements from the MASFlux buoy will be studied.

III. DATA COLLECTION

A. MASFLUX BUOY

The MASFlux buoy was developed by the Department of Meteorology at NPS in Monterey, CA. The buoys were designed to be small, portable, and easily deployable. The buoys are 6.15 meters in height with a 0.5 meter diameter float and weigh about 35 kg. The buoys are equipped with a 3-D sonic anemometer for turbulence and low-rate sampling sensors for four levels of temperatures and relative humidity, two levels of wind, one level of pressure, and three levels of water temperature measurements. In addition, a motion package, including a compass and accelerometer and a GPS receiver, was installed on the mast to measure location, heading, and 3-D angular accelerations. Table 1 describes the configuration of the MASFlux buoy sensors and sensor altitude used in CASPER-Pilot. Table 2 describes the configuration of the buoy for CASPER-East, which was slightly different from CASPER-Pilot. Figure 3 shows a schematic of the MASFlux buoy indicating the location of sensors on the mast. A picture of the MASFlux buoy deployed during CASPER-East is given in Figure 4. A critical aspect of this configuration is multi-level measurements of the wind and thermodynamic quantities. The heights of the temperature and humidity sensors and the depth of the seawater temperature sensors played an important role as discussed in Chapters IV and V. In summary, for both CASPER-Pilot and East field campaign, there were four levels of temperature/humidity measurements within the lowest three meters from the sea surface. Mean wind measurements were made at two levels, while the high rate sampling of wind/turbulence were also made by the 3-D sonic anemometer at the top of the mast. This makes three levels of mean wind measurements from the buoy.

Table 1. MASFlux Buoy Configurations for CASPER-Pilot.
Adapted from Zuniga (2013).

Sensor	Height (m)	Measured variables
Rotronic temperature/humidity Probe, Model MP100H	3.07, 1.54, 0.77 and 0.38	Temperature, relative humidity
Vaisala Weather Transmitter WXT520	1.83	Wind speed and direction, temperature and humidity (not used), barometric pressure
Vaisala WMT52 ultrasonic wind sensor	0.87	Wind speed and direction
Campbell Scientific temperature probe Model 109SS	-0.03, -0.16 and -0.41	Sea water temperature
Garmin GPS16-HVS	2.9	Position, velocity, magnetic declination
RM Young ultrasonic anemometer Model 81000VRE	3.48	High frequency wind speed and wind direction, sonic temperature
True North Revolution Technologies GS gyro stabilized electronic compass	2.9	Heading, pitch, roll
VectorNav VN-100 rugged accelerometer	0.6	Angular rates, linear accelerations, magnetic field components

During CASPER-Pilot, the lowest level of temperature/humidity sensor were frequently wet because of their close proximity to the surface and the presence of waves/swell. Its measurements were hence not reliable and will be omitted in the analyses. As a result, for CASPER-Pilot level one data indicates temperature and humidity observed at 0.77 m and wind measurements observed at 0.87 m, level two data indicates temperature and humidity observed at 1.54 m and wind measurements observed at 1.83 m, level three data indicates temperature and humidity data observed at 3.07 m and wind measurements observed at 3.48 m.

Table 2. MASFlux Buoy Configurations for CASPER-East.
Adapted from Zuniga (2013).

Sensor	Height (m)	Measured variables
Rotronic temperature/humidity Probe, Model MP100H	2.95, 1.6, 0.86 and 0.46	Temperature, relative humidity
Vaisala Weather Transmitter WXT520	1.90	Wind speed and direction, barometric pressure
Vaisala WMT52 ultrasonic wind sensor	0.97	Wind speed and direction
Campbell Scientific temperature probe Model 109SS	-0.25	Sea water temperature
RBR Solo self-recording thermistor	-1.14 and -2.24	Sea water temperature
Garmin GPS16-HVS	2.9	Position, velocity, magnetic declination
RM Young ultrasonic anemometer Model 81000VRE	3.43	High frequency wind speed and wind direction, sonic temperature
True North Revolution Technologies GS gyro stabilized electronic compass	2.9	Heading, pitch, roll
VectorNav VN-100 rugged accelerometer	3.05	Angular rates, linear accelerations, magnetic field components

For CASPER-East level one data indicates temperature and humidity observed at 0.46 m and wind measurements observed at 0.97 m, level two data indicates temperature and humidity observed at 0.86 m and wind measurements observed at 0.97 m, level three data indicates temperature and humidity data observed at 1.6 m and wind measurements observed at 1.90 m, level four indicates temperature and humidity observed at 2.95 m and wind measurements observed at 3.43 m. These levels are the “pairs” of data there were input to the COARE evaporation duct model.

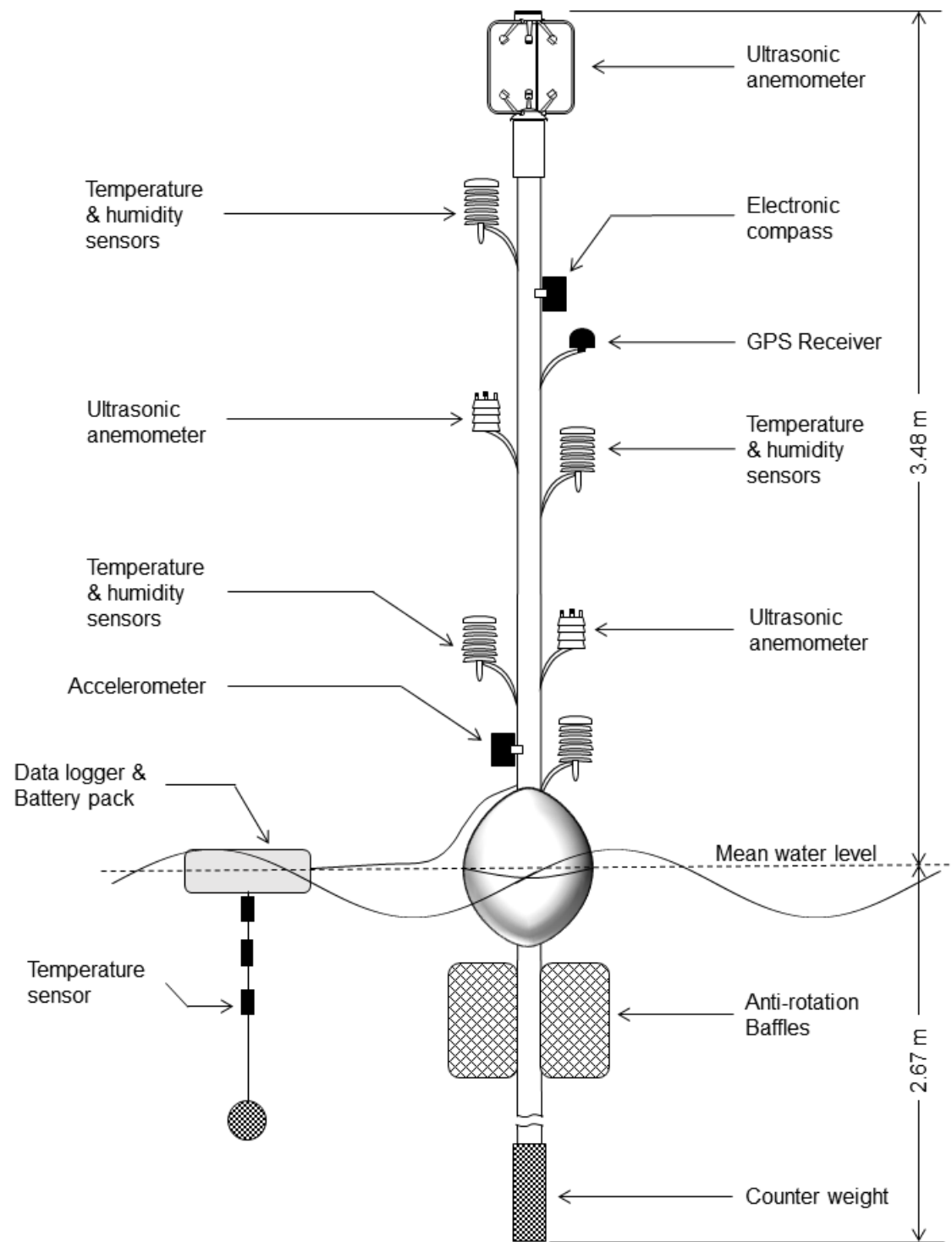


Figure 3. Schematic of the NPS MASFlux Buoy. Source: Alappattu (2017).



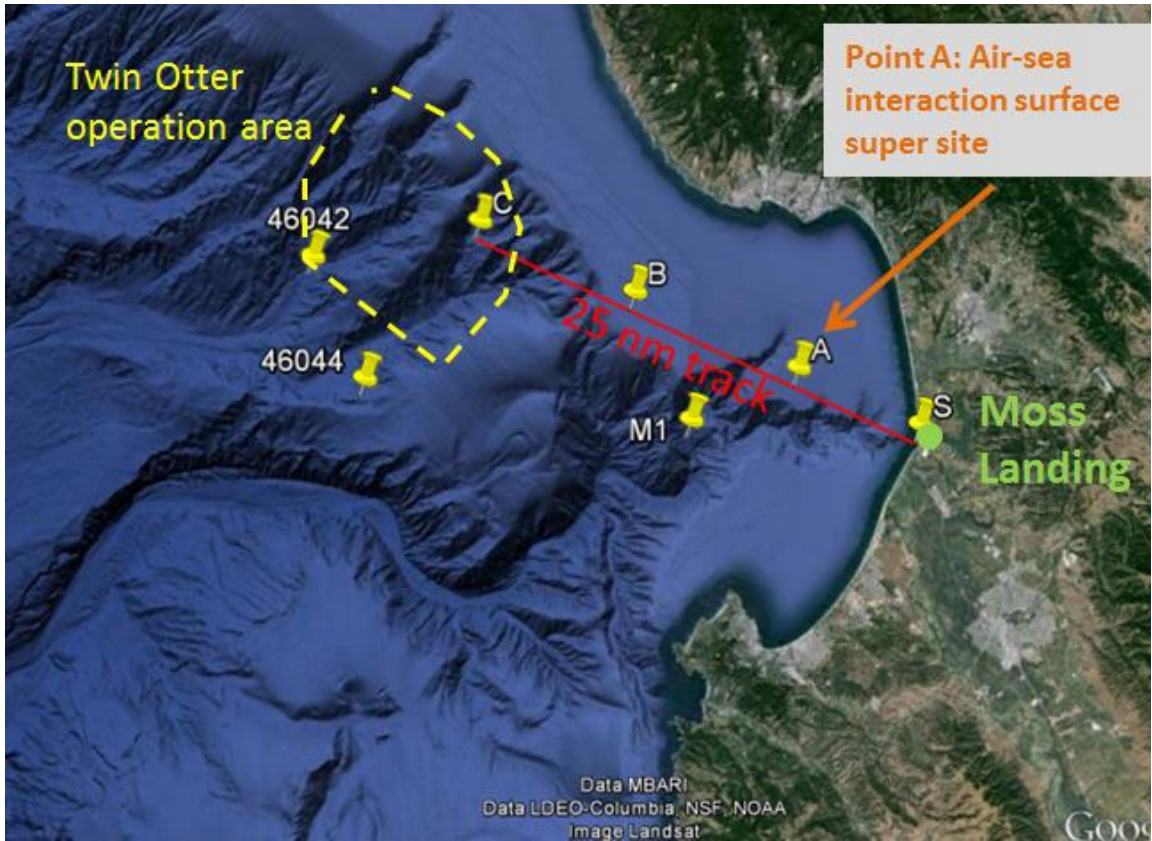
Figure 4. An Example of the NPS MASFlux Buoy when Deployed During CASPER-East. Source: Alappattu (2017).

B. CASPER MASFLUX DEPLOYMENTS

Since its initial development, the NPS MASFlux buoys have gone through several developmental changes and deployed several times before CASPER (Cheney 2010, Zuniga 2013). Some minor adjustments were also made between CASPER-Pilot and CASPER-East field campaign. This section outlines the setup and deployments of MASFlux in both field campaigns, which resulted in the data analyzed in this thesis. Note that MASFlux can be deployed in two different modes, either free drifting or fixed location. When a fixed location is desired, the MASFlux buoy is tethered to a moored surface float or a vessel, which was the mode used in CASPER-Pilot and CASPER-East.

1. CASPER-Pilot

CASPER-Pilot field campaign occurred 20 April – 5 May 2015, during which MASFlux measurements were made on April 21, 26, and 1 – 3 May 2015. Figure 5 shows the measurement area in Monterey Bay off the coast of Moss Landing, CA. Point A ($36^{\circ} 49.706N$, $121^{\circ}55.644W$) on this figure is the location of two moored floats deployed on April 21, 2015. The MASFlux buoy was attached to one of the floats and a tethered balloon with multiple levels of mean temperature and humidity measurements was attached to the other. This location was referred to as the surface super site. Table 3 describes all of the CASPER-Pilot deployment times and durations. It is seen that the duration from each deployment varied significantly, some were a result of weather and others were related to coordination of the ship pick up during relatively high wind events. Data collected on April 26 and April 27, 2015, was especially interesting because of the change from stable conditions to unstable conditions. The MASFlux buoy and the tethered balloon were deployed at around noon on April 26, 2015. Due to the increased wind in the afternoon, the attempt to recover the buoy and the tethered balloon failed and both systems were left in the water through the night. Fortunately, MASFlux survived the strong wind at night and continued to collect data until the next day when R/V John Martin returned to the station. This allowed for a ~30-hour period with a wide range of variations. The tethered balloon data was unfortunately lost as the wind sheared off the sonde packages off the tether line.



Point A ($36^{\circ} 49.706N$, $121^{\circ}55.644W$) is referred to as the surface super site where two surface floats, separated by about 100 m, for tethering the MASFlux and the tethered balloon system were deployed. The water depth at this location is 47 fathom. The red line denotes the R/V John Martin track and the yellow dash line enclosed the intended area for aircraft measurements.

Figure 5. CASPER-Pilot Measurement Area.

Table 3. CASPER-Pilot Deployment Time/Day and Durations.

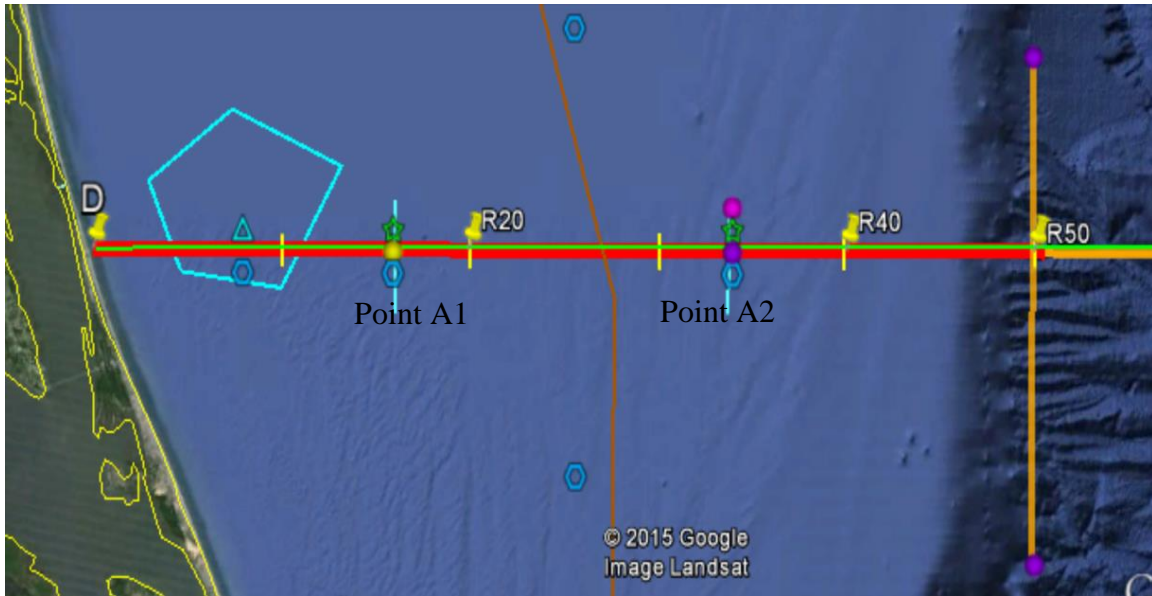
Deployment #	Start Date	End Date	Start Time	End Time	Duration (Hours)
1	21-APR-15	22-APR-15	21:52	01:35	3.72
2	26-APR-15	27-APR-15	18:47	22:32	27.76
3	1-MAY-15	2-MAY-15	16:45	23:51	7.10
4	2-MAY-15	2-MAY-15	17:50	21:55	4.09
5	3-MAY-15	5-MAY-15	16:57	12:46	43.81

A weak frontal system passed through the CASPER-Pilot site location on April 25, 2015. This produced light rain early on April 25, 2015. On April 26, 2015, the area

experienced strong surface wind in the afternoon and continued through the midnight when the weak northeasterly wind kicked in. The high wind period was also accompanied by warm air temperature, resulting in stable thermal stratification in the MASL while the northeasterly wind regime experienced unstable stratification. The measurements on this day thus provided both stable and unstable MASL conditions, which resulted in significant temporal variability within the 30-hour time period.

2. CASPER-East

One of the major CASPER field campaigns, CASPER-East occurred off the coast of Duck, NC in October and November of 2015. The main focus of CASPER-East was to assess the uncertainties in evaporation duct modeling and the effects of a heterogeneous marine environment on EM propagation (Wang et al. 2017). Wang et al. (2017) outlined many specifics of the CASPER-East field campaign. Figure 6 shows the general measurement area with the green stars (Points A1 and A2) denoting the locations of the surface floats used to tether MASFlux buoy. Point A1 was at ($36^{\circ}11'1.27''N$, $75^{\circ}24'57.00''W$) with 29 m water depth, about 16 nm east of the Duck pier; Point A2 was at ($36^{\circ}11'1.27''N$, $75^{\circ} 2'42.70''W$) with 38 m of water depth. Most of the MASFlux deployments were at Point A1 with the exception of Gulf Stream deployments on 30 October – 1 November 2015 and deployments on 3 November 2015, over the continental shelf break region when the MASFlux was tethered to R/V Hugh R. Sharp, one of the two CASPER research vessels. The measurements tethered to the vessels are normally during the ASI sampling module and lasted about 45 – 60 minutes. Table 4 describes all of the CASPER-East MASFlux deployment time, durations and locations. Figure 7 shows the locations of all MASFlux deployments during CASPER-East.



The two green stars denote the locations of the surface super sites (Point A1 and Point A2) at 16 nm and 34 nm east of the Duck pier, respectively.

Figure 6. CASPER-East Measurement Area.

Table 4. CASPER-East Deployment Time/Day and Durations.

Deploy -ment #	Start Date	End Date	Start Time	End Time	Duration (Hours)	Lat.	Long.
1	13-Oct-15	14-Oct-15	11:56	00:22	12.43	36.1675	-75.4334
2	14-Oct-15	16-Oct-15	19:45	11:10	15.40	36.1673	-75.4335
3	20-Oct-15	20-Oct-15	11:14	18:24	7.17	36.1671	-75.4332
4	24-Oct-15	24-Oct-15	11:37	20:49	9.20	36.1729	-75.0708
5	25-Oct-15	25-Oct-15	14:35	22:27	7.87	36.1671	-75.4332
6	29-Oct-15	29-Oct-15	12:51	20:28	7.63	36.1673	-75.4332
7	30-Oct-15	30-Oct-15	13:35	14:41	1.10	36.0105	-74.3161
8	31-Oct-15	31-Oct-15	13:29	14:23	0.90	35.9672	-74.2611
9	31-Oct-15	31-Oct-15	15:40	16:39	0.93	35.9914	-74.3041
10	1-Nov-15	1-Nov-15	12:26	13:15	0.82	35.9421	-74.2212
11	1-Nov-15	1-Nov-15	14:31	15:41	1.17	36.0124	-74.2909
12	1-Nov-15	1-Nov-15	17:13	18:02	0.80	36.0498	-74.3908
13	3-Nov-15	3-Nov-15	14:37	15:49	1.18	36.1815	-75.3496
14	3-Nov-15	3-Nov-15	16:38	17:46	1.12	36.1775	-75.4292
15	3-Nov-15	3-Nov-15	18:30	19:41	1.17	36.1747	-75.5801
16	3-Nov-15	3-Nov-15	20:11	21:27	1.28	36.1721	-75.6667

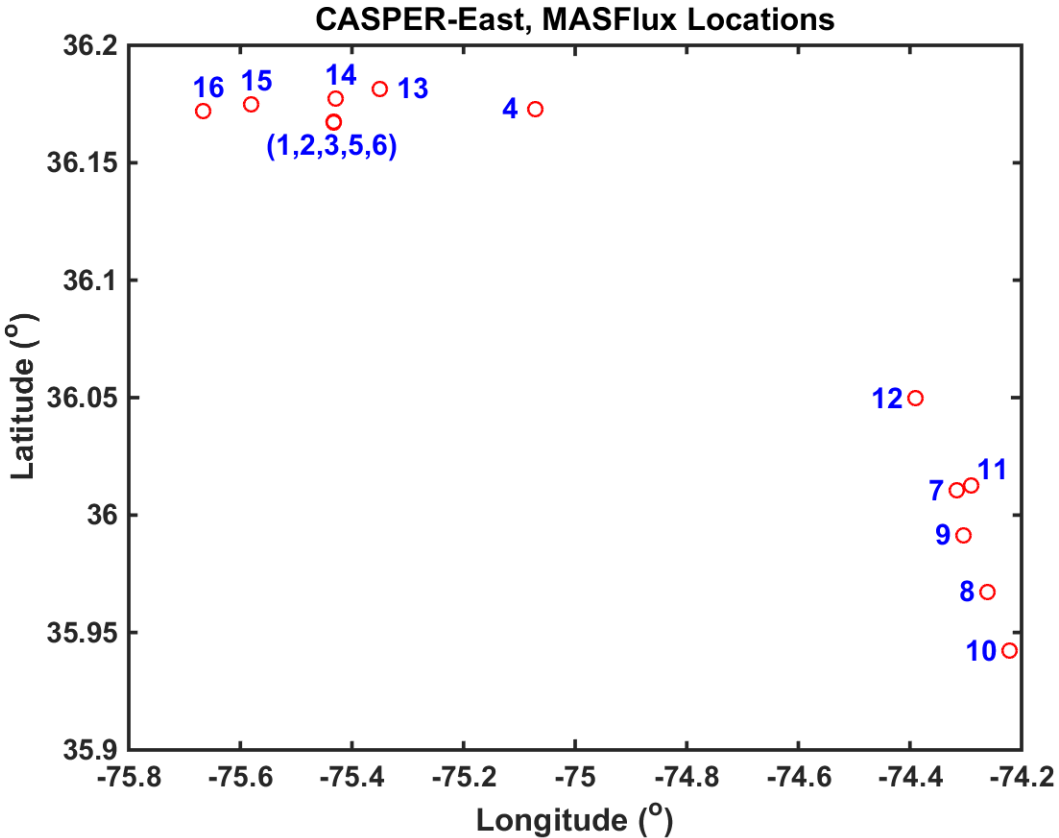


Figure 7. Locations of MASFlux deployments during CASTER-East.

In addition to the MASFlux buoys, there were several other platforms with different instrument setups used in CASPER-East that collected valuable atmospheric and oceanographic data. The R/V Hugh R. Sharp had temperature, wind, and humidity sensors mounted on the bow mast at the height of 12 m. The work boat from the R/V Sharp was also used to deploy a tethered balloon with an iMet sounding package modified to radio data to the tablet computer in real-time. In addition to temperature, humidity and pressure sampling capabilities, the iMet sensor package also included GPS locations and altitude. The package was raised and lowered repeatedly to measure the thermodynamics of the MASL. Finally, there was a Twin Otter Aircraft that measured the SST via an infrared radiometer. The Twin Otter deployed a fully instrumented Controlled Towed Vehicle (CTV) that measured all quantities on the Twin Otter except for the aerosol and cloud measurements. The CTV sampled the atmosphere between 0

and 250 meters above the surface of the ocean. This data was blended together in Chapter IV to help better analyze the evaporation duct and modified refractivity profiles and show the value of the MASFlux buoy.

Several cold fronts passed through the CASPER-East site during the data collection period. These fronts generally brought sustained northerly winds of 10 – 14 m/s, colder air temperatures, and generated rough seas with significant wave heights of approximately two meters. These conditions limited the deployment of MASFlux and other small platforms. However, measurements were made whenever conditions allowed. Table 4 describes the data collection days and times. There were several instances in which the weather conditions did not allow for data collection. A synoptic summary of CASPER-East measurement days is available in the CASPER data archive.

C. SENSOR ACCURACY AND DATA QUALITY CONTROL

1. Sensor Accuracy

The temperature and relative humidity was measured by the Rotronic model MP100H that uses the HygoClipS3 probe. The temperature is accurate to $\pm 0.03^{\circ}\text{C}$ and relative humidity is accurate to $\pm 1.5\%$. All temperature and humidity sensors were calibrated before and after the field experiments. Wind speed and direction along with barometric pressure was measured by the Vaisala Weather Transmitter WXT520 at a height of 1.83 and 1.90 m for CASPER-Pilot and CASPER-East, respectively. The wind speed resolution is 0.1 m/s with an accuracy of ± 3 m/s at 10m/s and ± 3 degrees for direction. The barometric pressure has a resolution of 0.1hPa with accuracy of ± 0.5 hPa. A WMT52 wind sensor with the same accuracy of the WXT520 was used on the MASFlux buoy at a height of 0.87 m.

2. Data Quality Control

MASFlux data went through two steps of data calibration and quality control. First, the sensors from all levels were calibrated before and after the project either in a water bath (CASPER-Pilot) or in a calibration chamber (CASPER-East). The differences among the sensors were removed so that the observed differences among different

altitudes represented vertical variations. Note this calibration does not provide an accurate absolute temperature/humidity, it only removed the relative differences. Secondly, data quality controls were made during the analyses stage through visual inspection “bad” data that was removed from the final datasets were rather apparent compared to other levels. These “bad” data normally occur to the lowest level of temperature/humidity measurements where sensor wetting was likely to occur due to the low altitude of the sensor. Water temperature at the top level may be problematic at times when it was dragged out of water. These periods of measurements were removed from the data analyses. In particular, on 26 April 2015, during CASPER-Pilot experiment, the Rotronic’s temperature/humidity sensor at the 0.38 m level was accidentally submerged in water during shipboard deployment. As a result, both temperature and relative humidity were excluded from analyses. Similar situation may occur on other days where the temperature/humidity data from the lowest level were not included in the analyses.

IV. DATA ANALYSIS

A. CASPER-PILOT

As described in Chapter III, CASPER-Pilot was conducted in late April and early May of 2015 with five deployments totaling about 90 hours. Measurements on April 26 – 27, 2015 were made during a period when the marine atmospheric boundary layer went through both stable and unstable conditions which was very useful data for examining variability of temperature, moisture, and wind gradients under various thermal forcing. This case will be used as an example to illustrate the MASFlux capability for characterizing air-sea interaction processes and for EM ducting.

1. Observed Near-Surface Variability

Strong temporal variation was observed at the buoy location for the deployment of MASFlux on April 26, 2015. The air temperature at all three levels are plotted along with all three levels of sea water temperatures in Figure 8. Figure 8a shows the raw 1 Hz data along with the two minute time averaged data.

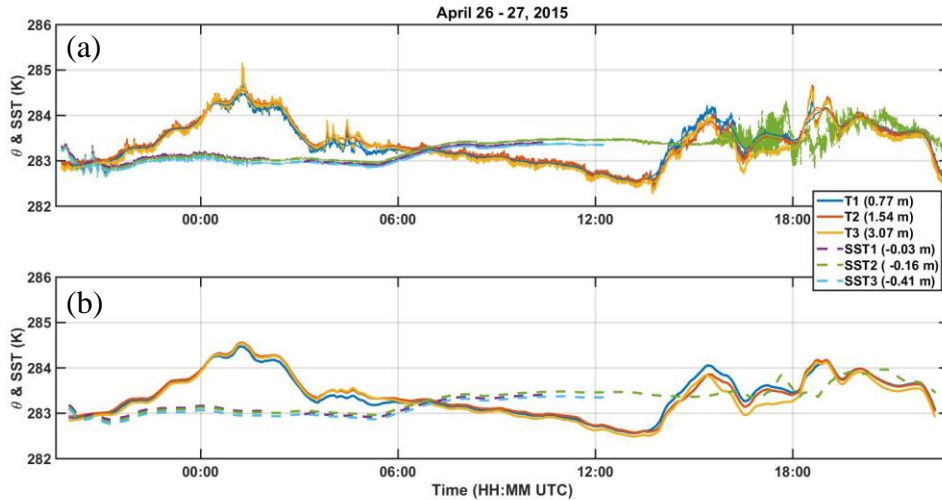


Figure 8. Temporal Variations of Air Temperature and Sea Temperature Measured by the MASFlux Buoy on April 26–27, 2015. (a) Original Data, (b) 2-Minute Low-Pass Filtered Data.

Figure 8b shows the two minute averaged data only to indicate the variation of the mean quantity during the measurement period. Two minute averaged data will be shown for the remainder of the CASPER-Pilot data for clarity of presentation. The air temperature varied between 282.5 and 284.5 K during the ~30 hour period, while the variation of water temperature was less than 1 K. Figure 9 shows the air-sea temperature difference (the sea surface temperature minus the air temperature, or ASTD) throughout the day. Positive values of ASTD indicate unstable thermal stratifications while negative values indicate stable conditions. However, it is important to note that the sea surface temperature was measured at a water depth of 0.4 m, which is different from the skin sea surface temperature (SSST). The potential error in using top water temperature to represent SSST will be estimated later. For simplicity, we still refer to the top level water temperature measurements as SST. Figure 9 shows that the first 11 hours of measurements were persistently made in stable stratification conditions. Unstable surface layers started at about 06:30 UTC and lasted until about 14:00 UTC on 27 April, after which the atmosphere varied near neutral stability with slightly longer cumulative periods of unstable condition. Red shading indicates the stable condition with strong winds, blue shading indicates the unstable condition and green shading indicates the stable condition with weak winds.

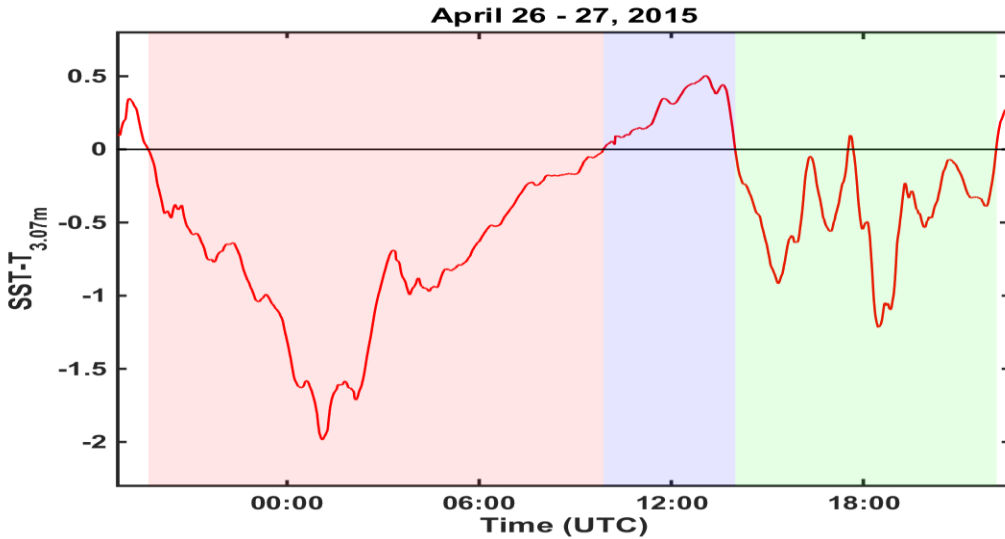


Figure 9. Temporal Variations of Air Temperature and Sea Temperature Difference Measured by the MASFlux Buoy on April 26–27, 2015.

Figure 10 describes the wind variability throughout the day on April 26–27, 2015 as recorded by the MASFlux buoy. The strongest wind occurred at 00:00 while the lowest wind speeds occurred between 10:00 and 18:00. At 00:00 the wind shear is also the strongest as indicated by the largest differences between each of the three levels. Note the green line shows the measurements from the lowest anemometer at 0.87 m, the red line corresponds to measurements at 1.83 m, and the blue line shows the wind speed at 3.48 m.

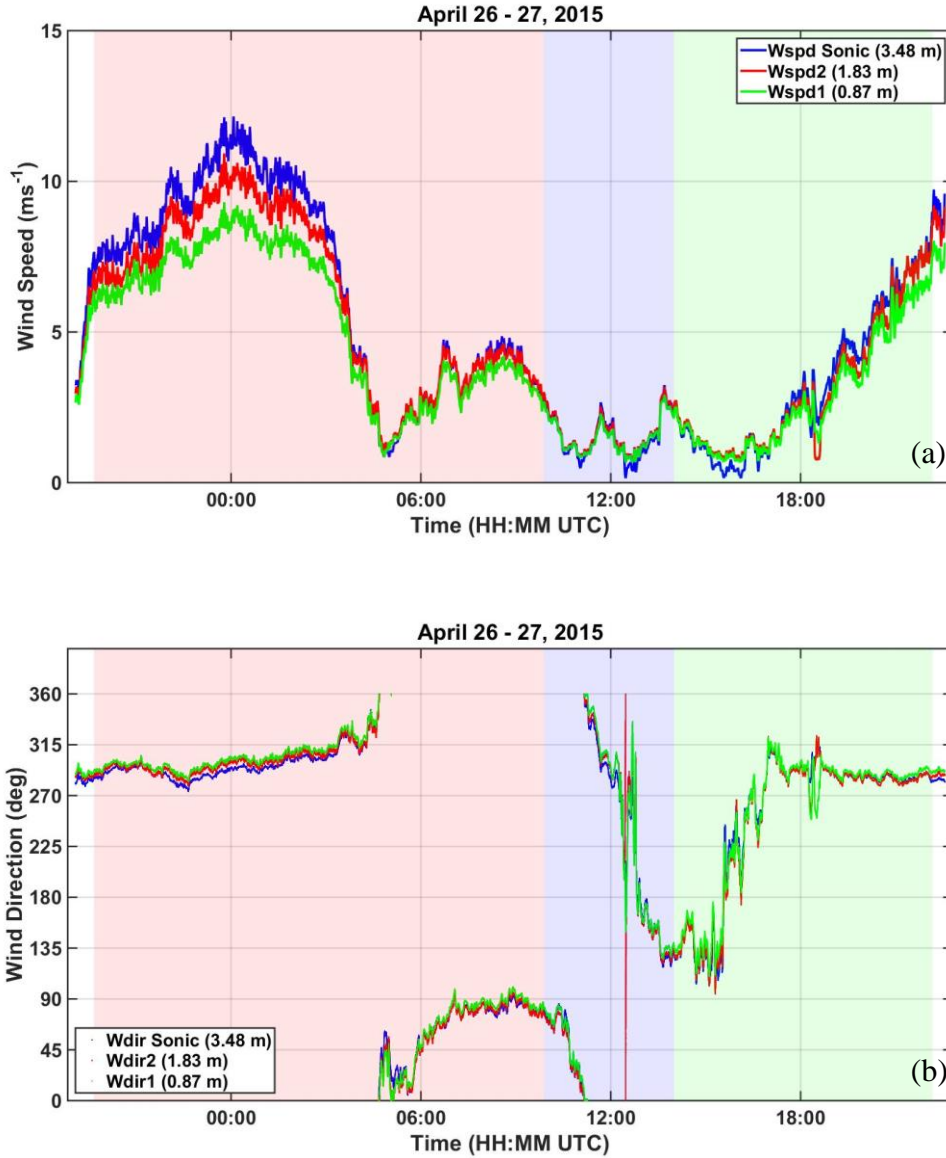


Figure 10. Temporal Variation of Wind Speed (a) and Direction (b) Measured by the MASFlux Buoy on April 26–27, 2015.

Figure 10b describes the direction throughout the day on April 26–27, 2015. The first half of the measurement period shows winds generally out of the west. The winds eventually become easterly at about 09:00 and gradually backing to westerly at 12:00 followed with a dramatic shift to southerly at about 13:00. Winds are from the southeast at 15:00 and then shift back to westerly winds by 18:00. Figure 11 describes the pressure

throughout the time period. Of note, the decreasing pressure around 00:00 corresponds to the increase winds observed in Figure 10.

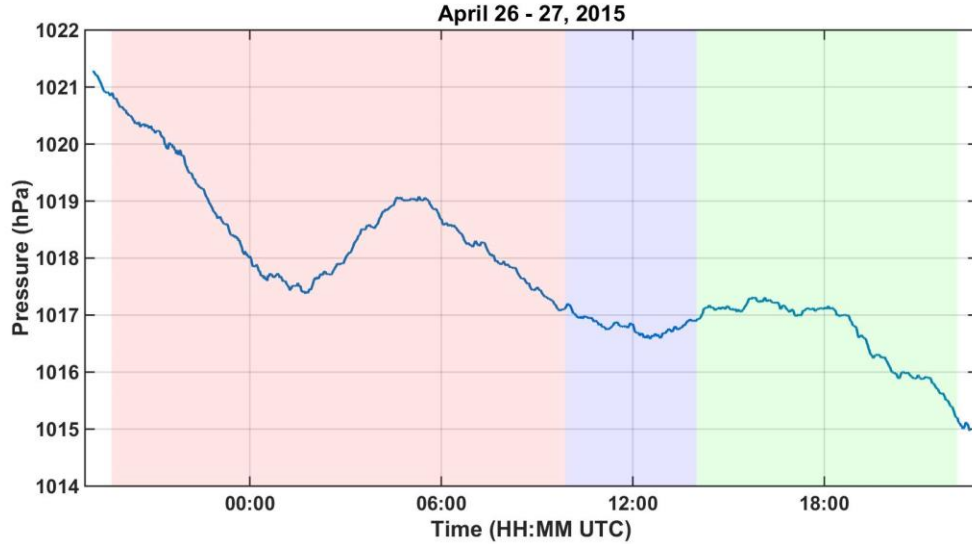


Figure 11. Temporal Variation of Pressure Measured by the MASFlux Buoy on April 26–27, 2015.

Figure 12 shows the specific humidity measured by the MASFlux buoy on April 26–27, 2015. Specific humidity increases until 07:00 then decreases until 15:00 before increasing once again. This figure also shows how the MASFlux buoy is able to resolve the near surface gradient in specific humidity, which allow for more accurate depiction of the modified refractivity profiles for quantifying evaporation duct properties.

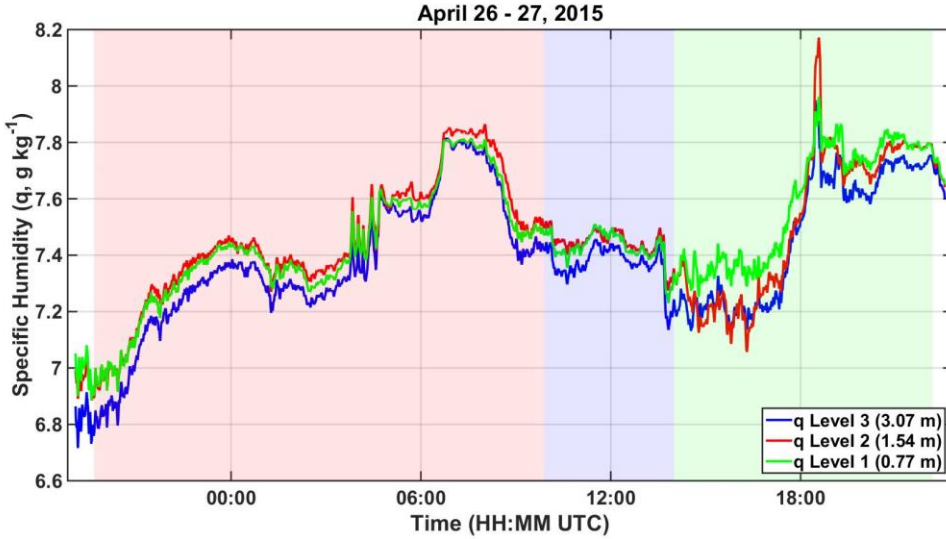


Figure 12. Temporal Variation of Specific Humidity as Measured by the MASFlux Buoy on April 26–27, 2015.

Figure 13 shows the change in significant wave height (SWH) measured by the MASFlux. The wave information was derived from the combination of motion and location sensing on the MASFlux (Zuniga 2013). SWH is at a maximum at 02:00. This corresponds to the time shortly after the maximum westerly wind speed occurred.



Figure 13. Temporal Variation of Significant Wave Height (SWH) Measured by the MASFlux Buoy on April 26–27, 2015.

High-rate sampling of turbulence and temperature perturbations were made on the MASFlux buoy by a 3-D sonic anemometer for direct estimates of turbulent momentum and sensible heat fluxes (Figure 14). The largest negative heat flux occurs shortly after 00:00. This corresponds to the period of the strongest wind and when air temperatures are warmer than SSTs (stable thermal stratification) as seen in Figures 9 and 10. Maximum SWHs also occur at this time in response to the strong wind. The heat flux was very small during the next six hours or so from 06:00 until 12:00. This period corresponds to the identified unstable condition, as seen in Figure 9. The small magnitude of SHF is mainly associated with the low wind speed (Figure 10a). Figure 14b shows the frictional velocity (u^*) derived from the MASFlux measurements. This quantity represents the magnitude of momentum flux. Similar to the SHF, momentum flux reached its maximum at 00:00 corresponding to the maximum wind speed (Figure 10a).

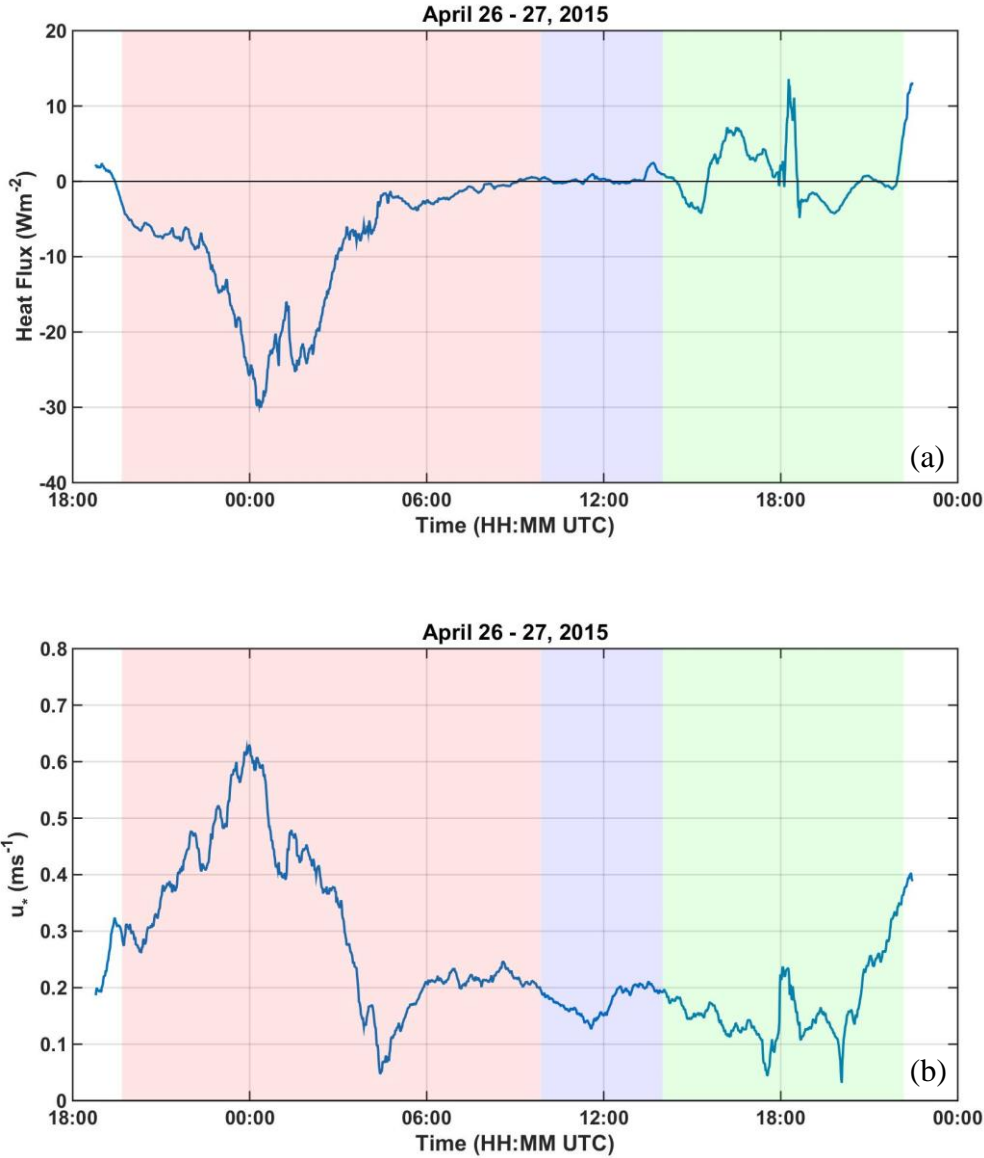


Figure 14. Temporal Variation in Heat Flux (a) and Frictional Velocity (b) Calculated from the MASFlux Buoy Measurements on April 26–27, 2015.

The major advantage of MASFlux is its capability to reveal the near-surface variability by using multiple sensors on a platform with small footprint. Figure 15 shows such vertical variation and how such variation evolved in time using vertical profiles in temperature, specific humidity, wind speed, and modified refractivity at six specific times during the measurement period on April 26–27, 2015. The selected profiles are at a time interval of six hours.

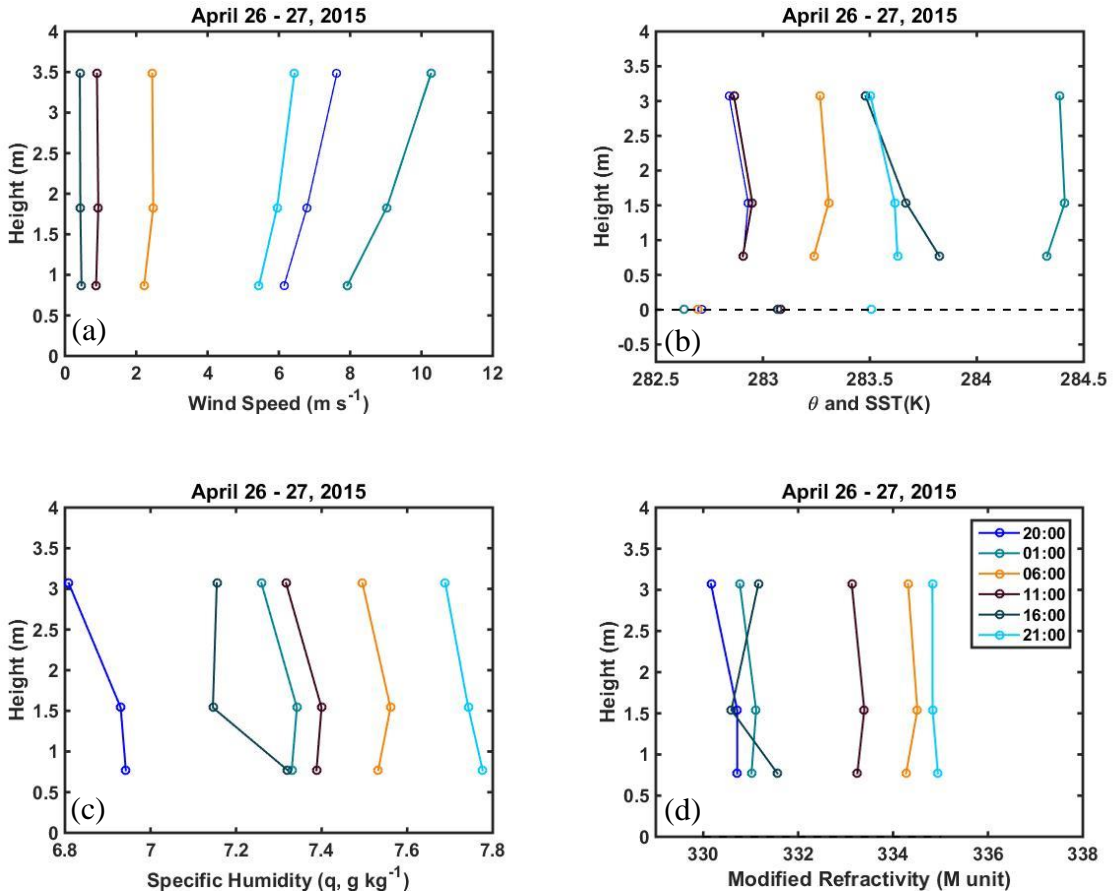


Figure 15. Temporal Variation in (a) Wind Speed, (b) θ and SST, (c) Specific Humidity, and (d) Modified Refractivity, as Measured and Calculated from MASFlux April 26–27, 2015.

Figure 15a displays the evolution of the wind speed profile shown in Figure 10a from a different perspective. The three time periods with moderate wind speed at 20:00 on 26 April 01:00 and 21:00 on 27 April 2017 all clearly indicate strong wind shear with monochromatic wind speed increase with height in this figure. In contrast, the three weak wind cases show little wind shear or even slight wind reversal (06:00) between 1.83 and ~ 3.48 m. Figure 11b includes the SST to provide the temperature variation from the surface to ~ 3 m above. The difference between SST and the measured temperature at level three was shown in Figure 9. The thermal stability indicated by Figure 9 can be

seen here in Figure 15b as well. Based on this indication, we have weakly unstable cases at 20:00 on 26 April and 21:00 on 27 April, unstable at 11:00 on 27 April. The rest of the cases had stable stratification. However, it is interesting to see that the thermal stratification is more complex than what is indicated by the bulk ASTD between the water surface and the measurements at 3.07 m. First, the strongest gradient is between the lowest measurement level and the sea surface; this is an expected result from MOST. However, the vertical gradients of θ between adjacent levels in the atmosphere were very weak or each change signs from one layer to the other, which occurred on all profiles except for 16:00 on 27 April. It appears that θ decreases slightly with height between level two and level three irrespective of its gradient below, indicating somewhat persistent near-neutral thermal stratification within the air column at very low levels although strong thermal stratification may be present below. This observation suggests potential uncertainties if the atmospheric thermal stability is defined based on measurements within the atmosphere only without the SST information. Similar complexity is observed in the vertical profiles of specific humidity as seen in Figure 15c. While one expects to observe decreasing moisture away from the sea surface, a few profiles show a slight increase or small change between 0.77 and 1.54 m although decreases in q between 1.54 and 3.07 m were persistently observed with the exception at 16:00 on 27 April. Similar to temperature, the largest gradients in q are near the surface. The lack of vertical gradients in the layer between 0.77 and 3.01 m resulted in little change in the modified refractivity (M), as shown in Figure 15d.

2. MASFlux Measurements vs MOST Profiles

In this section, validity of MOST is examined using the MASFlux measurements. The discussions here includes the deviation of the MOST profiles from MASFlux measurements as well as surface fluxes derived from MOST in comparison with those calculated from MASFlux using the eddy correlation method.

The measurements from the MASFlux buoy, averaged in 30-minute intervals, different levels were used as input to the modified COARE surface flux algorithm to generate vertical profiles and surface fluxes following MOST. This calculation was

made for pairs of wind and T/RH measurements. Since there were three levels of usable T/RH measurements and three levels of wind measurements at similar altitudes, the input to COARE was grouped in three combined levels: level x (x being one, two, or three) implies using both T/RH and wind measurements from their respective level x measurements. Figures 16 and 17 show examples of the profile comparisons from stable (01:00 on 27 April) and unstable (11:00 on 27 April) periods, respectively. Each figure includes the MASFlux measurements as well as COARE profiles calculated using all three combination levels. Potential temperature (θ), specific humidity (q), wind speed, and modified refractivity (M) are each shown. The circles indicate the measured variables while the curved lines indicate the calculated COARE profiles.

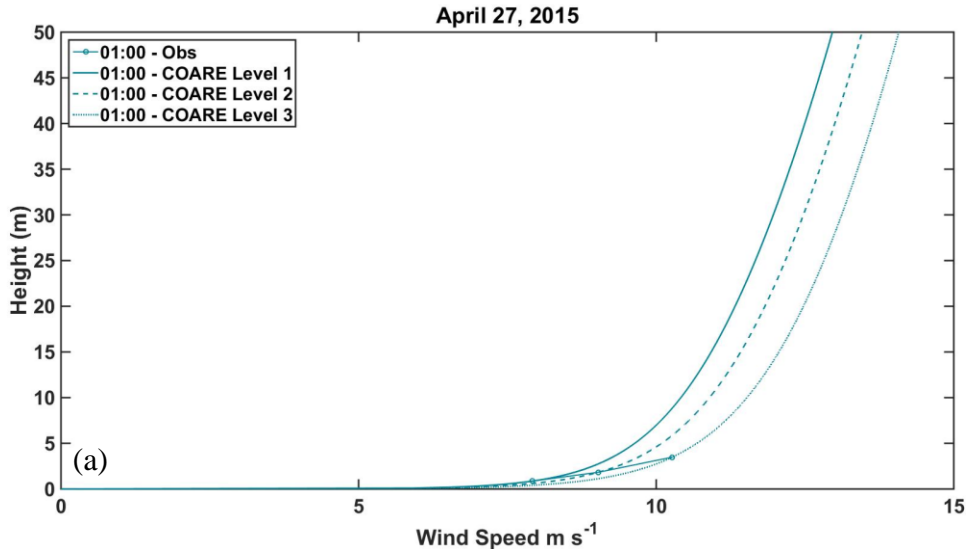


Figure 16. COARE Profiles during a Period of Stable Thermal Stratification (01:00) with Inputs from Measurement Levels One to Three. (a) Wind Speed, (b) Potential Temperature, (c) Specific Humidity, (d) Modified Refractivity.

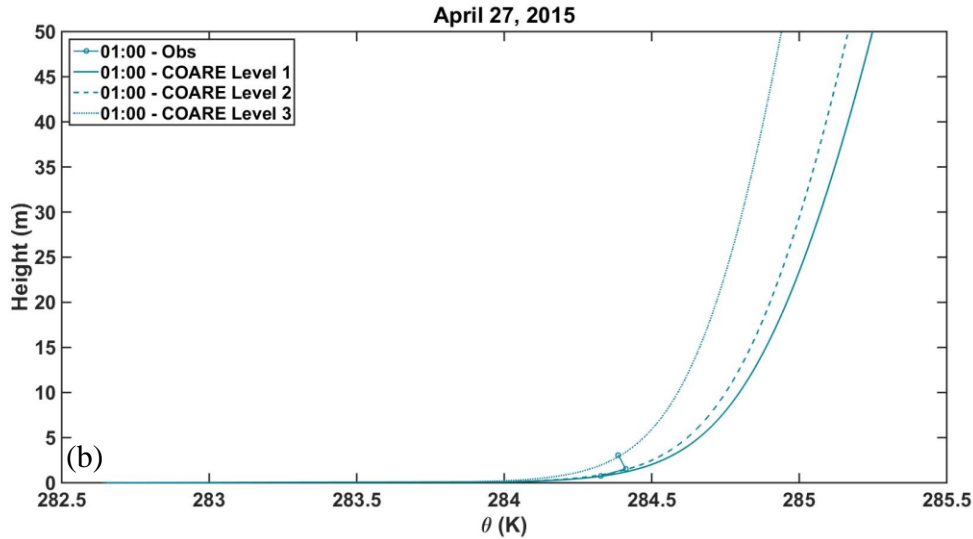


Figure 16. COARE Profiles during a Period of Stable Thermal Stratification (01:00) with Inputs from Measurement Levels One to Three. (a) Wind Speed, (b) Potential Temperature, (c) Specific Humidity, (d) Modified Refractivity. (Continued).

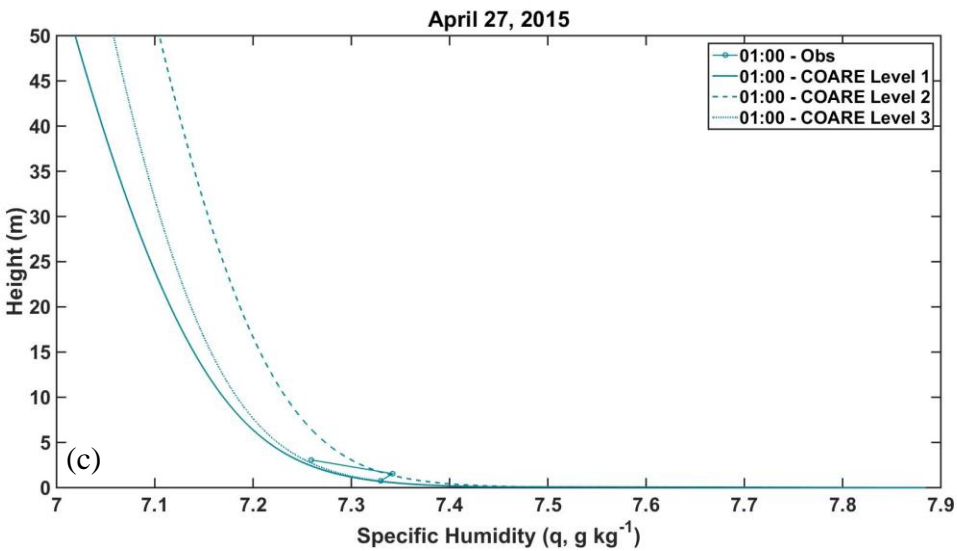


Figure 16. COARE Profiles during a Period of Stable Thermal Stratification (01:00) with Inputs from Measurement Levels One to Three. (a) Wind Speed, (b) Potential Temperature, (c) Specific Humidity, (d) Modified Refractivity. (Continued).

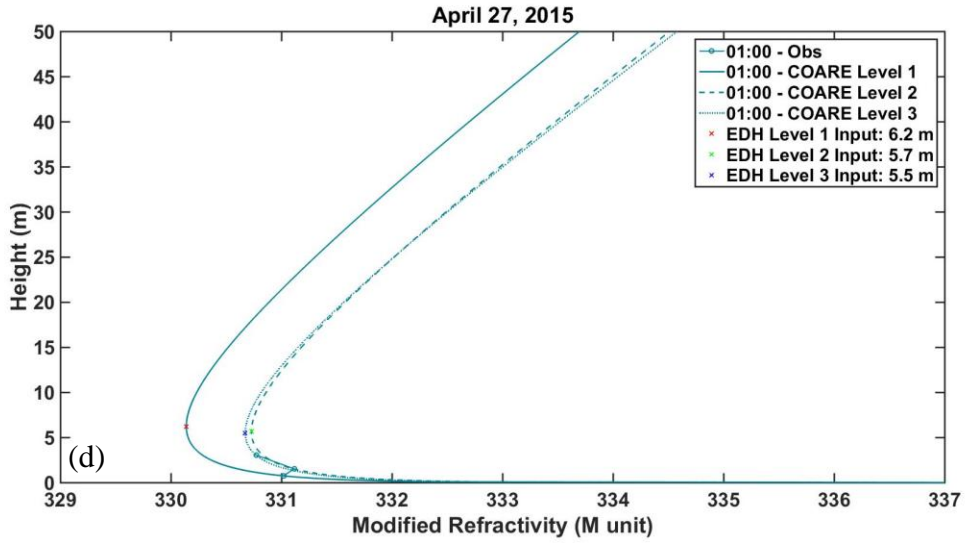


Figure 16. COARE Profiles during a Period of Stable Thermal Stratification (01:00) with Inputs from Measurement Levels One to Three. (a) Wind Speed, (b) Potential Temperature, (c) Specific Humidity, (d) Modified Refractivity. (Continued).

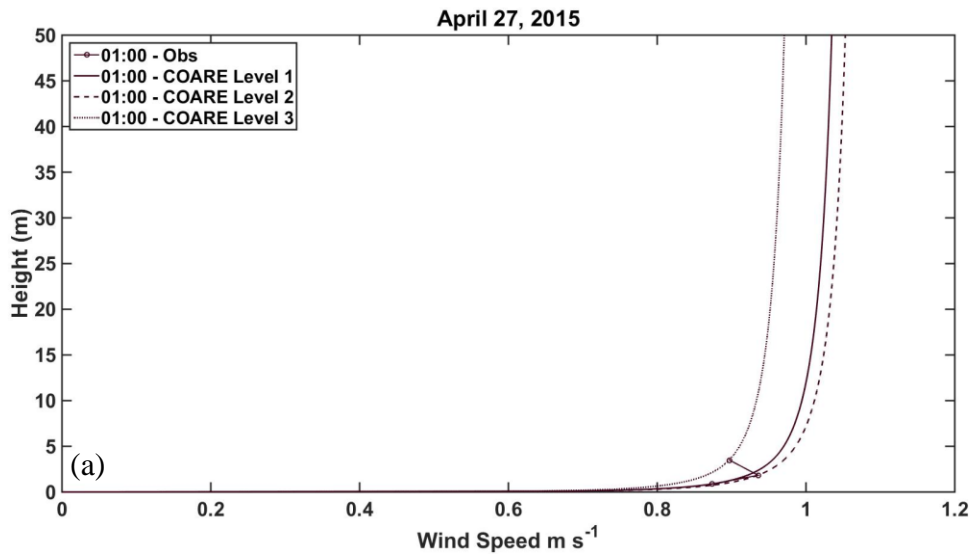


Figure 17. COARE Profiles during a Period of Unstable Thermal Stratification (11:00) with Inputs from Measurement Levels One to Three. (a) Wind Speed, (b) Potential Temperature, (c) Specific Humidity, (d) Modified Refractivity

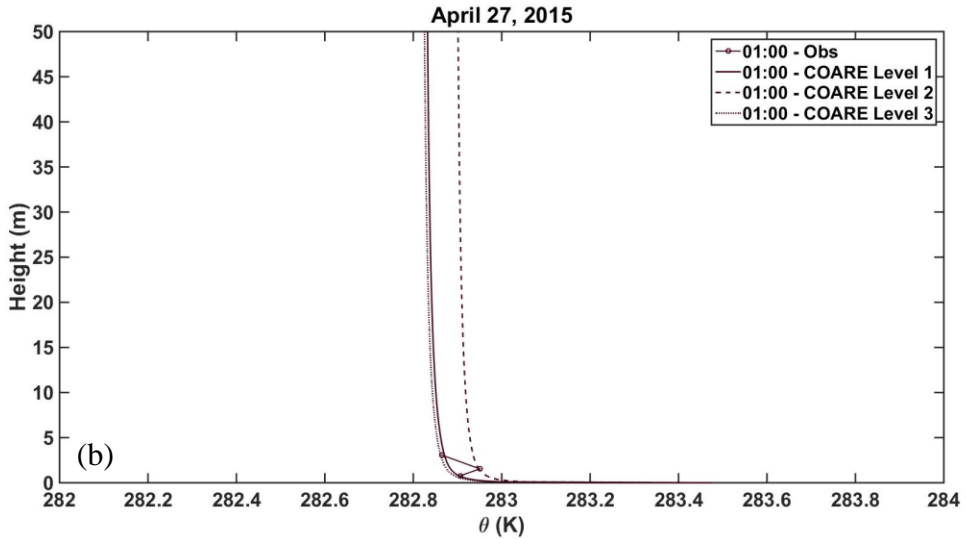


Figure 17. COARE Profiles during a Period of Unstable Thermal Stratification (11:00) with Inputs from Measurement Levels One to Three. (a) Wind Speed, (b) Potential Temperature, (c) Specific Humidity, (d) Modified Refractivity. (Continued).

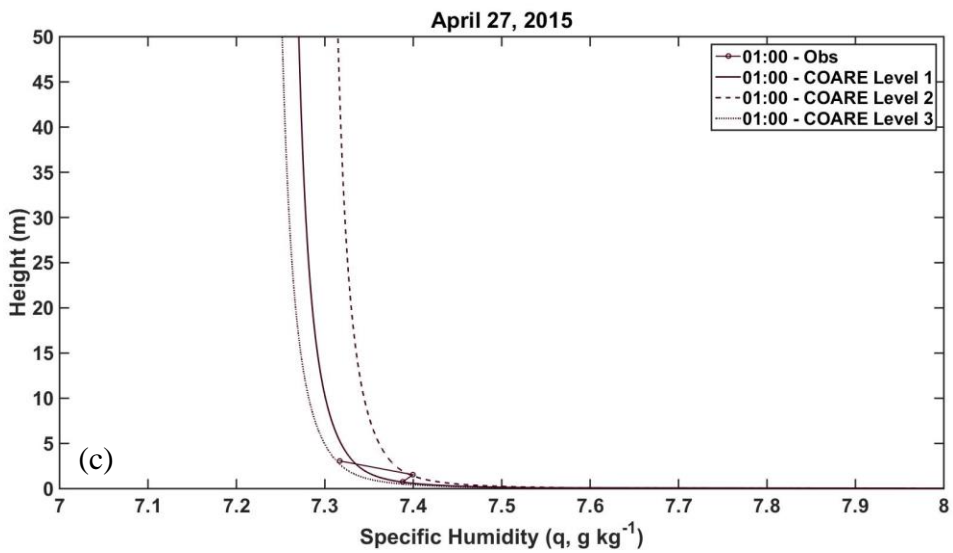


Figure 17. COARE Profiles during a Period of Unstable Thermal Stratification (11:00) with Inputs from Measurement Levels One to Three. (a) Wind Speed, (b) Potential Temperature, (c) Specific Humidity, (d) Modified Refractivity. (Continued).

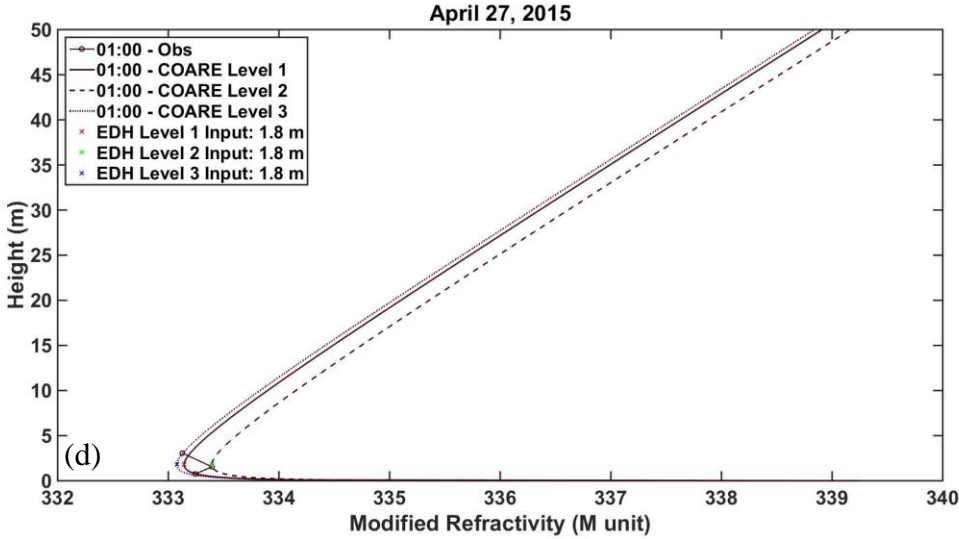


Figure 17. COARE Profiles during a Period of Unstable Thermal Stratification (11:00) with Inputs from Measurement Levels One to Three. (a) Wind Speed, (b) Potential Temperature, (c) Specific Humidity, (d) Modified Refractivity. (Continued).

Both Figures 16 and 17 show different COARE profiles when inputs were taken from different levels. This is an indication that the measured vertical profiles do not exactly follow the COARE profile (also referred to as the MOST profiles). On Figure 16d and 17d, the evaporation duct heights were also indicated on the M profiles. The area of measurements off the central coast of California is normally represented by shallow EDH, which is clearly seen in the results here. The EDH during the stable period varied between 5.5 and 6.2 m using different input levels while the unstable condition has an EDH of only 1.8 m and did not show a variation when different input levels were used. It should be noted, however, that the M profiles take different shapes in spite of the same magnitude of EDH. Their impact on EM propagation hence is still different.

To quantify the discrepancies of the MOST profiles from measurements, the difference between the COARE profiles and the measurements was obtained in the following way: Bulk measurements were collected at 0.77 m, 1.54 m, and 3.07 m for temperature and humidity and 0.87 m, 1.83 m, 3.48 m for wind speed. The COARE algorithm produces the vertical variation at 0.1 m vertical intervals. To compare the bulk measurements with the predicted profile, the observed 0.77 m measurement was compared with the COARE calculated value at 0.8 m, the 1.54 m observed measurement

was compared with the 1.5 m calculation and the 3.07 m bulk measurement was compared with the 3.1 m calculation. Similarly for wind speed the 0.87 m measurement was compared with the 0.9 m calculation, the 1.83 m measurement was compared with the 1.8 m measurement, and the 3.48 m measurement was compared with the 3.50 m calculation. The differences are considered errors in the generated COARE profiles. These definitions of errors are illustrated in Figure 18.

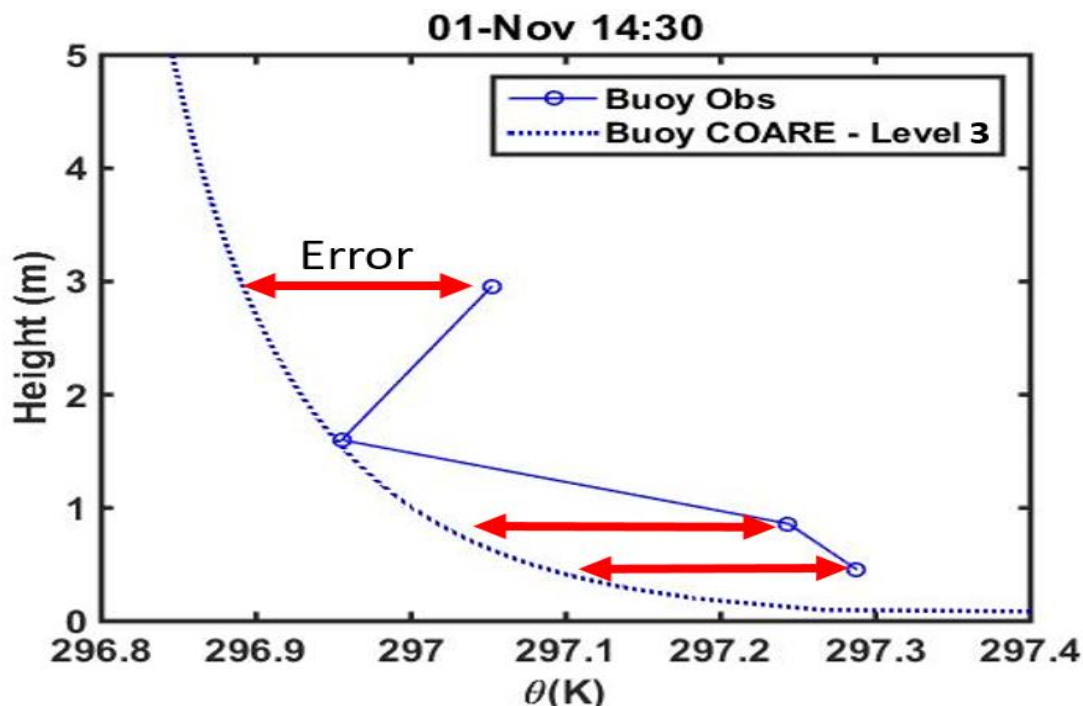


Figure 18. Example Error Plot Calculation.

The mean difference for temperature, specific humidity, wind speed, and modified refractivity for each 30-minute average intervals between the model and observation point was taken at each of the other levels. The results are shown in Figures 19 through 22 for the entire time period of MASFlux measurements on 26 – 27 April 2015. Each Figure describes the temperature, specific humidity, wind speed, or modified refractivity for the specified measurement input.

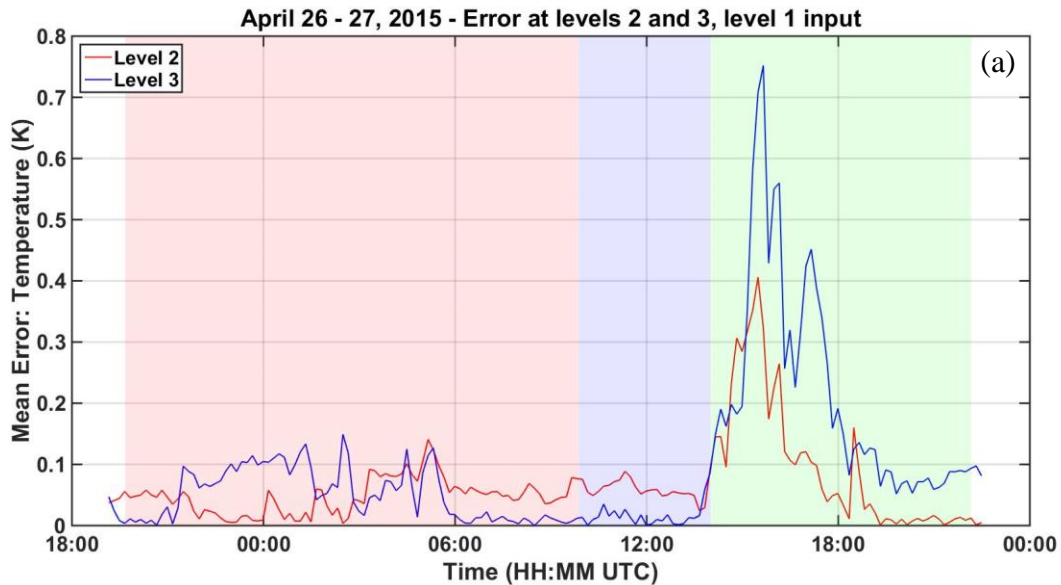


Figure 19. COARE Profile Error in Temperature. (a) Level One Input, (b) Level Two Input, (c) Level Three Input.

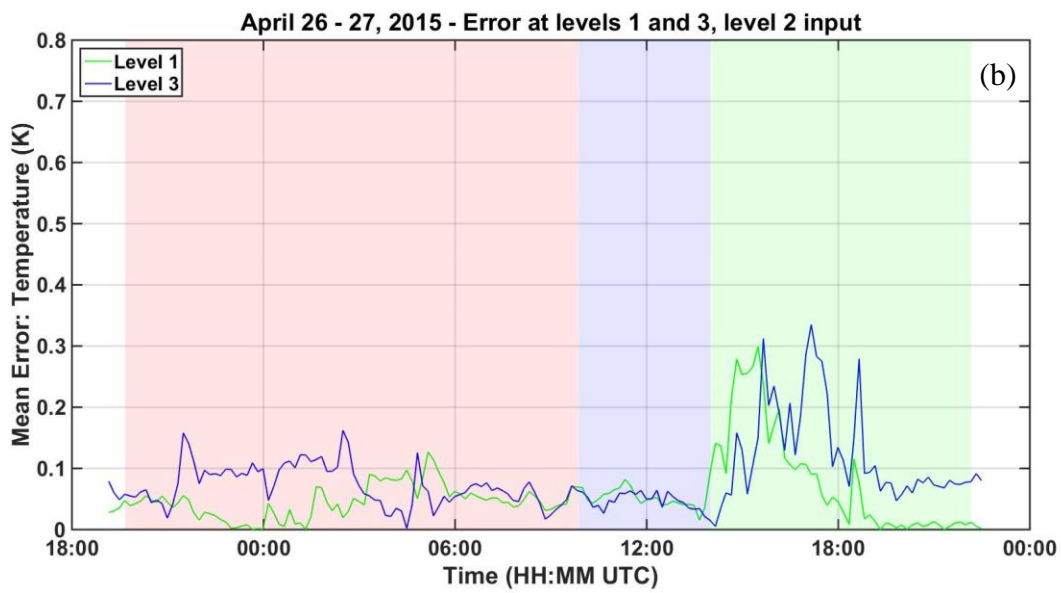


Figure 19. COARE Profile Error in Temperature. (a) Level One Input, (b) Level Two Input, (c) Level Three Input. (Continued).

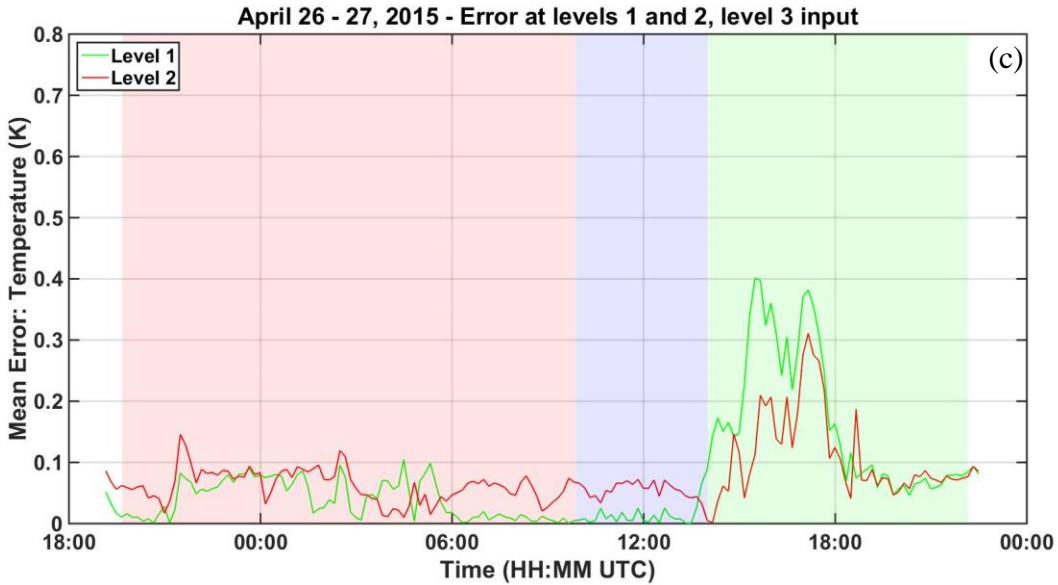


Figure 19. COARE Profile Error in Temperature. (a) Level One Input, (b) Level Two Input, (c) Level Three Input. (Continued).

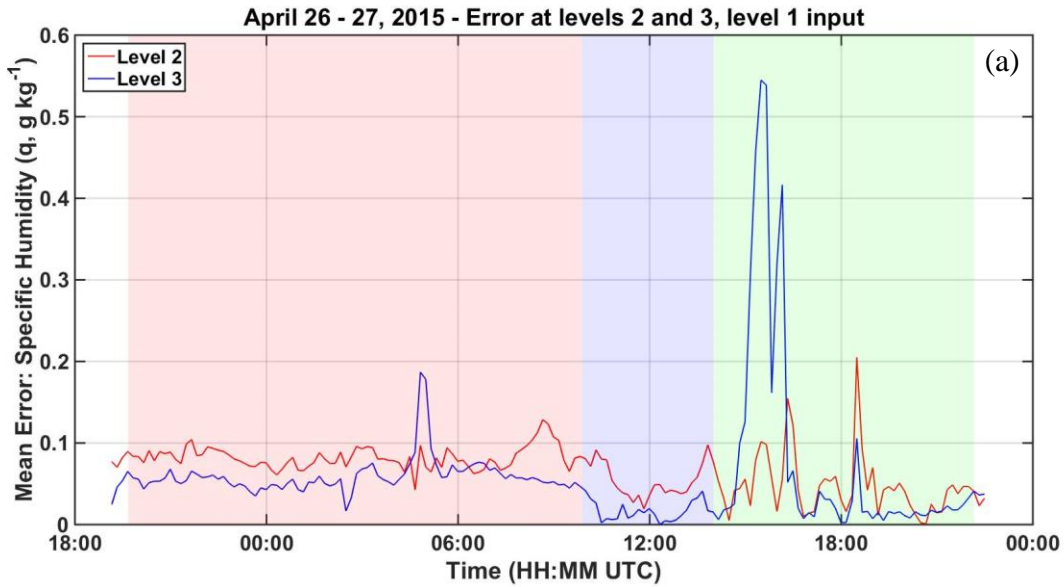


Figure 20. COARE Profile Error in Specific Humidity. (a) Level One Input, (b) Level Two Input, (c) Level Three Input.

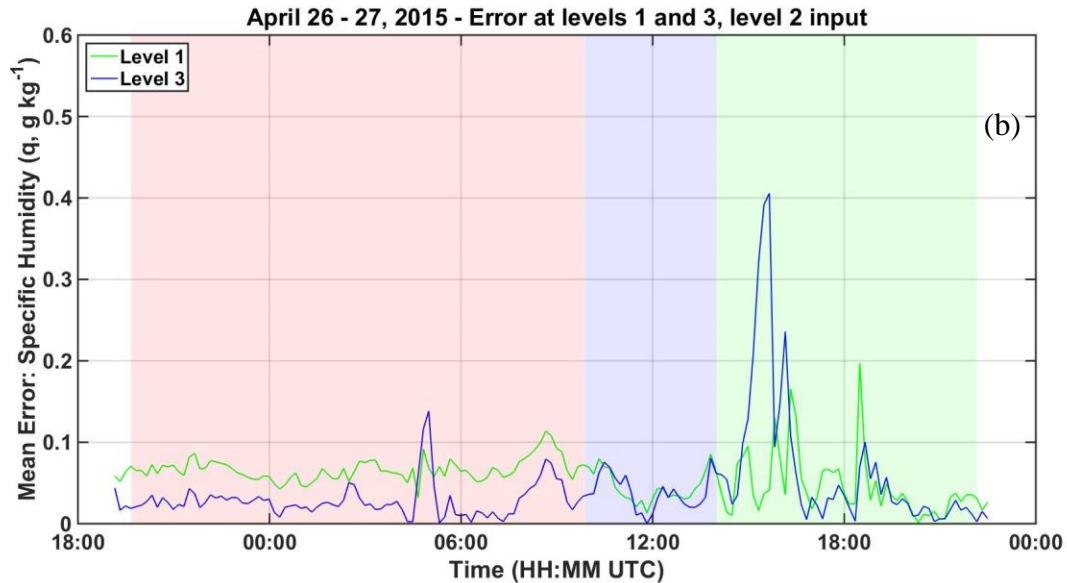


Figure 20. COARE Profile Error in Specific Humidity. (a) Level One Input, (b) Level Two Input, (c) Level Three Input. (Continued).

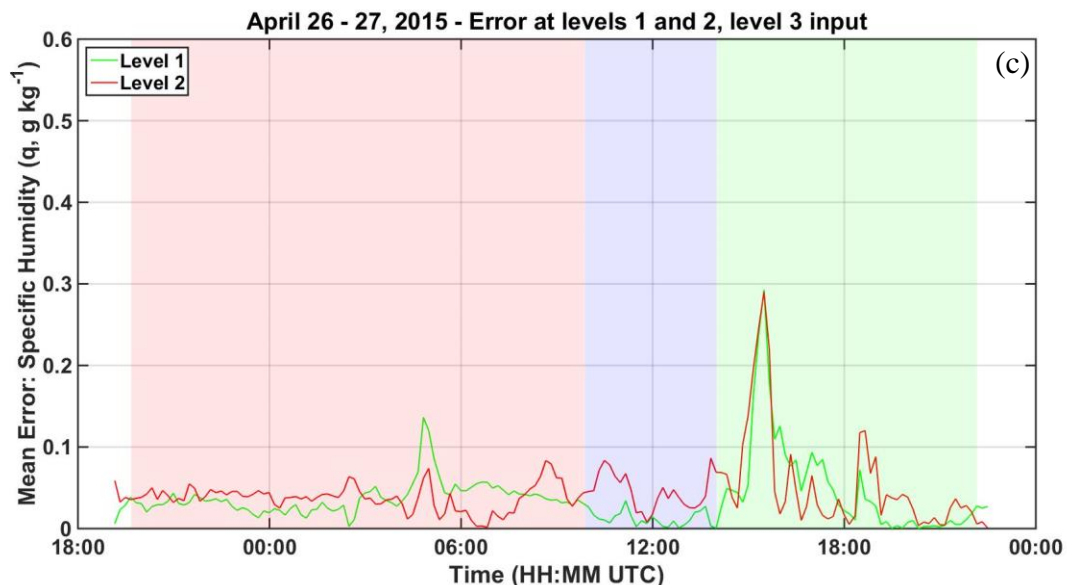


Figure 20. COARE Profile Error in Specific Humidity. (a) Level One Input, (b) Level Two Input, (c) Level Three Input. (Continued).

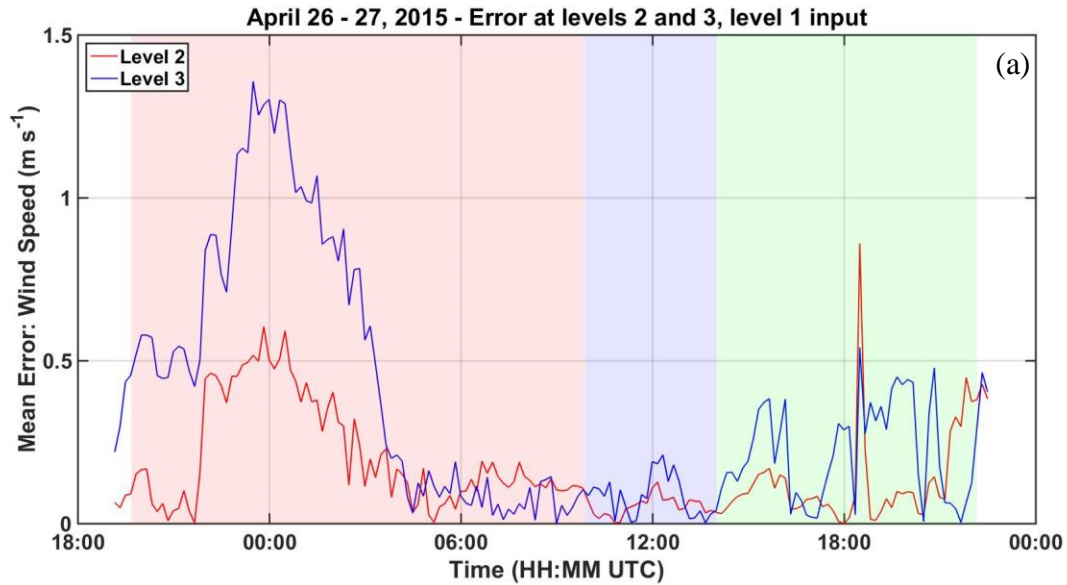


Figure 21. COARE Profile Error in Wind Speed. (a) Level One Input, (b) Level Two input, (c) Level Three Input.

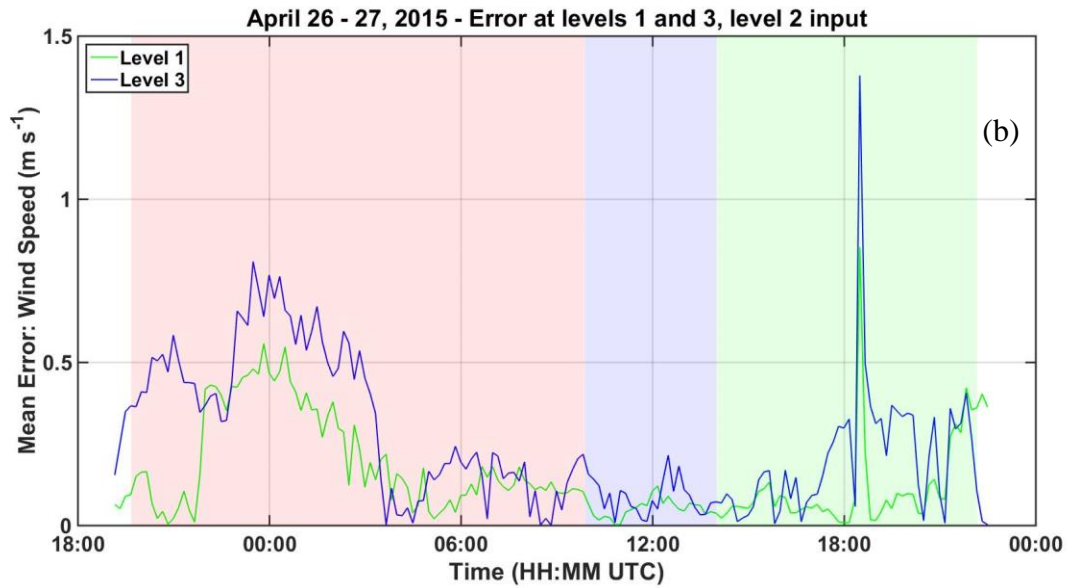


Figure 21. COARE Profile Error in Wind Speed. (a) Level One Input, (b) Level Two input, (c) Level Three Input. (Continued).

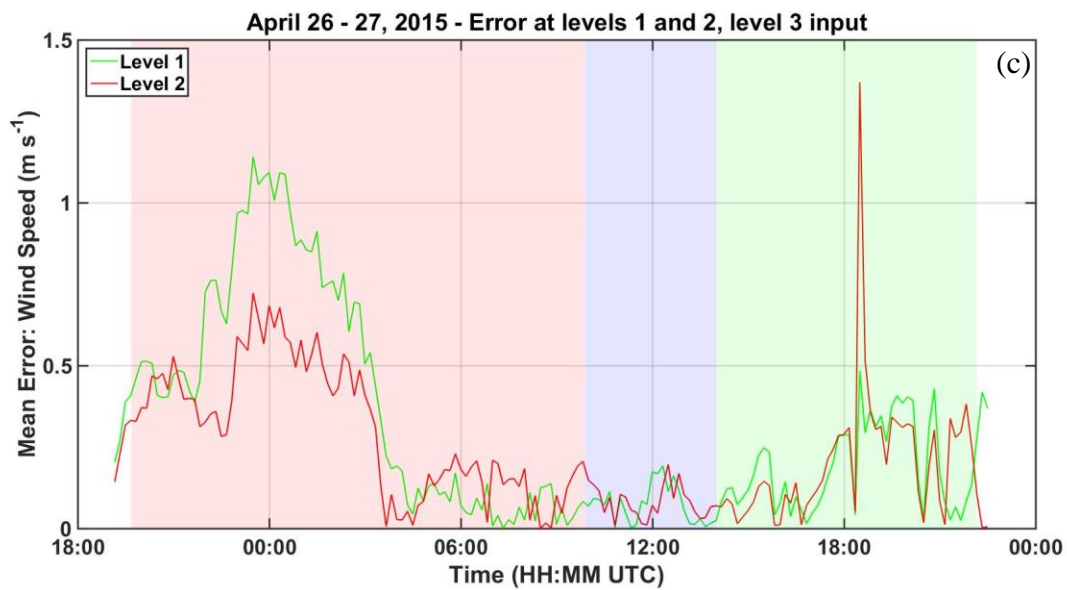


Figure 21. COARE Profile Error in Wind Speed. (a) Level One Input, (b) Level Two input, (c) Level Three Input. (Continued).

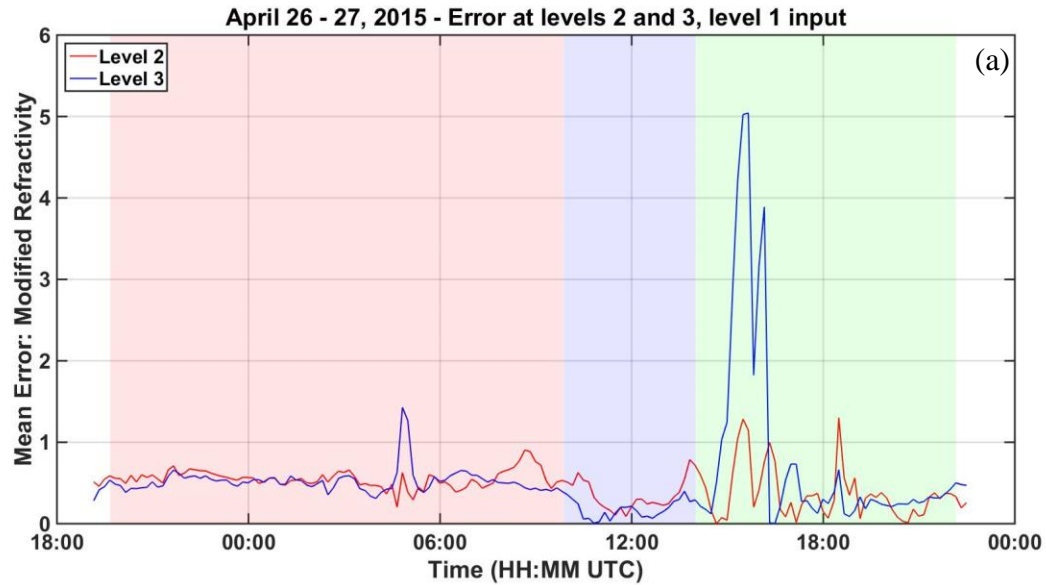


Figure 22. COARE Profile Error in Modified Refractivity. (a) Level One Input, (b) Level Two input, (c) Level Three Input.

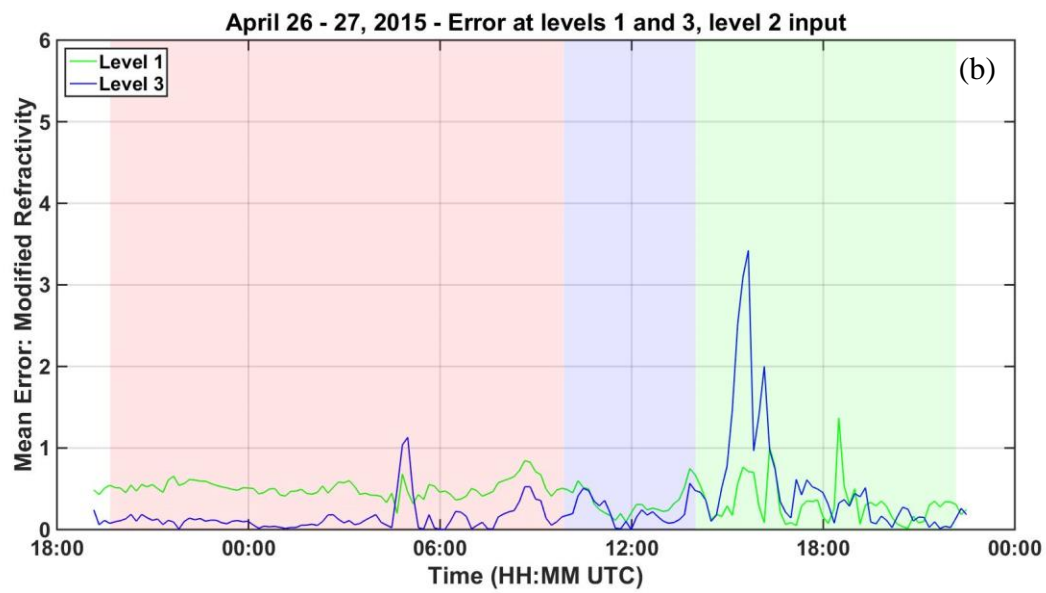


Figure 22. COARE Profile Error in Modified Refractivity. (a) Level One Input, (b) Level Two input, (c) Level Three Input. (Continued).

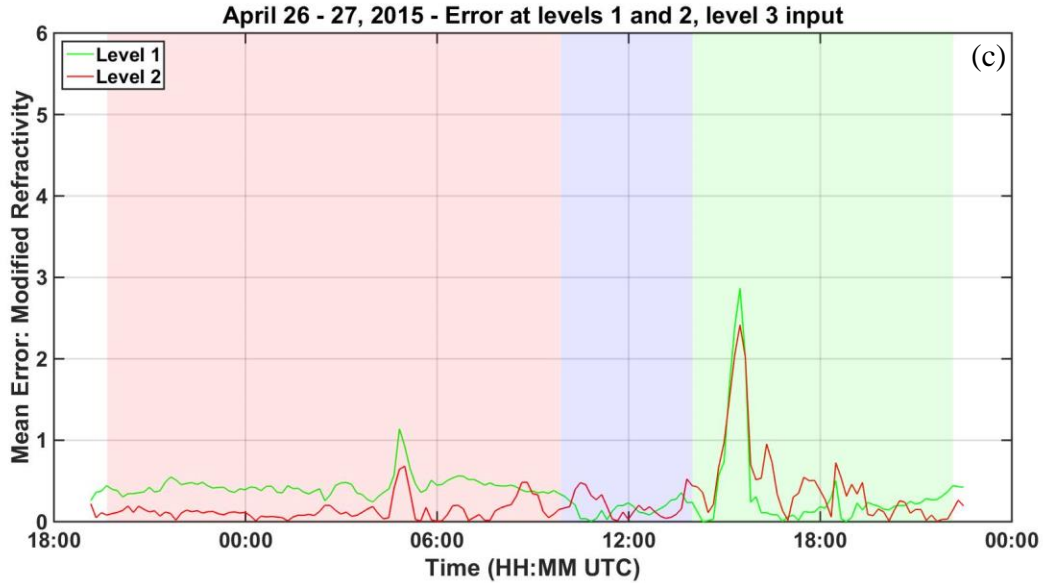


Figure 22. COARE Profile Error in Modified Refractivity. (a) Level One Input, (b) Level Two input, (c) Level Three Input. (Continued).

Figures 19 through 22 show difference error variability in wind and in scalars (temperature, humidity, and the derived M). A time period of stable conditions was defined from April 26, 2015, at 20:13 until April 27, 2015, at 06:58. A time period of unstable conditions was defined from April 27, 2015, at 06:58 until April 27, 2015, at 14:46. This can be seen in Figure 9 where the stability plot crosses zero on the x-axis. Table 5 compares the mean error from each input level with the other two levels for both the stable strong wind, stable weak wind, and unstable time periods.

Table 5. Level One (a), Two (b), and Three (c) Mean Error Compared with other Levels for the Stable and Strong Wind Condition, Stable and Weak Wind Condition, and Unstable Condition.

Level 1 Input (a)			
θ (K)			
	Stable & Strong Wind	Stable & Weak Wind	Unstable
Level 2	0.0476	0.0974	0.0590
Level 3	0.0520	0.2155	0.0167
Specific Humidity (g kg^{-1})			
Level 2	0.0819	0.0474	0.0541
Level 3	0.0592	0.0784	0.0164
Wind Speed (m s^{-1})			
Level 2	0.2192	0.1289	0.0535
Level 3	0.4988	0.2223	0.0838
Modified Refractivity (M units)			
Level 2	0.5521	0.3706	0.3506
Level 3	0.5222	0.8138	0.1746

Level 2 Input (b)			
θ (K)			
	Stable & Strong Wind	Stable & Weak Wind	Unstable
Level 1	0.0457	0.0819	0.0521
Level 3	0.0713	0.1256	0.0496
Specific Humidity (g kg^{-1})			
Level 1	0.0664	0.0468	0.0456
Level 3	0.0321	0.0643	0.0409
Wind Speed (m s^{-1})			
Level 1	0.2079	0.1157	0.0522
Level 3	0.3414	0.2154	0.0866
Modified Refractivity (M units)			
Level 1	0.5077	0.3232	0.3422
Level 3	0.1530	0.5380	0.2178

Level 3 Input (c)			
θ (K)			
	Stable & Strong Wind	Stable & Weak Wind	Unstable
Level 1	0.0396	0.1669	0.0153
Level 2	0.0617	0.1124	0.0534
Specific Humidity (g kg^{-1})			
Level 1	0.0374	0.0502	0.0120
Level 2	0.0378	0.0548	0.0456
Wind Speed (m s^{-1})			
Level 1	0.4339	0.1890	0.0743
Level 2	0.3096	0.2057	0.0819
Modified Refractivity (M units)			
Level 1	0.4318	0.3599	0.1662
Level 2	0.1382	0.4536	0.2051

Examining both the input level and the stability and wind regime provides insights to the conditions when MOST is most problematic. Table 5 shows that input from the lowest level (level one) produces the largest error in the modified refractivity profiles, while level three input produces the lowest error. The errors in MOST profiles varied substantially with wind speed and thermal stability. The smallest errors are seen in the unstable condition. The stable condition with weak winds produces the highest error; the stable condition with strong winds is slightly more accurate.

3. Surface Flux, Evaporation Duct Properties, and SST Correction

In this section, the COARE parameterized surface fluxes are compared to the direct flux measurements shown in Figure 23. Momentum flux varied most significantly throughout the measurement period with the maximum magnitude corresponding to the wind maximum. In general, the COARE algorithm underestimated the magnitude of the momentum flux (MF). Such behavior does not seem to be associated with the thermal stability although the strong wind and stable period near 00:00 of 27 April show significant variability for input from the different levels, an indication of deviation from the assumption of the constant flux layer under MOST. During the long period of relatively weak wind following the frontal passage (06:00 – 18:00 on 27 April), the

parameterized MF is not sensitive to the choice of measurement levels, which is a significant contrast to the strong wind period. This is likely associated with weak wind shear in the low-wind period shown in Figure 10a.

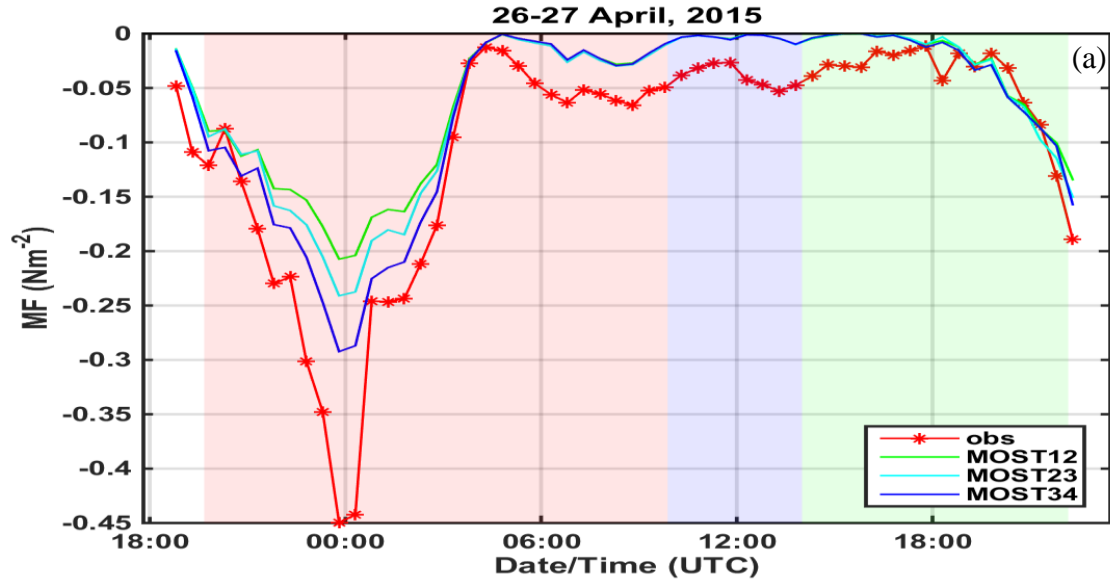


Figure 23. Comparison of Measured and COARE Parameterized Surface Fluxes. (a) Momentum Flux, (b) Sensible Heat Flux, (c) Latent Heat Flux.

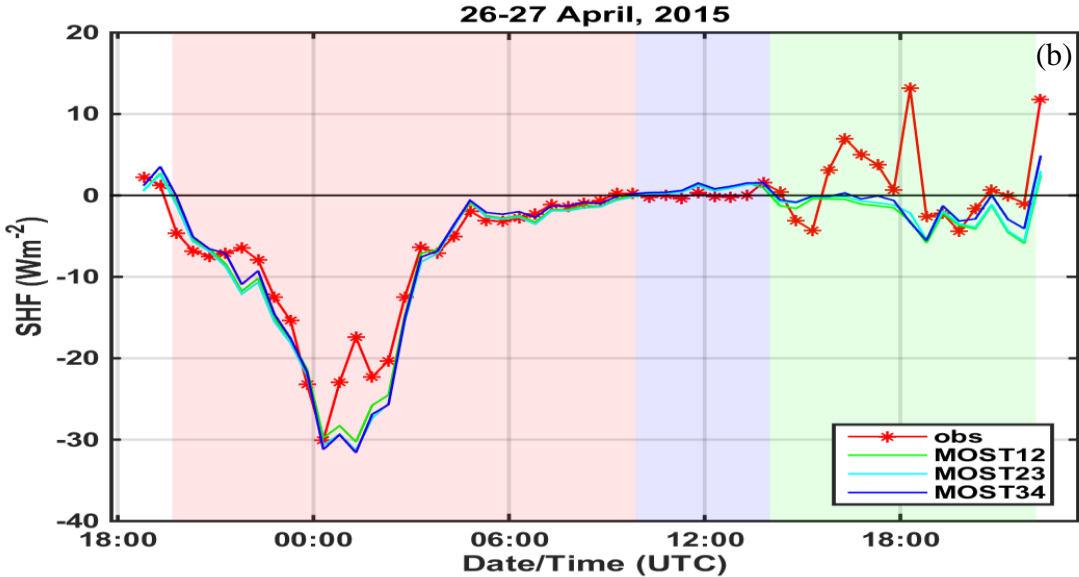


Figure 23. Comparison of Measured and COARE Parameterized Surface Fluxes. (a) Momentum Flux, (b) Sensible Heat Flux, (c) Latent Heat Flux. (Continued).

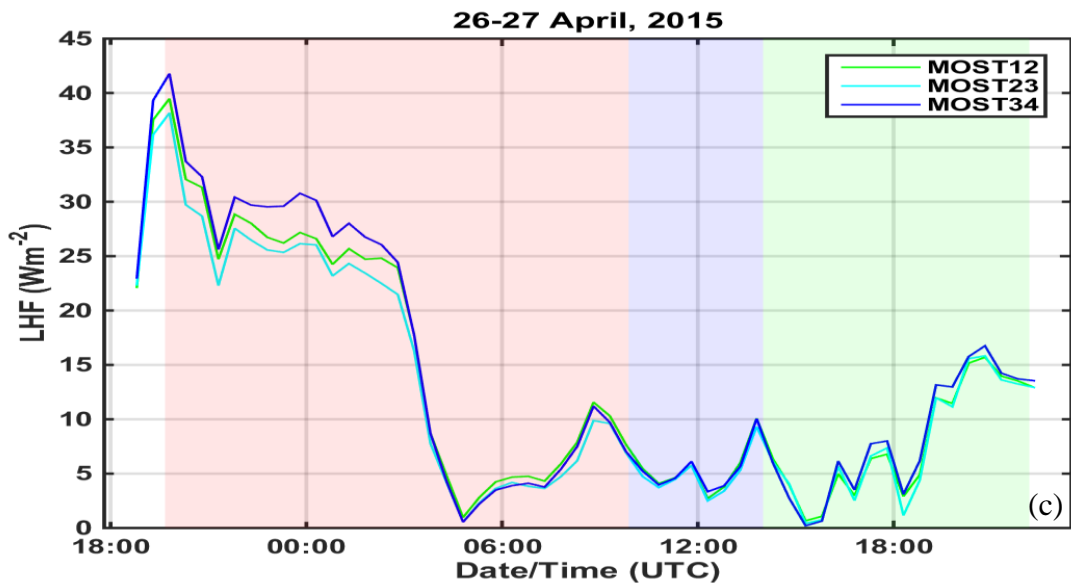


Figure 23. Comparison of Measured and COARE Parameterized Surface Fluxes. (a) Momentum Flux, (b) Sensible Heat Flux, (c) Latent Heat Flux. (Continued).

The sensible heat flux was represented fairly well by the COARE algorithm during the strong wind stable and unstable periods with the exception during about a two-hour period following the strongest near-surface wind. It will be discussed later that this

apparent discrepancy is a result of overly corrected SST. During the period of weak wind and stable stratification between 14:00 – 18:00 on 27 April, the observed SHF shows small and variable values that were at times not consistent with the expected negative heat fluxes in stable conditions. Further data quality control should be made to this portion of the data in the future to ensure measurement quality in the weak turbulence regime.

Latent heat flux was not measured on the MASFlux buoy. The parameterized latent heat flux (LHF) shows large magnitudes of upward LHF during the period of high wind and decrease dramatically as the wind speed transitioned to low-wind. The large LHF reaching 40 Wm^{-2} was rarely seen over the cold water of the Monterey Bay (Wang and Kalogiros 2011) especially in stable stratifications.

Figure 24 shows the evaporation duct height (EDH) and strength (EDS) derived from the COARE model using input from the MASFlux measurements. Overall, evaporation ducts in this region is rather shallow and weak. Input from different altitude measurements resulted in similar ED properties except for the periods shaded in darker red or green where model results are highly variable in both EDH and EDS. Further examination indicated that these periods both occurred in low wind and stable conditions (Figure 24c). A threshold of wind speed is visually identified to be 3.4 ms^{-1} shown in the black dash line. The combined low wind and stable stratification resulted in the minimum turbulent kinetic energy shown in Figure 24d. It is worth noting, though, that the ED model does not have similar problems in the unstable condition with similar magnitude of turbulent kinetic energy (TKE) at around 12:00 on 27 April.

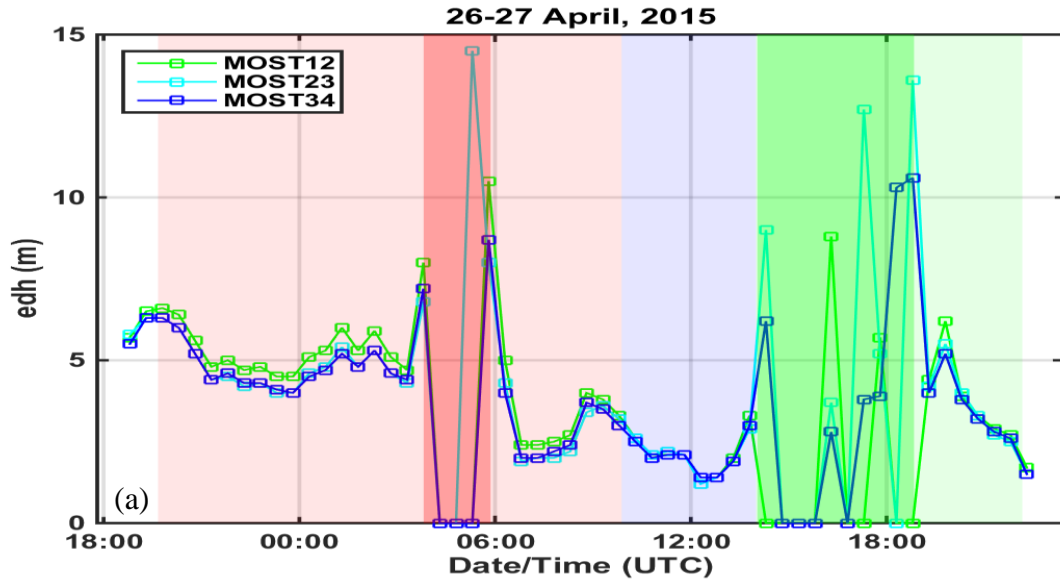


Figure 24. Evaporation Duct Height (a) and Duct Strength (b) Derived from the Modified COARE Algorithm; and Corresponding Wind Speed Variability (c), and Turbulent Kinetic Energy (d).

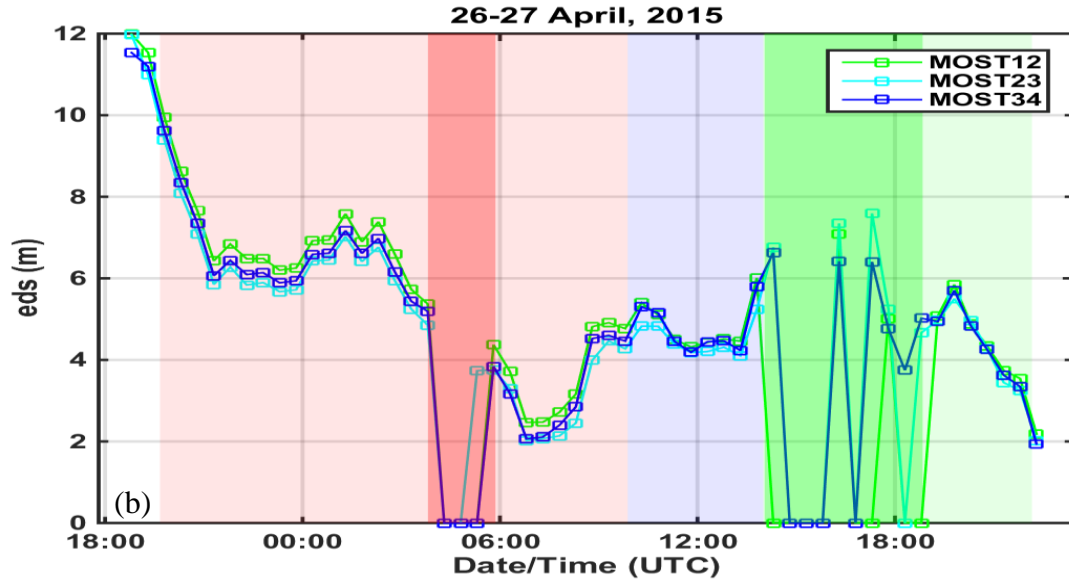


Figure 24. Evaporation Duct Height (a) and Duct Strength (b) Derived from the Modified COARE Algorithm; and Corresponding Wind Speed Variability (c), and Turbulent Kinetic Energy (d). (Continued).

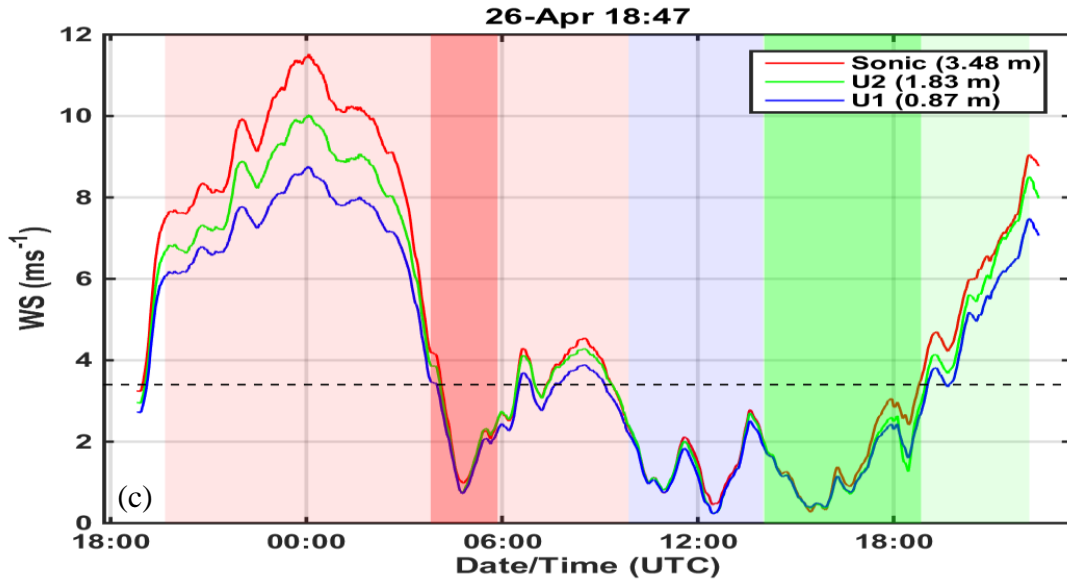
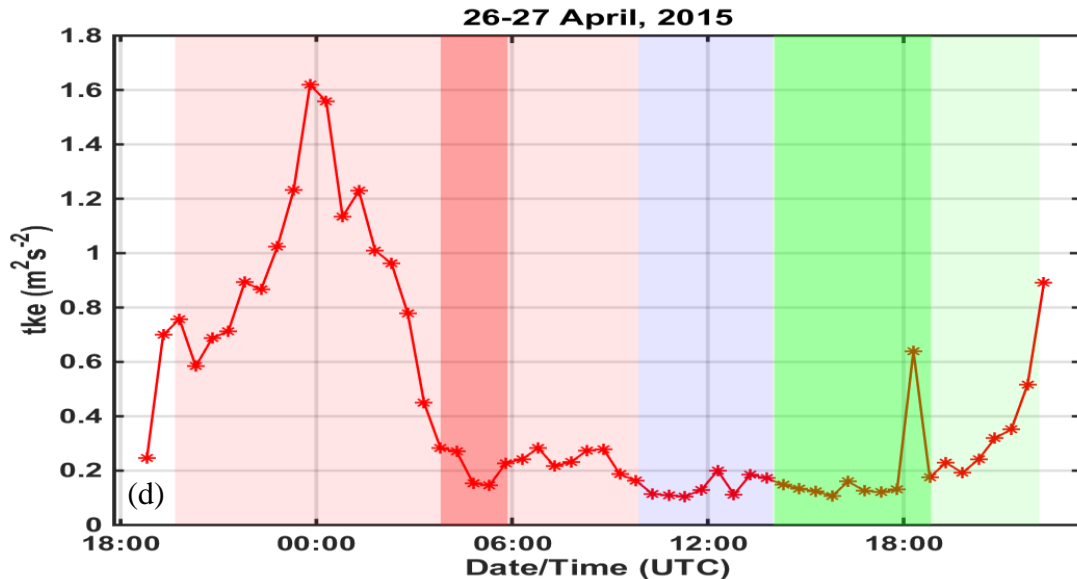


Figure 24. Evaporation Duct Height (a) and Duct Strength (b) Derived from the Modified COARE Algorithm; and Corresponding Wind Speed Variability (c), and Turbulent Kinetic Energy (d). (Continued).



The darker shaded red and green time period indicate periods of weak wind and stable thermal stability.

Figure 24. Evaporation Duct Height (a) and Duct Strength (b) Derived from the Modified COARE Algorithm; and Corresponding Wind Speed Variability (c), and Turbulent Kinetic Energy (d). (Continued).

Figure 25 shows the impact of SST on the modeled SHF. Top layer water temperature was measured on the MASFlux at 3, 16, and 41 cm below the water surface. Because of the waves and the buoy motion, the exact depth of these sensors may vary during the measurements. In the case of measurements on 26 – 27 April, the temperature probe at the top level malfunctioned. We hence used the measurements at 16 cm below to represent the sea surface temperature with the idea that a correction is likely needed since the temperature at depth may not represent the skin temperature of the water surface due to the cool skin effects (Fairall et al. 2003). The correction was made using the assumption that the measured air-sea temperature should be zero when the measured SHF is zero. We hence identified a -0.4°C correction that should be applied to the water temperature at 16 cm depth to represent the sea surface skin temperature. Figure 25 shows a comparison between the COARE SHFs before and after the correction and in comparison with the measured SHF. The correction resulted in about a 3 W m^{-2} reduction in the COARE SHF. Additionally, the corrected SST resulted in an overestimate of SHF between 00:50 and 02:50 on 27 April, about one hour after the maximum wind forcing to the ocean. In contrast, the SHF without the correction seems to represent the measured SHF well. This result suggests that a correction for this period is not needed. This is reasonable result as the strong wind-forced mixing in the upper ocean may have eliminated the cool skin layer in this case. The results shown earlier in this chapter used the corrected SST.

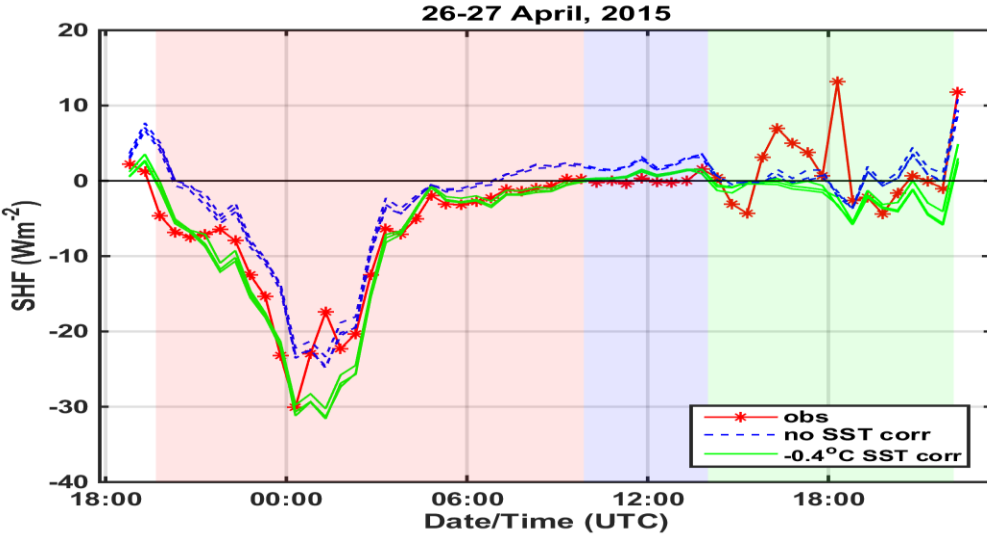


Figure 25. SHF from the COARE Model with and without Correction of the SST.

B. CASPER-EAST

1. Gulf Stream and continental shelf analysis

The location of CASPER-East was strategically selected to allow different meteorological and oceanographic conditions to be observed. As discussed in Chapter III, the MASFlux buoy was deployed in two modes: one was for long hours at either Point A1 or Point A2, one was for short term deployments tethered to the R/V Sharp. The latter deployment mode allows the combination of ship and buoy measurements to extend beyond the buoy measurement level to about 12 m above the surface on the ship bow mast. Each measurement duration was relatively short (30-min to 1-hour long). These measurements will be analyzed in this chapter. Figure 26 shows the location and SST of all MASFlux deployments when tethered to R/V Sharp. These include deployments over the Gulf Stream from 30 October – 1 November, 2015 and over the continental shelf on 3 November 2015. Figure 26 shows that the SST over the shelf region (deployments 13 to 16) was between 18 and 19 °C. Figure 26 shows more detail of the CASPER-East deployments number 7 – 12 over the Gulf Stream. Due to the strong GS currents, the ship/buoy drifted with the currents for a distance of 8 – 10 km. The spatial variability along the path was generally small. Deployment 7 was the only

measurements on 30 October; it shows a mean SST of 20.4°C, clearly on the cold water side of the Gulf Stream. By 1 November, the GS front had move further northwest, all MASFlux deployments on the second and third Gulf Stream measurement days (30 October and 1 November) were made over the warm water region.

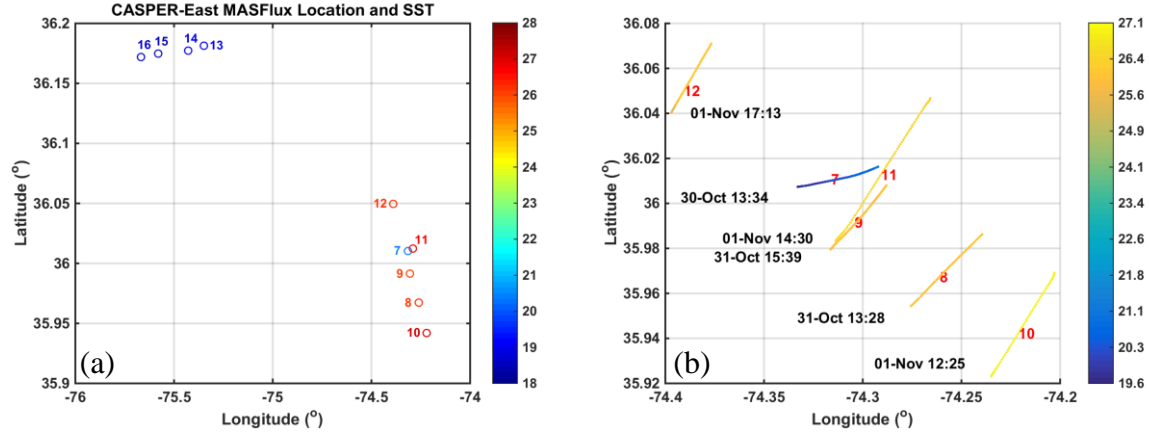


Figure 26. CASPER-East Deployment Map. (a) Legs 7 – 12, (b) Legs 10 – 12

The following discussions will be focused on the vertical profiles of mean and fluxes observed by the MASFlux buoy and the bow mast on R/V Sharp. Figures 27 through 32 show a comparison between the cases over the Gulf Stream (deployments 7 – 12) and over the continental shelf (deployments 13 – 16). The circles indicate MASFlux measurements and the green star is data from the mast of R/V Sharp. Subplots with a red line denote measurements over the warm water of the GS, while those with a blue line indicate measurements over the continental shelf. Comparing the cases over the Gulf Stream with warmer temperatures and a stronger current to the cases over the continental shelf with cooler temperature and a weaker current provided valuable results.

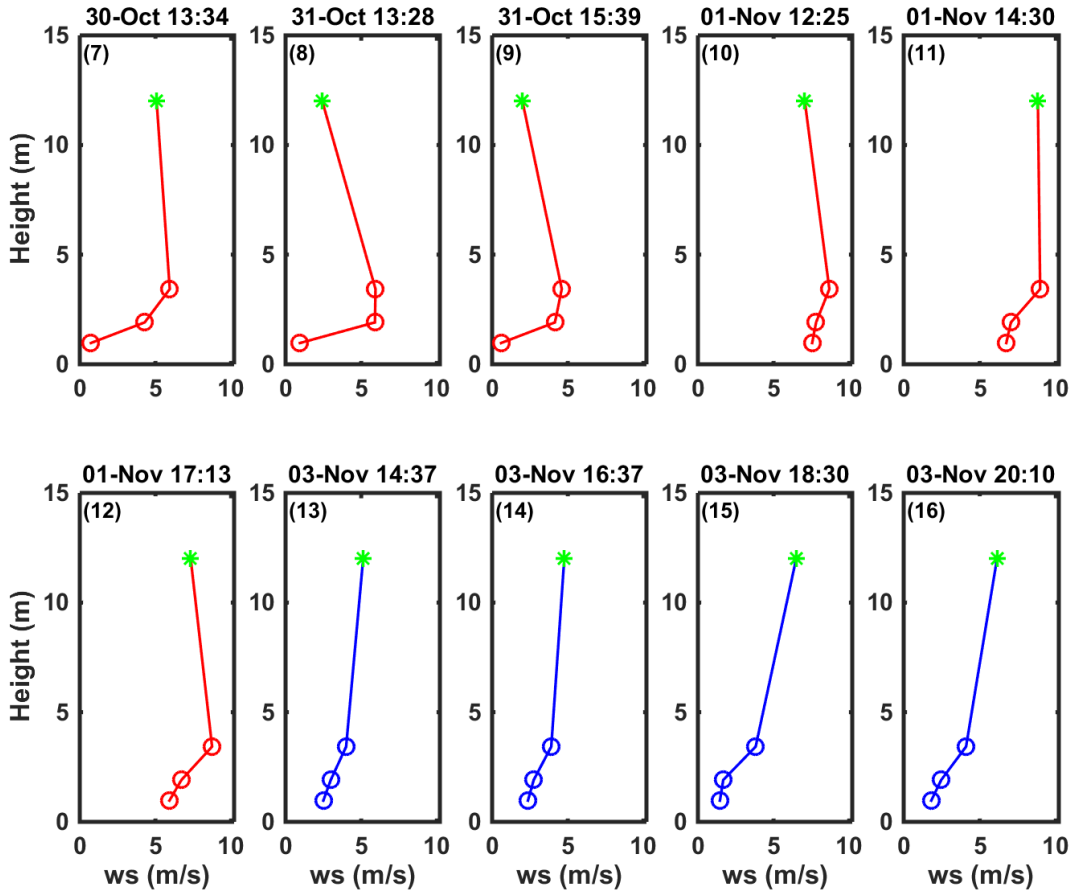


Figure 27. CASPER-East Deployments 7 – 16 Wind Comparison.

The mean wind variations between 0.87 and 12 m from the MASFlux buoy and the bow mast of R/V Sharp are given in Figure 27. Figure 27 shows that legs 7 – 12 indicate a near surface jet possibly associated with the Gulf Stream current and warmer temperatures. In these legs there is evidence of a near surface jet over the GS that is generally not present over the shelf region (legs 13 – 16). The full extent of the near surface jet was not observed in these cases because there is an altitude gap between the highest level of the MASFlux buoy and the mast of R/V Sharp. However, there is some evidence that the jet level is likely below 5 m above sea level (ASL) in deployments seven, eight and nine on 30 and 31 October. These are also low wind cases where the mean measured wind speed was less than 5 m s^{-1} at all levels. In comparison, the stronger wind cases observed on 1 November (deployments 10, 11, and 12) shows

monochromatic increase of the wind from the MASFlux. The peak of the wind profile is likely beyond the 3-D sonic anemometer level on the MASFlux and below the ship bow-mast level at 12 m. To further illustrate the above discussion, some of the key variables are summarized in Table 6 including the mean wind and potential temperature at the ship level (12 m), mean wind at the top of the buoy (3.43 m), mean potential temperature at the highest buoy level (2.95 m), and SST. The wind decrease from the top of the buoy to the ship mast ranges between 0.1 to 3.5 ms⁻¹ for cases over the GS. Over the shelf region, increases of the mean wind between the top of the buoy and the ship mast varied between 0.9 and 2.7 ms⁻¹. Additional research is required to better understand this feature and its likely cause associated with the swell and/or current.

Table 6. Mean wind speed, SST and potential temperature from R/V Sharp and MASFlux during CASPER-East.

Deploy - ment #	WS (ship)	WS (buoy3)	delta_WS	SST	θ (ship)	θ (buoy4)	SST - ship	SST - 04	Ship - 04
7	5.1	5.9	-0.9	292.47	292.86	293.84	-0.40	-1.37	0.98
8	2.4	5.9	-3.5	297.55	289.10	290.45	8.46	7.10	1.35
9	2.0	4.6	-2.6	297.51	289.59	290.62	7.91	6.89	1.02
10	7.1	8.7	-1.6	298.78	294.93	296.26	3.85	2.52	1.33
11	8.8	9.0	-0.1	298.33	295.58	297.05	2.75	1.28	1.47
12	7.3	8.7	-1.4	298.02	296.29	297.81	1.73	0.21	1.52
13	5.1	4.0	1.1	290.54	291.34	292.35	-0.80	-1.81	1.02
14	4.8	3.9	0.9	290.53	291.00	292.00	-0.47	-1.47	1.00
15	6.5	3.8	2.7	290.00	290.78	291.69	-0.78	-1.69	0.91
16	6.1	4.1	2.0	290.11	290.09	291.18	0.02	-1.07	1.09

The vertical variation of temperature, specific humidity, and the derived modified refractivity are shown in Figures 28 through 30, respectively. In addition to the ship mast and buoy measurements, the concurrently measured SST and the derived surface saturation specific humidity (assuming 98% saturated) and the corresponding M are also included in these figures. The SST was measured from the R/V Sharp and had gone through extended data quality control (Alappattu et al., 2017). This combination of data from both the ship and the buoy provides the high vertical resolution data to illustrate the vertical structure of the atmosphere near the surface of the ocean.

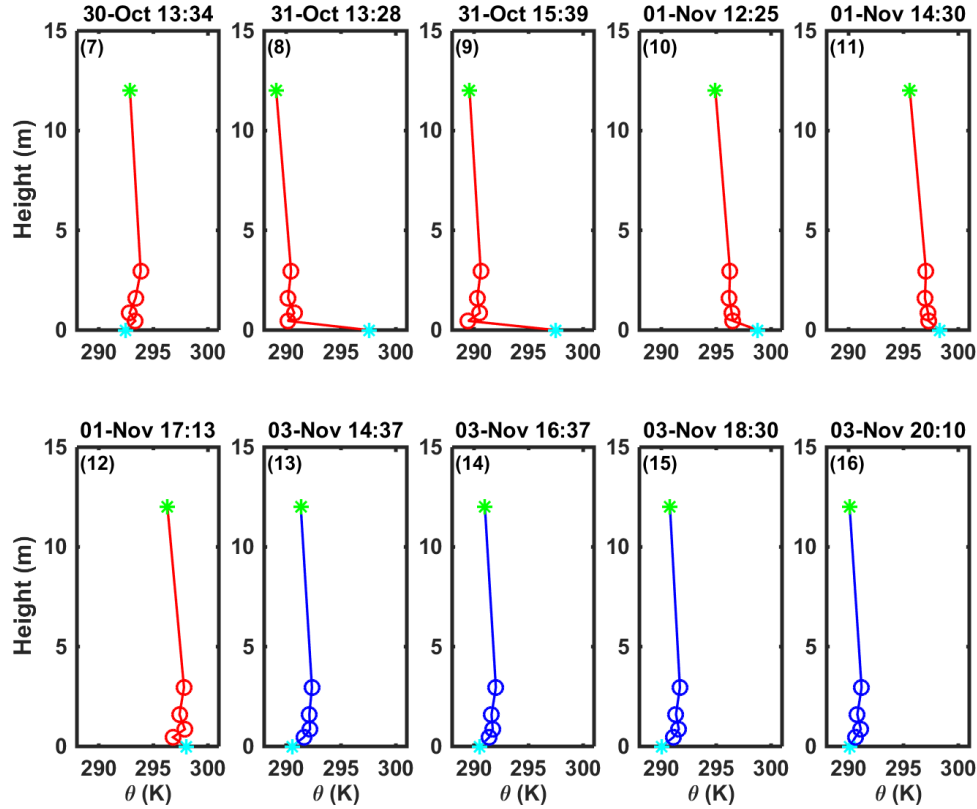


Figure 28. CASPER-East Deployments 7 - 16 Temperature Comparison.

Figure 28 shows the complex temperature variability with height in the near surface levels similar to those observed in CASPER-Pilot experiment (Figure 15b). First, we note the persistent decrease in potential temperature between the top of the buoy and the ship (see last column of Table 6). Table 6 shows that the temperature difference between these two levels is between 0.9 and 1.52 K within 9 m of vertical separation. This result is somewhat questionable due to its large magnitude. However, cross-examination of the data quality by comparing temperature measurements from redundant sensors at the same level, including temperature derived from the 3-D sonic measurements and an independent temperature probe, suggested that the measured temperature on the bow mast from the Rotronics probe was valid. Furthermore, comparisons with measurements from the tethered balloon and from CTV, to be

discussed later, seem to indicate such large difference is possible given that the MASFlux measurements are so close to the surface.

Table 6 and Figure 28 also revealed the extreme vertical gradients in θ near the surface in case of strong air-sea temperature difference captured on 31 October 2015. This extreme gradient was confined between 0.46 m and the surface and was not at all reflected in the layers above. In the case of deployment nine, the buoy temperature at the lowest level seems to be the lowest of all four levels, which is most puzzling. Specific humidity (Figure 29), on the other hand, shows expected vertical gradient from the surface through the buoy at various altitude and to the ship mast, particularly over the warm water of the Gulf Stream (deployment 7 – 12). The near-surface gradient over the stable shelf region is not apparent from the MASFlux buoy measurements. The M -profiles in Figure 30 mainly reflect the variation in specific humidity as water vapor pressure is the major contributor to M .

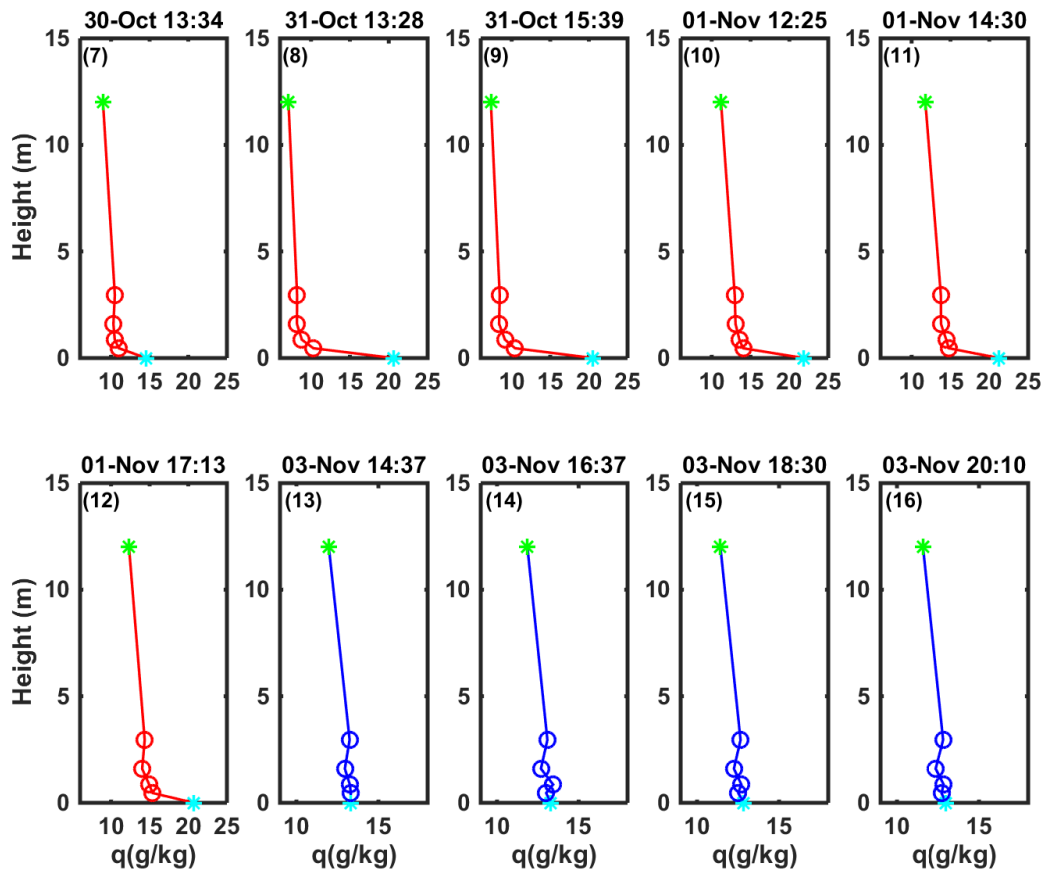


Figure 29. CASPER-East Deployments 7 - 16 Specific Humidity Comparison.

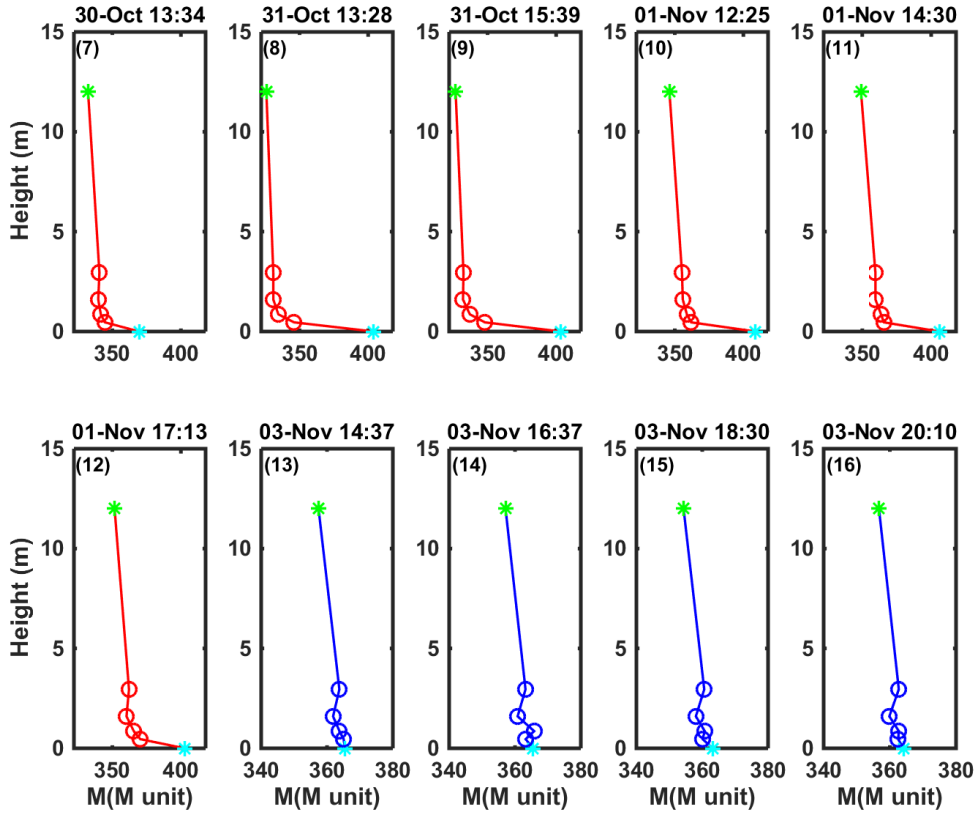


Figure 30. CASPER-East Deployments 7 – 16 Modified Refractivity Comparison.

Turbulent momentum and sensible heat fluxes were also obtained during CASPER-East on the R/V Sharp bow mast at 12 m and on MASFlux at 3.43 m (Figures 31– 32). Here, negative heat flux indicates sensible heat transport from the air into the ocean, which is the case in deployment 7, 13, 14, 15 and the ship SHF from 16. These are the stable cases as identified by the difference between SST and the top level temperature measurements on the MASFlux buoy (Table 6). For deployment 16, the sign of SHF at both buoy and ship levels are inconsistent with their respective thermal stability indicated by ASTD (Table 6). It should be pointed out that all these stable cases, especially deployment 13 – 16 over the shelf break has very small heat fluxes. The relative error in flux calculation for these cases should be large. In contrast, positive heat fluxes near the surface are substantially larger over the warm water of the GS resulting in

SHF in the range of $20 - 90 \text{ W m}^{-2}$. We have confidence in the fluxes in these cases. Meanwhile, significant decreases in SHF from the buoy level to the ship level are observed over the GS. Such flux convergence in the lowest 12 m of the atmosphere validate the MOST assumption of constant flux layer and should contribute to measurable heating of the layer. It is even more puzzling how the strong temperature gradient can be maintained in case of such strong turbulence fluxes. Future analyses should look into the length scales of turbulence mixing in these cases to understand the nature of momentum and scalar mixing in these extreme stability cases. More measurements with fine vertical resolution near the surface should also benefit.

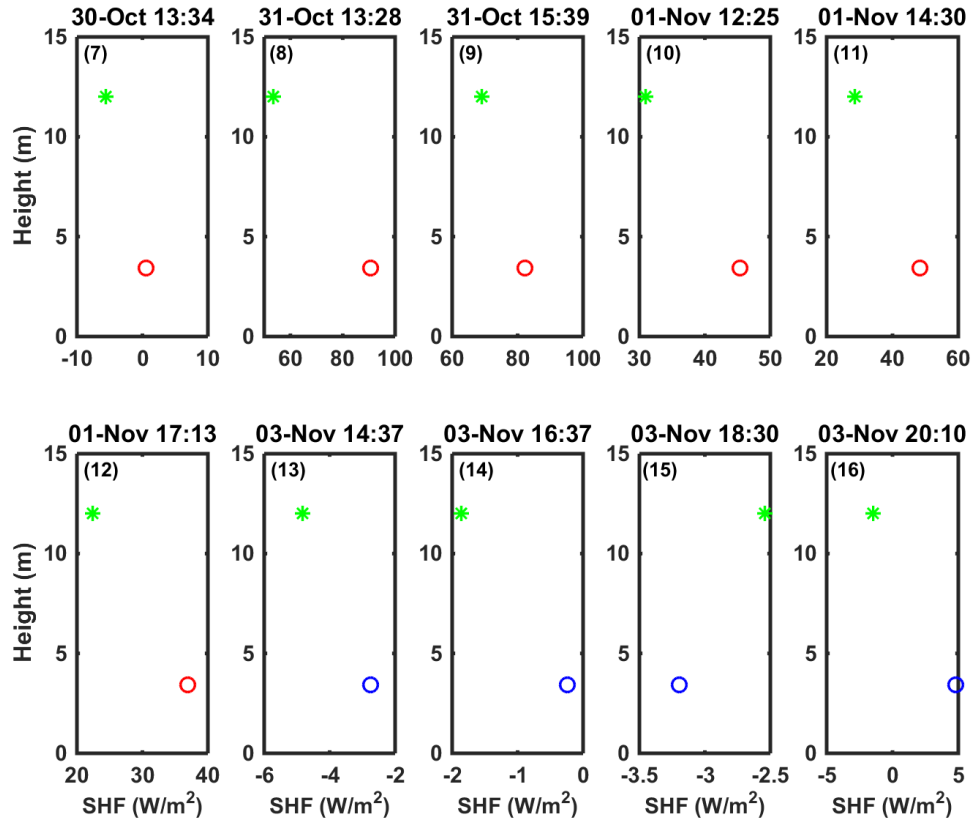


Figure 31. CASPER-East Deployments 7 – 16 Sensible Heat Flux Comparison.

The surface layer frictional velocity, u_* , is shown in Figure 32 to represent momentum flux. Again, significant flux convergence/divergence is observed in nearly all cases between the ship level and the buoy level. However, the connection between the sign of the divergence with mean wind speed or thermal stability is not clear. The buoy measurements may be in the wave boundary layer. Future work should separate the momentum fluxes in to wind sea and swell driven component, which may suggest connections with the wave factors.

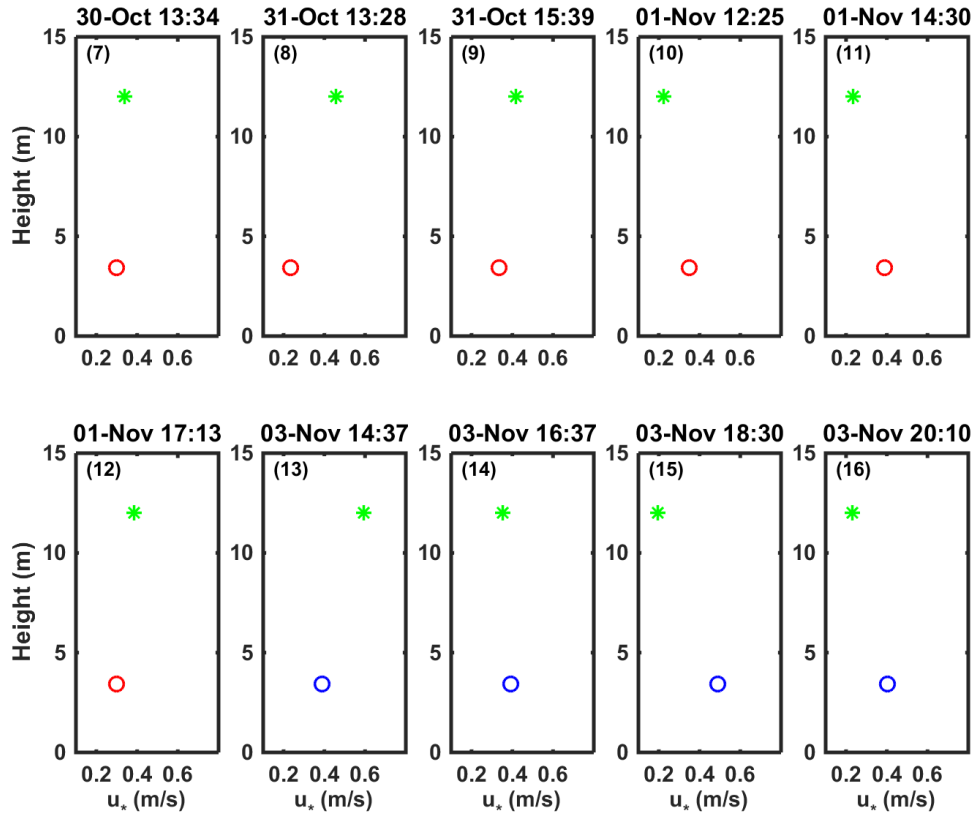


Figure 32. Frictional Velocity in CASPER-East Deployments 7 – 16.

2. Ship and MASFlux Measurements vs. MOST Profiles over the Gulf Stream

Discussions in the previous section suggested interesting vertical variations of wind and scalars over the Gulf Stream. The presence of the near-surface wind jet and the

complex temperature profiles clearly indicate deviations from the MOST depicted vertical profiles. In this section, an attempt is made to quantify such deviations using measurements over the Gulf Stream (deployments 7 through 12). This discussion is structured similarly as in Chapter IV Section A.2 for results from CASPER-Pilot. Figures 33 through 36 show potential temperature (θ), specific humidity, wind speed, and modified refractivity as measured from the MASFlux buoy and the bow mast of R/V Sharp. Instrument heights and specifications are described in Chapter III. The COARE algorithm was used with inputs from levels one through four from the MASFlux and ship mast at each individual level. The observed ship data and COARE model output are in red. Observed buoy data and COARE model output are in black. The EDH is marked by a “x” on each COARE output on the modified refractivity plots with the values given in the legends.

Figures 33 through 36 are capable of revealing the details of the observed vertical variability in all variables with a zoomed in axis range when the corresponding sea surface quantities are not included. The complex vertical structure in potential temperature from surface to the ship level can be seen clearly in nearly all subplots of Figure 33. The near surface wind jets can also be easily identified on the plots of the mean wind speed (Figure 35) while the specific humidity and the M profiles reveals the near-surface gradients. Note these gradients are seen in the mean profiles averaged over a time period of 50 to 70 minutes and hence are statistically significant. All these gradients were discussed in the previous section. The deviation of the MOST profiles from these measurements can be identified in these figures. When the MOST profiles with input from different levels collapse together, it is indicative that the measurements follow MOST description. This occurred on Legs 10 and 11 for the MASFlux data only. These two cases were two of the three cases with mean buoy speed (at level three) exceeding 8 m s^{-1} (Table 6). They are also two of the four cases where the ASTD exceeded 2 K. These results suggest that MOST is adequate for marine atmospheric surface layers near the surface when turbulence was generated by both strong buoyancy and shear. However, there are clear differences between the buoy and the ship results, suggesting different turbulence forcing mechanisms at different levels of the lower 12 m

of the marine surface layer. Leg 12 is the high wind but low thermal forcing case while legs eight and nice are the low wind but strong thermal forcing cases, all indicate large deviation of the MOST profiles from the observations in the lowest 3 m. Leg seven is the only stably stratified case over the cold region of the GS; wind speed at MASFlux level 3 during this leg averaged to 5.9 m s^{-1} . The errors in MOST profiles when compared to observations are apparent in this case as well.

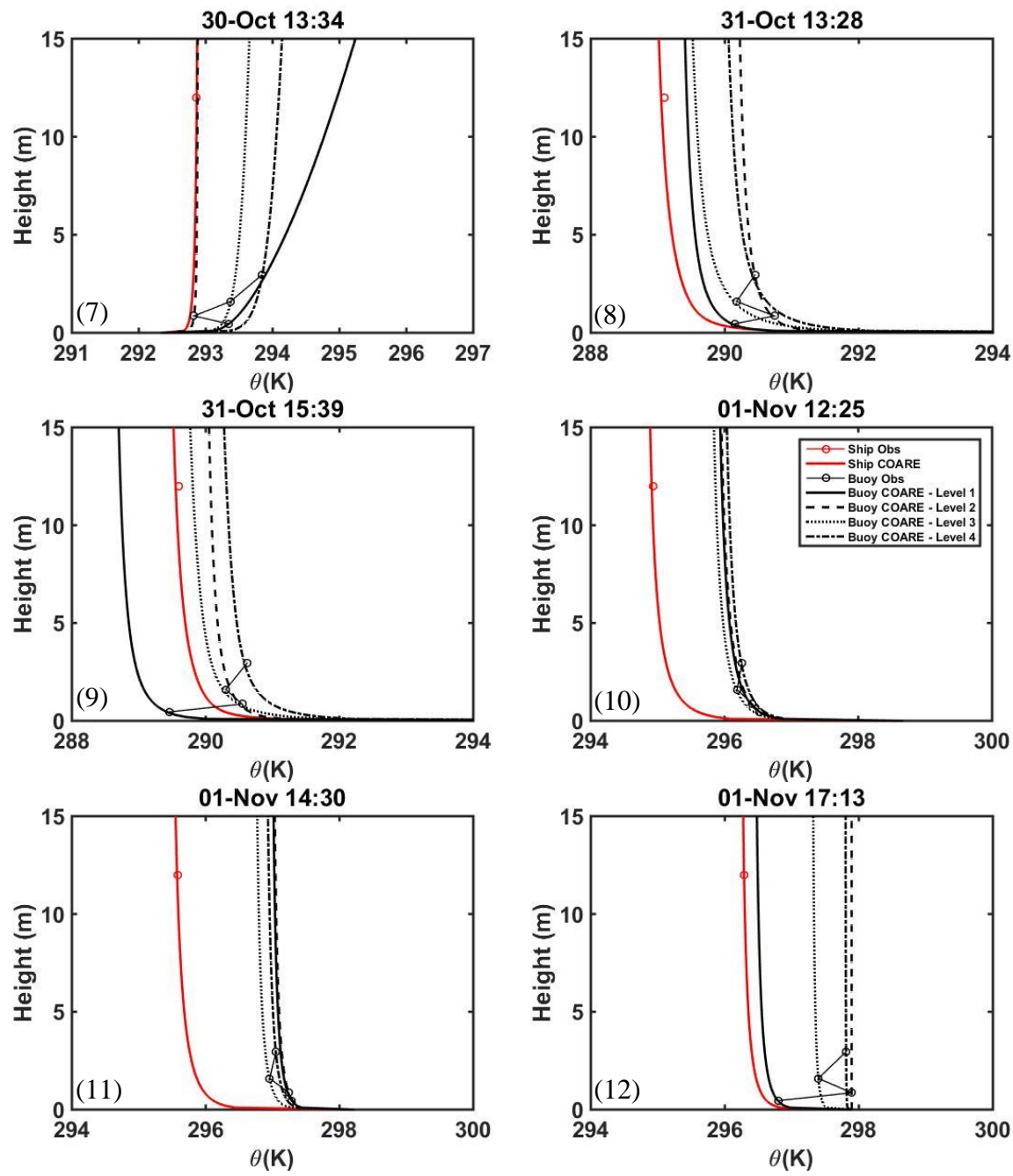


Figure 33. Potential Temperature for CASPER-East Observations and COARE Model Output for Deployments 7 – 12.

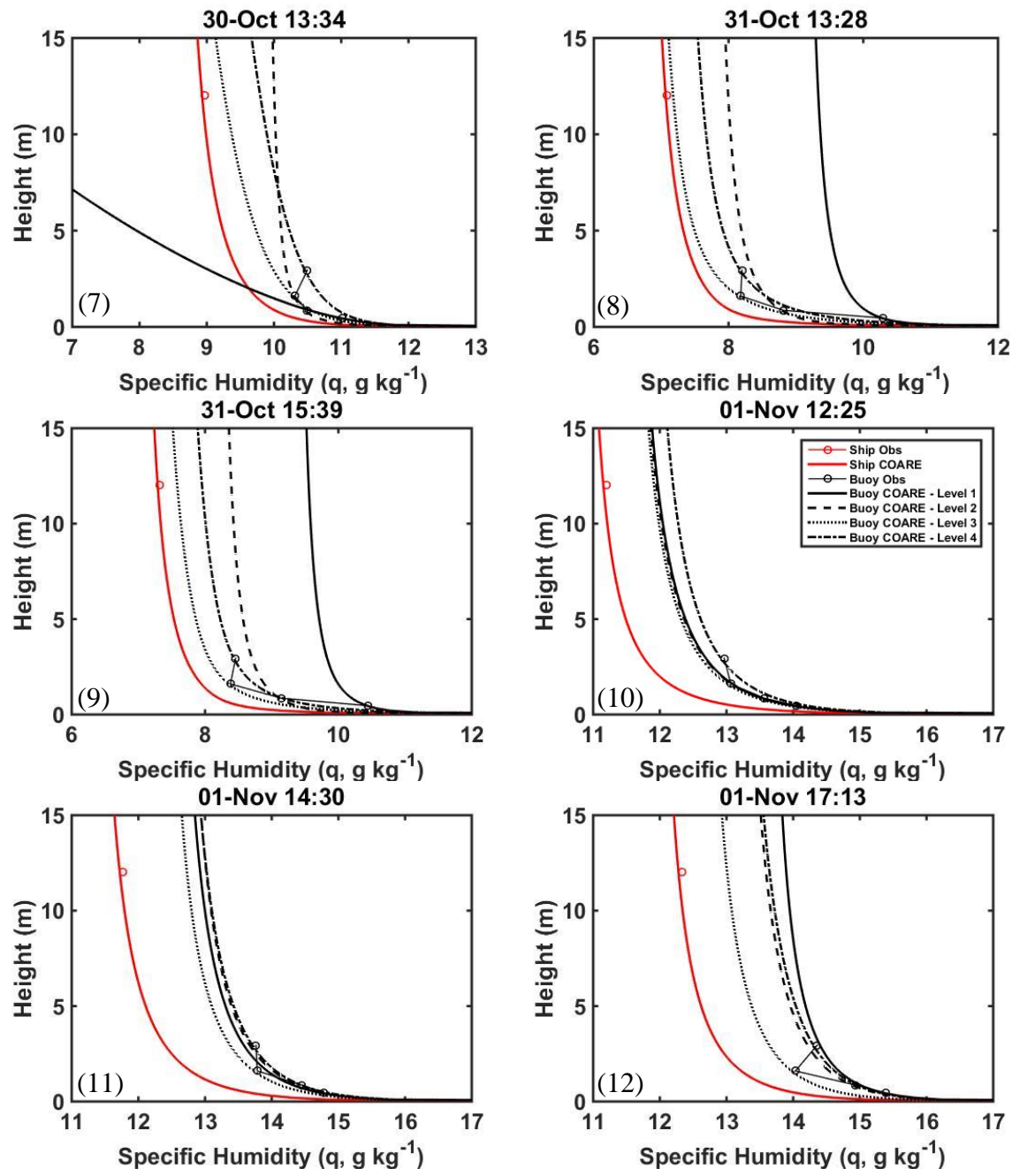


Figure 34. Specific Humidity for CASPER-East Observations and COARE Model Output for Deployments 7 – 12.

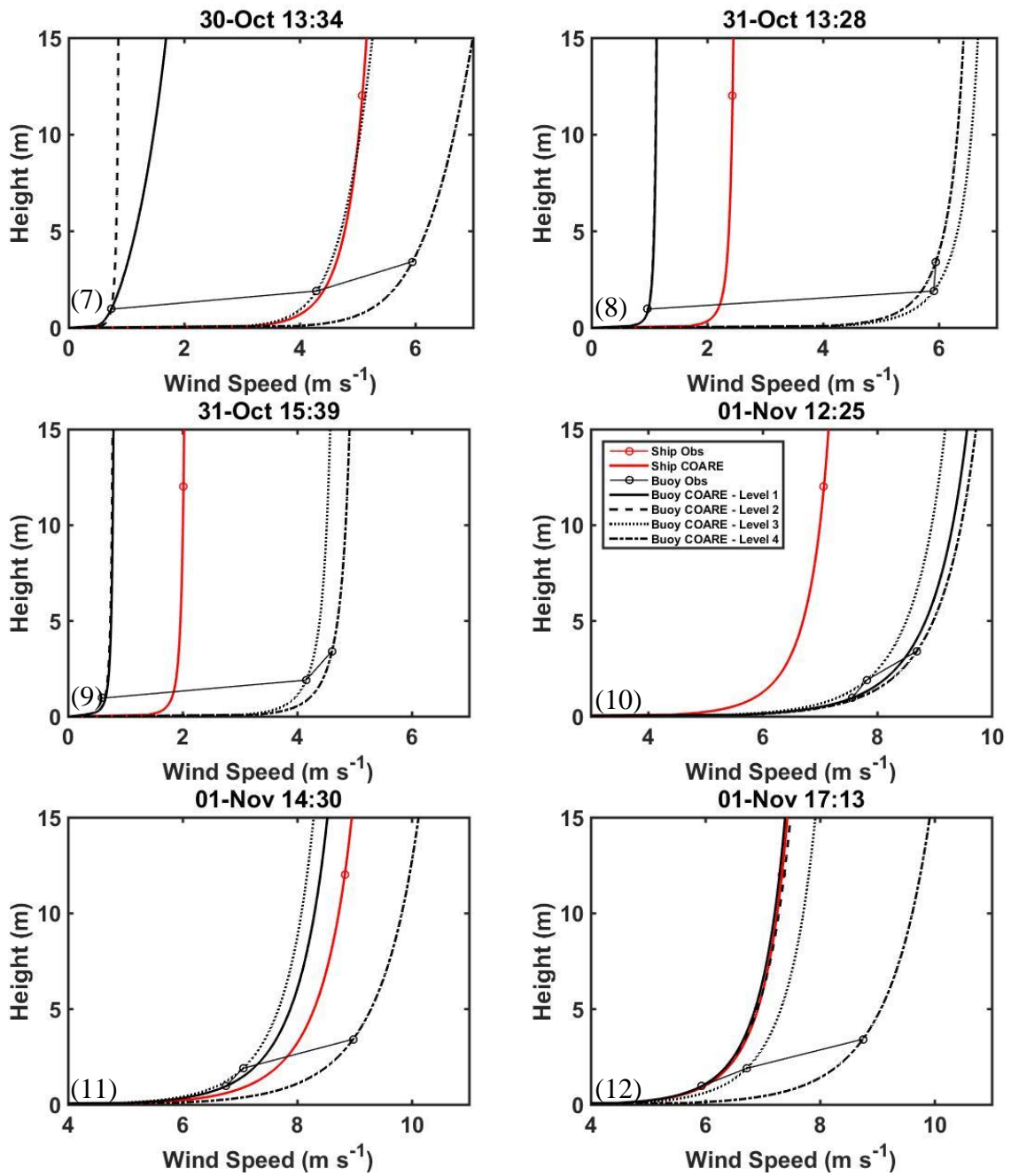


Figure 35. Wind Speed for CASPER-East Observations and COARE Model Output for Deployments 7 – 12.

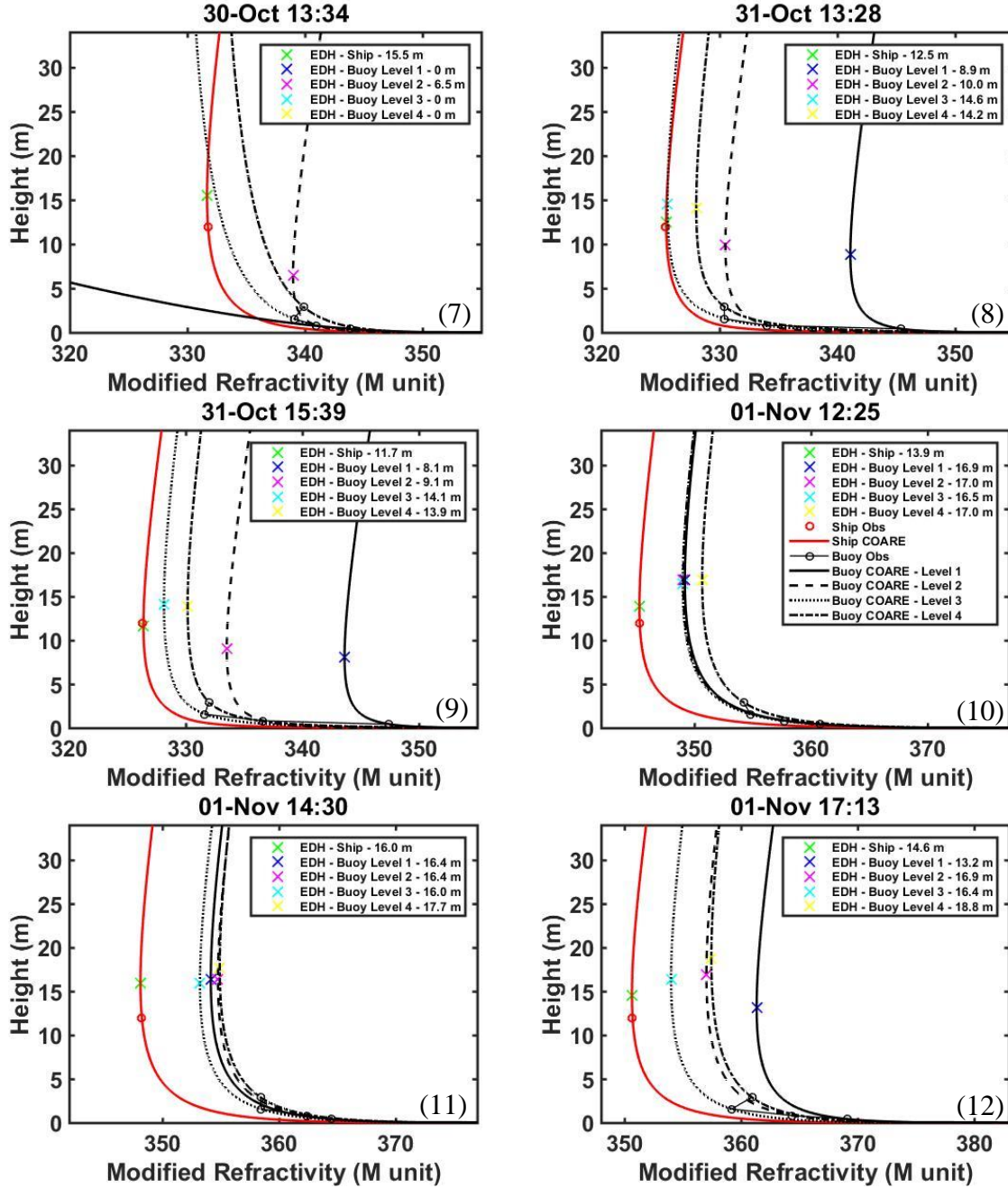


Figure 36. Modified Refractivity for CASPER-East Observations and COARE Model Output for Deployments 7 – 12.

To better analyze the results shown in Figures 33 through 36, error analyses for the derived COARE profiles are further calculated for each input levels. Observation and model error was again calculated in the method described in Chapter IV, Section 1. For CASPER-East, mean measurements were collected at 0.46 m, 0.86 m, 1.60 m, and 2.95

m for temperature and humidity and 0.97 m, 1.90 m, 3.43 m for wind speed. The COARE algorithm produces data points every 0.1 m. To compare the bulk measurements with the predicted profile, the observed 0.46 m measurement was compared with the 0.5 m calculation, the 0.86 m observed measurement was compared with the 0.9 m calculation, the 1.60 m observed measurement was compared with the 1.6 m calculation and the 2.95 m bulk measurement was compared with the 3.0 m calculation. Similarly, for wind speed the 0.97 m measurement was compared with the 1.0 m calculation, the 1.90 m measurement was compared with the 1.9 m calculation, and the 3.43 m measurement was compared with the 3.4 m calculation. The numerical error values for each input level, one through four for the MASFlux buoy and ship level are shown in Table 7 through 11.

Table 7. CASPER-East COARE Profile Errors with Level One Input.

	Leg 8	Leg 8	Leg 9	Leg 10	Leg 11	Leg 12
θ (K)						
Level 2	0.6633	0.8169	1.3210	0.0332	0.0217	1.1761
Level 3	0.2773	0.3938	1.2225	0.0820	0.2155	0.7419
Level 4	0.0609	0.8020	1.6760	0.1051	0.0671	1.2141
Ship	2.1002	0.3342	0.8676	1.0327	1.4440	0.1993
Specific Humidity (g kg^{-1})						
Level 2	0.0051	1.2067	1.0446	0.0663	0.1612	0.0397
Level 3	0.4005	1.6424	1.6168	0.0250	0.1513	0.6531
Level 4	1.4913	1.4362	1.3681	0.2842	0.1913	0.0352
Ship	3.7779	2.2430	2.2404	0.7729	1.1594	1.5662
Wind Speed (m s^{-1})						
Level 2	3.4278	4.8826	3.4547	0.2920	0.1747	0.3919
Level 3	4.9296	4.8862	3.8736	0.1337	1.3494	2.0888
Ship	3.5194	1.3152	1.2230	2.3624	0.4257	0.0428
Modified Refractivity (M units)						
Level 2	0.6944	9.9097	9.4935	0.0772	0.7048	2.4862
Level 3	2.9499	12.4099	13.4095	0.3444	1.0156	5.8885
Level 4	10.1906	11.4756	12.2343	1.4962	1.0889	2.4444
Ship	28.5526	15.7673	17.4207	4.0754	6.0662	10.6597

Table 8. CASPER-East COARE Profile Errors with Level Two Input.

	Leg 7	Leg 8	Leg 9	Leg 10	Leg 11	Leg 12
θ (K)						
Level 1	0.5362	0.6872	1.1745	0.0118	0.0036	1.0997
Level 3	0.5267	0.3890	0.0715	0.0980	0.2314	0.4966
Level 4	0.9818	0.0062	0.3620	0.0882	0.0838	0.0845
Ship	0.0158	1.1506	0.4780	1.0510	1.4622	1.6004
Specific Humidity (g kg^{-1})						
Level 1	0.3976	1.2782	1.1115	0.1252	0.0300	0.1893
Level 3	0.0112	0.3663	0.5084	0.0088	0.2353	0.5055
Level 4	0.3153	0.1366	0.2399	0.3013	0.1038	0.1513
Ship	1.0392	0.9049	1.0805	0.7539	1.2521	1.2626
Wind Speed (m s^{-1})						
Level 2	3.5170	4.8860	3.4671	0.2921	0.1749	0.3817
Level 3	5.1459	4.8901	3.8876	0.1336	1.3488	2.0627
Ship	4.2296	1.3200	1.2395	2.3628	0.4239	0.0404
Modified Refractivity (M units)						
Level 1	1.7564	9.8900	9.4641	0.4955	0.1524	2.7239
Level 3	0.8808	2.2484	3.6864	0.2208	1.5676	2.9780
Level 4	0.6007	1.1257	2.3439	1.6273	0.5139	0.8030
Ship	7.4422	5.1135	7.2668	3.9295	6.6749	6.5022

Table 9. CASPER-East COARE Profile Errors with Level Three Input.

	Leg 7	Leg 8	Leg 9	Leg 10	Leg 11	Leg 12
θ (K)						
Level 1	0.0929	0.5804	1.2867	0.1106	0.2095	0.6537
Level 2	0.4902	0.3365	0.0704	0.1219	0.2314	0.4702
Level 4	0.3931	0.5531	0.5359	0.1993	0.1615	0.4374
Ship	0.7577	0.4622	0.2125	0.9375	1.2013	1.0332
Specific Humidity (g kg^{-1})						
Level 1	0.2213	1.1325	1.2509	0.1795	0.2946	0.7087
Level 2	0.0510	0.2019	0.4169	0.1385	0.3589	0.6237
Level 4	0.5112	0.4483	0.4068	0.3554	0.3980	0.7266
Ship	0.3014	0.0884	0.2681	0.7160	0.9604	0.6788
Wind Speed (m s^{-1})						
Level 1	3.2895	4.6335	3.3644	0.2444	0.1398	0.3713
Level 3	1.4133	0.2199	0.3012	0.4541	1.5437	1.6643
Ship	0.0524	4.1830	2.5345	1.9896	0.6582	0.4689
Modified Refractivity (M units)						
Level 1	1.1451	8.6908	10.5893	0.6913	1.2771	5.4866
Level 2	0.1029	0.7586	2.6601	0.4021	1.6829	3.0520
Level 4	2.7616	2.2948	2.0100	1.8106	2.1086	3.8512
Ship	1.3274	0.2050	1.8427	3.8550	5.1104	3.4471

Table 10. CASPER-East COARE Profile Errors with Level Four Input.

	Leg 7	Leg 8	Leg 9	Leg 10	Leg 11	Leg 12
θ (K)						
Level 1	0.2434	1.0310	1.7720	0.0523	0.0753	1.0264
Level 2	0.8473	0.1358	0.4224	0.0507	0.0881	0.0744
Level 3	0.3834	0.4497	0.4547	0.1706	0.1470	0.4172
Ship	1.2306	0.9949	0.7172	1.1312	1.3617	1.5114
Specific Humidity (g kg^{-1})						
Level 1	0.1419	0.7665	0.8451	0.0877	0.0026	0.1356
Level 2	0.4496	0.1808	0.0177	0.1428	0.0400	0.0119
Level 3	0.3979	0.3719	0.3611	0.2428	0.2797	0.5864
Ship	0.8307	0.5213	0.6405	1.0027	1.2570	1.3157
Wind Speed (m s^{-1})						
Level 1	4.4999	4.4373	3.6262	0.1306	1.1592	1.7719
Level 2	1.3081	0.2130	0.2813	0.4083	1.4185	1.5289
Ship	1.7271	3.9376	2.8680	2.5138	1.1294	2.4142
Modified Refractivity (M units)						
Level 1	0.9222	6.6909	8.3582	0.9010	0.5502	2.1933
Level 2	2.1828	1.3481	0.4693	1.2771	0.2798	0.4726
Level 3	2.4857	2.2591	2.1700	1.7532	2.0511	3.6977
Ship	4.3766	2.6385	3.8661	5.5589	6.9117	7.0463

Table 11. CASPER-East COARE Profile Errors with Ship Level Input.

	Leg 7	Leg 8	Leg 9	Leg 10	Leg 11	Leg 12
θ (K)						
Level 1	0.5995	0.3025	0.7914	0.9541	1.1911	0.1827
Level 2	0.0539	1.1044	0.4655	1.0067	1.2666	1.3550
Level 3	0.5773	0.6974	0.3606	0.9260	1.0880	0.9287
Leve 4	1.0209	1.1237	0.8201	1.1380	1.2937	1.4082
Specific Humidity (g kg^{-1})						
Level 1	0.7487	1.9505	1.9656	1.0148	1.1732	1.4161
Level 2	0.4953	0.8054	0.9571	1.0035	1.2750	1.3616
Level 3	0.5872	0.4249	0.4362	0.9208	1.0003	0.8123
Leve 4	1.0484	0.6880	0.7522	1.2116	1.3733	1.4904
Wind Speed (m s^{-1})						
Level 1	3.4133	1.2326	1.2163	1.6951	0.3874	0.0679
Level 2	0.1137	3.6361	2.2729	1.5931	0.5652	0.3414
Leve 3	1.3194	3.6117	2.6744	2.1715	0.9417	2.0391
Modified Refractivity (M units)						
Level 1	4.1076	13.3085	15.0168	5.0948	5.7285	9.0005
Level 2	3.1511	4.0317	5.9984	4.9700	6.3305	6.7142
Level 3	3.0543	1.9250	2.4680	4.5816	4.8060	3.7429
Leve 4	5.6455	3.2623	4.1255	6.2858	7.0592	7.5931

The mean error for each variable at each level was calculated and is shown in Tables 12 through 15. Mean wind speed (MASFlux levels 1 – 4, and ship level) and air sea temperature difference (ASTD) for each leg are displayed for reference.

Table 12. CASPER-East Mean Error of COARE Profiles for θ (K) for All Input Levels.

	Leg 7	Leg 8	Leg 9	Leg 10	Leg 11	Leg 12
Mean WS	5.1	2.4	2.0	7.1	8.8	7.3
ASTD	-1.37	7.10	6.89	2.52	1.28	0.21
Level 1	0.7759	0.5868	1.2718	0.3132	0.4371	0.8329
Level 2	0.5152	0.5582	0.5215	0.3123	0.4452	0.8203
Level 3	0.4335	0.4830	0.5264	0.3423	0.4509	0.6486
Level 4	0.6762	0.6529	0.8416	0.3512	0.4180	0.7574
Ship	0.5629	0.8070	0.6094	1.0062	1.2098	0.9686

The input data levels are given in the left column.

Table 13. CASPER-East Mean Error of COARE Profiles for Specific Humidity (g kg^{-1}) for All Input Levels.

	Leg 7	Leg 8	Leg 9	Leg 10	Leg 11	Leg 12
Mean WS	5.1	2.4	2.0	7.1	8.8	7.3
ASTD	-1.37	7.10	6.89	2.52	1.28	0.21
Level 1	1.4187	1.6321	1.5675	0.2871	0.4158	0.5736
Level 2	0.4409	0.6715	0.7350	0.2973	0.4053	0.5272
Level 3	0.2713	0.4678	0.5857	0.3473	0.5030	0.6844
Level 4	0.4550	0.4601	0.4661	0.3690	0.3948	0.5124
Ship	0.7199	0.9672	1.0278	1.0377	1.2054	1.2701

The input data levels are given in the left column.

Table 14. CASPER-East Mean Error of COARE Profiles for Wind Speed (m s^{-1}) for All Input Levels.

	Leg 7	Leg 8	Leg 9	Leg 10	Leg 11	Leg 12
Mean WS	5.1	2.4	2.0	7.1	8.8	7.3
ASTD	-1.37	7.10	6.89	2.52	1.28	0.21
Level 1	3.9589	3.6947	2.8504	0.9294	0.6499	0.8412
Level 2	4.2975	3.6987	2.8647	0.9295	0.6492	0.8283
Level 3	1.5851	3.0121	2.0667	0.8960	0.7806	0.8348
Level 4	2.5117	2.8626	2.2585	1.0176	1.2357	1.9050
Ship	1.6155	2.8268	2.0545	1.8199	0.6314	0.8161

The input data levels are given in the left column.

Table 15. CASPER-East Mean Error of COARE Profiles for Modified Refractivity (M Units) for All Input Levels.

	Leg 7	Leg 8	Leg 9	Leg 10	Leg 11	Leg 12
Mean WS	5.1	2.4	2.0	7.1	8.8	7.3
ASTD	-1.37	7.10	6.89	2.52	1.28	0.21
Level 1	10.5969	12.3906	13.1395	1.4983	2.2189	5.3697
Level 2	2.6700	4.5944	5.6903	1.5683	2.2272	3.2518
Level 3	1.3343	2.9873	4.2755	1.6898	2.5447	3.9592
Level 4	2.4918	3.2341	3.7159	2.3725	2.4482	3.3525
Ship	3.9896	5.6319	6.9022	5.2330	5.9811	6.7627

The input data levels are given in the left column.

To better visualize the errors between the observed data and COARE output, the results in Table 12 through 15 are plotted in Figure 37, where the mean error for each variable is plotted against the height of the measurement. For the errors in wind speed, there is a clear separation, where the large errors at all levels are associated with the cases of weak wind (legs seven, eight, and nine). This is also seen in errors of specific humidity and somewhat in potential temperature with the exception of leg 12 where thermal stability is weak compared to the other two moderation wind cases (legs 10 and 11). In these three cases the error for specific humidity and modified refractivity also dramatically decrease once the height is above the lowest measurement level. Interestingly, the stable stratification case does not stand out with larger error compared to others as opposed to the common notion that stable stratification is more problematic. As discussed earlier, legs 10 and 11 show the smallest errors within the buoy levels in all variables.

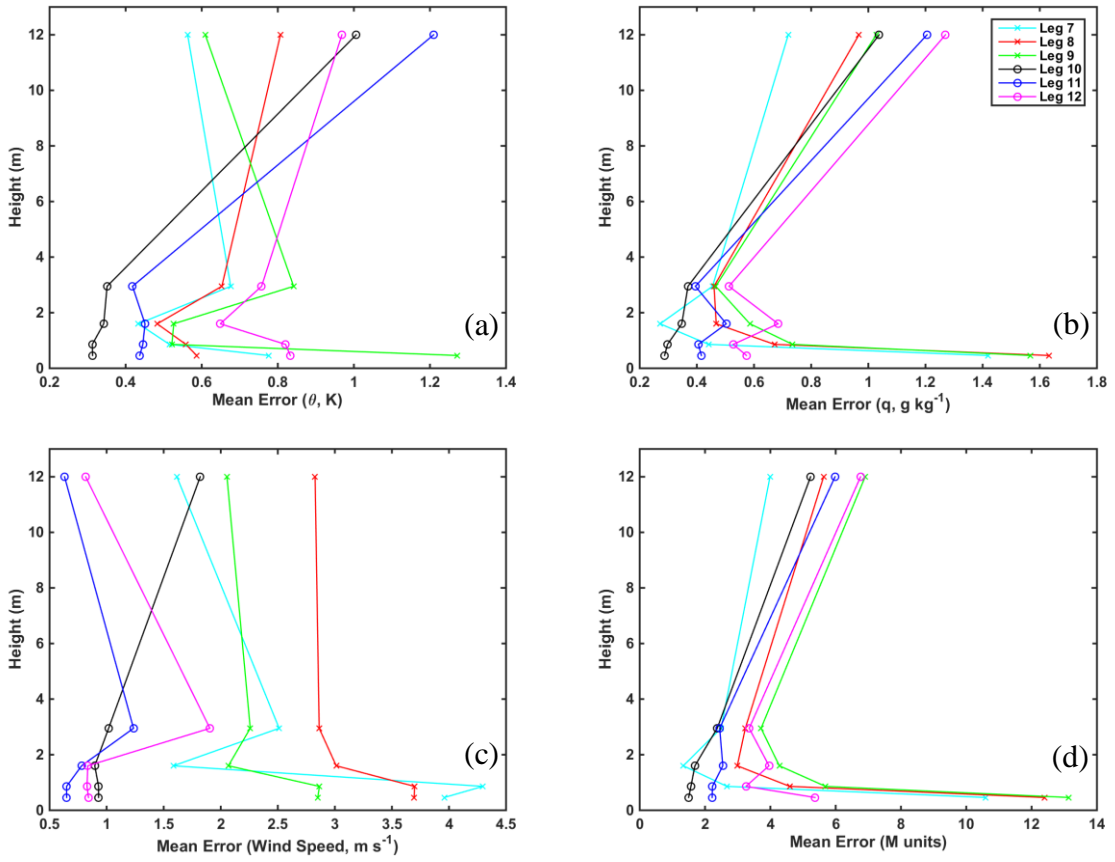


Figure 37. CASPER-East Error for each Variable Plotted Versus Height. (a) θ , (b) Specific Humidity, (c) Wind Speed, (d) Modified Refractivity

Errors at the ship level are significantly variable and large in both temperature and particularly in specific humidity. It should be noted that the MASFlux buoy was tethered to R/V Sharp and that the lateral separation between the MASFlux buoy measurements and the R/V Sharp mast measurements were very small and negligible. The measurements of temperature at the ship level were cross-checked with redundant sensors and no significant measurement errors were detected.

The large errors at the ship level translate to large errors in the modified refractivity (Figure 37d) and will inevitably affect the properties of the identified EDH. This result is alarming when the input from a low level platform is used in the evaporation duct model. Table 16 shows the evaporation duct height, its mean, and

standard deviation from the six GS cases when inputs to the ED model were from different levels. Mean wind and air-sea temperature difference are again shown in the table for reference.

Table 16. CASPER-East Evaporation Duct Height.

Evaporation Duct Height						
	Leg 7	Leg 8	Leg 9	Leg 10	Leg 11	Leg 12
Mean WS	5.1	2.4	2.0	7.1	8.8	7.3
ASTD	-1.37	7.10	6.89	2.52	1.28	0.21
Level 1	NA	8.9	8.1	16.9	16.4	13.2
Level 2	6.5	10	9.1	17.0	16.4	16.9
Level 3	NA	14.6	14.1	16.5	16	16.4
Level 4	NA	14.2	13.9	17.0	17.7	18.8
Ship	15.5	12.5	11.7	13.9	16.0	14.6
Mean	11	12.04	11.38	16.26	16.5	15.98
Std.	6.3400	2.5225	2.7298	1.3353	0.7000	2.1568

Legs 10 and 11, the unstable cases with moderate wind, produce an average duct height just above 16 meters and have relatively lower variability using measurement input from different levels. Some input in the stable case did not produce an evaporation duct, while the low wind or the weak stability case (leg 12) all show a moderate level of variabilities. The EDH in these cases are then sensitive to the input levels.

3. Vertical Profiles from Multiple Platform Measurements

The added value of the MASFlux buoys can be further seen when combining data from other platforms which was concurrently collected during CASPER-East. Figure 39 shows an example of temperature and specific humidity profiles from all sensors measured over the Gulf Stream on 1 November, 2015. The combined SST distribution along the CTV path and during the MASFlux deployments are shown in Figure 38. The SST data from the different sources smoothly, providing the confidence in the SST calibration on both platforms (Alappattu et al., 2017).

The MASFlux measurements in Figure 38 were from leg 12. The mean value (circle) and the variability during the entire measurement period are shown as the

magenta line. CTV measurements were made within 20 minutes within leg 12 timeframe. It made a descend sounding over the warm water region followed by the long leg heading northwest at ~12 m height. This constant level measurement provided the mean and turbulence along the path as well as SST variability shown in Figure 39. An ascend sounding was also made over the cold water region. CTV measurements from both soundings and the level leg are shown in Figure 39. Current measurements were also made from a tethered balloon system on the work boat of R/V Sharp. The measurements from the multiple ascend/descend soundings on the tethered balloon is also shown in Figure 39. Finally, the bow mast measurements from R/V Sharp are also given in this figure together with the ship mean SST and the CTV SST over the warm and cold regions. On Figure 39b, only the 98% of the saturation specific humidity at the ship mean SST are given at the surface to represent the specific humidity at the immediate surface.

Figure 39a shows the consistency among different platforms over the warm water region. The CTV SST is warmer than the ship SST, consistent with the SST distribution since the warm region was at the very beginning of the CTV leg. The unstable thermal stratification and the magnitude of the temperature from CTV, the ship bow mast, and the tethered balloon are all consistent with the ship temperature being slightly higher. The CTV temperature during the transit leg at 12 m shows the evolution of air temperature towards the cold water region, which is stably stratified as shown by the last ascend sounding of the CTV. It is also seen that the MASFlux measurements were able to reveal the complex temperature variability close to the surface, which is not possible from other platforms. The MASFlux measured mean temperature lies in between the tethered balloon temperature and SST, providing the gradients towards the surface. The role of the MASFlux measurements is better shown in specific profiles in Figure 39b where the tethered balloon measurements only had very few data points. The higher resolution for specific humidity is critical for accurately producing modified refractivity profiles.

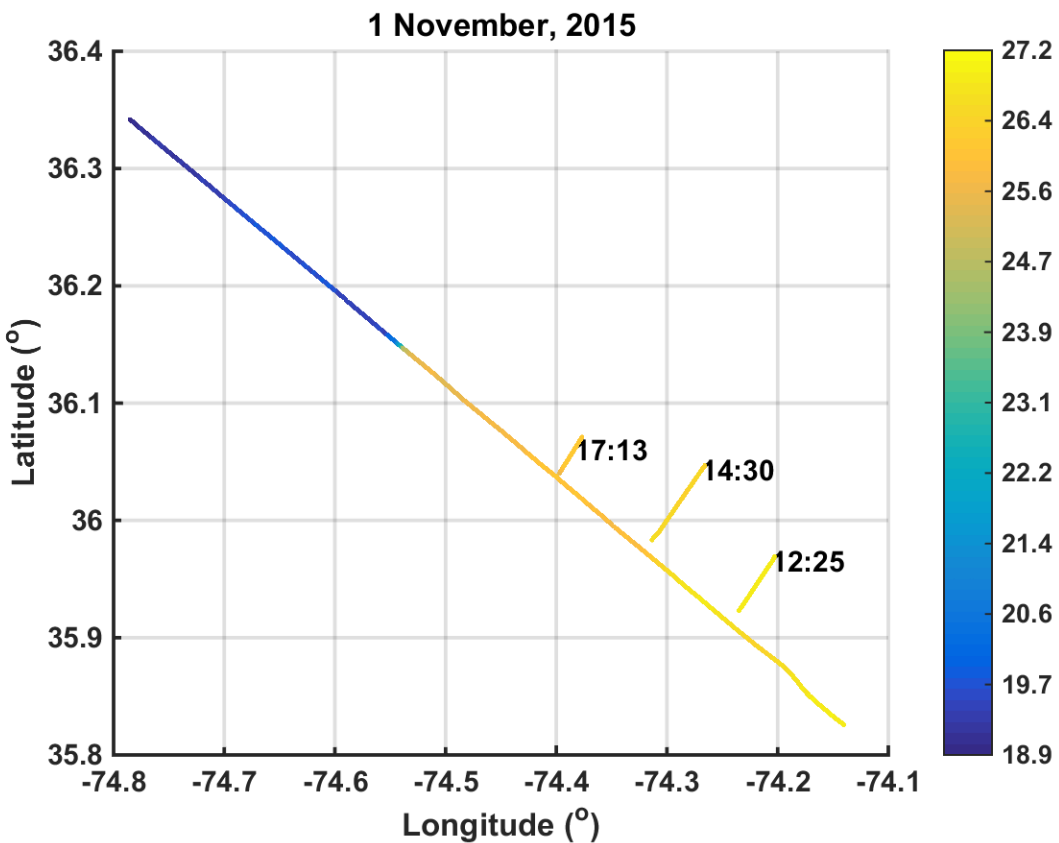


Figure 38. Measured Sea Surface Temperature from CTV (Long Northwest-Southeast Line) and from R/V Sharp (Short lines) on November 1, 2015.

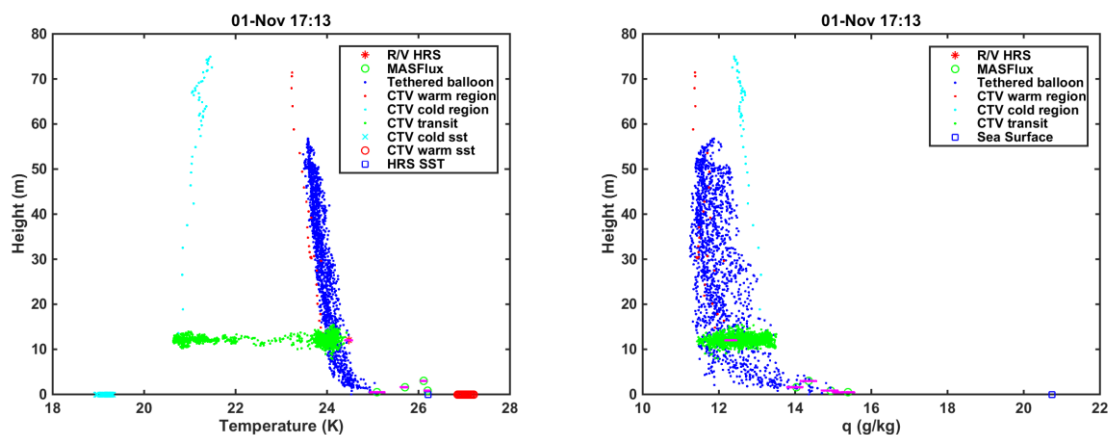


Figure 39. CASPER-East Leg 12 MASFlux Buoy, R/V HRS, Tethered Balloon and CTV Observations. (a) Temperature (b) Specific Humidity.

V. SUMMARY AND CONCLUSIONS

Measurements by the NPS MASFlux buoys were made on multiple days during CASPER-Pilot and CASPER-East field campaigns offshore of Moss Landing, CA and offshore of Duck, NC, respectively. During CASPER-Pilot experiment, 30-hour long measurements were made between 26 – 27 April, 2015 during a period of variable wind and thermal stability. This case showed the value of continued measurements at a fixed location allowing in-depth analyses of the temporal variation of mean and turbulent statistics at multiple levels near the surface. Such measurements so close to the surface are otherwise not available without the MASFlux buoy. This case was separated into three time periods: a high wind stable stratification period, a low wind unstable period, and a low wind stable period. All stabilities were defined based on ASTD where the SST was corrected for cool skin effect based on adjustment of the COARE parameterized surface sensible heat flux in comparison with the SHF derived directly from the high-rate measurements by the 3-D sonic anemometer. The MASFlux buoy measurements at multiple levels within the first 3.5 m above the ocean surface revealed the strong vertical gradient in mean wind, especially during the high wind conditions. However, the temperature and humidity profiles show rather complex vertical structure not expected by Monin-Obukhov Similarity Theory (MOST).

An error analysis between the COARE and the observed measurements was completed to better quantify the validity of COARE (and hence MOST) for the marine surface layer when the input levels are close to the surface. Such deviations are most significant in stable stratifications and also substantial in low wind convective cases. In these cases, the largest deviations are found when the measurements below one meter are used as input to the model. Above one meter the model output produced similar error, regardless of the input for the COARE model.

Concurrent measurements from the bow mast of R/V Sharp and the MASFlux buoy were made during 16 deployments of the MASFlux buoy over the Gulf Stream and the continental shelf region during CASPER-East. These measurements extended the MASFlux measurements to the ship bow mast level at 12 m. The analyses here focused

on these measurement periods. The vertical gradient in mean wind, temperature, specific humidity, and modified refractivity were examined in detail. One of the most significant results is the presence of the surface wind jet over the Gulf Stream region where currents are strong and SST's are warmer. These surface wind jets were not present over the shelf break region where SSTs are cooler and the current is weaker. It is suspected that this is just a result of the fast moving swell and the currents of about $2 - 3 \text{ m s}^{-1}$. However, further research is needed to make such conclusions. Similar to cases observed in the CASPER-Pilot experiment, the temperature profiles near the surface from CASPER-East also show complex vertical structure. Similar complex specific humidity profiles were also found over the shelf region in CASPER-East, although the specific humidity measurements over the Gulf Stream show smooth gradients between the surface and the surface layer above. As such, the MASFlux buoy measurements help to reveal the fine vertical structure of modified refractivity.

The two levels of turbulence flux measurements from the R/V Sharp and from MASFlux buoy were examined for co-located buoy and ship measurements. This comparison showed flux divergence in both momentum and sensible heat fluxes. This demonstrate, from another perspective, that the constant flux layer assumption of the surface layer is flawed.

Similar to the CASPER-Pilot analyses, the deviations of the MOST profiles from those observed were analyzed. It was found that the largest errors were introduced when the measurements as input to the ED model came from measurements at the lowest altitude. It was also found that the errors in the MOST profiles are the smallest during strong wind convective conditions.

Concurrent measurements of the MASFlux, the research vessel, the tethered balloon launched from a small boat, and the aircraft shows the added value of the MASFlux in providing the much needed mean wind and thermodynamic conditions within the lowest three meters above the surface.

LIST OF REFERENCES

- Alappattu, D. P., Q. Wang, R. Yamaguchi, R. J. Lind, M. Reynolds, and A. J. Christman, 2017: Warm layer and cool skin corrections for bulk water temperature measurements for air-sea interaction studies. *J. Geophys. Res. Oceans*, **122**, doi:10.1002/2017JC012688.
- Babin, S. M., G. D. Dockery, 2001: LKB-Based evaporation duct model comparison with buoy data. *J. Appl. Meteor.*, **41**, 434–446.
- Babin, S. M., G. S. Young, and J. A. Carton, 1997: A new model of the oceanic evaporation duct. *J. Appl. Meteor.*, **36**, 193–204.
- Beljaars, A. C. M., and A. A. M. Holtslag, 1991: Flux parameterization over land surfaces for atmospheric models. *J. Appl. Meteor.*, **30**, 327–341.
- Cheney, D. 2010: *Measurements of the Air-Sea Interface from an instrumented Small Buoy*, Naval Postgraduate School Thesis.
- Cook, J. and S. Burk, 1992: Potential refractivity as a similarity variable. *Bound.-Layer Meteor.*, **58**, 151–159.
- Donelan, Mark A., Fred W. Dobson, Stuart D. Smith, Robert J. Anderson, 1993: On the Dependence of Sea Surface Roughness on Wave Development. *J. Phys. Oceanogr.*, **23**, 2143–2149.
- Drennan, W. M., H. C. Graber, D. Hauser, and C. Quentin, 2003: On the wave age dependence of wind stress over pure wind seas. *J. Geophys. Res.*, **108**, 8062–8074.
- Edson, J., Palusziewicz T., Sandgathe, S., Vincent, L., Goodman, L., Curtin, T., Hollister, J., Colton, M., 1999: Coupled marine boundary layers and air-sea interaction initiative: combining process studies, simulations, and numerical Models. Office of Naval Research. 144.
- Fairall, C. W., E. F. Bradley, D. P. Rogers, J. B. Edson, and G. S. Young, 1996a: Bulk parameterization of air-sea fluxes in TOGA COARE. *J. Geophys. Res.*, **101**, 3747–3767.
- Fairall, C., E. Bradley, J. Hare, A. Grachev, and J. Edson, 2003: Bulk Parameterization of Air–Sea Fluxes: Updates and Verification for the COARE Algorithm. *J. Climate*, **16**, 571–591, doi: 10.1175/1520-0442(2003)
- Foken, T. 2006. 50 years of the Monin-Obukhov similarity theory. *Boundary-Layer Meteorology*. **119**, 431–447, doi:10.1007/s10546-006-9048-6.

- Frederickson, P.A., K. L. Davidson, K. D. Anderson, S. M. Doss-Hammel, D. Tsintikidis, 2003: Air-sea interaction processes observed from buoy and propagation measurements during the RED experiment. 5.
- Frederickson, Paul, 2010. "Software Design Description for the Navy Atmospheric Vertical Surface Layer Model (NAVSLaM) CSCI, Version 1.0"/ Prepared for the Naval Oceanographic Office, Systems Integration Division, 7 July 2010. 36 pages.
- Gallaudet T, 2016, Naval Oceanography Electromagnetic Maneuver Warfare Strategy. Accessed 17 January 2017. [Available online at http://www.navy.mil/submit/display.asp?story_id=93788].
- Grachev, A. A., C. W. Fairall, and E. F. Bradley, 2000: Convective profile constants revisited. *Bound.-Layer Meteor.*, 94, 495–515.
- Hill, R. J, 1989: Implications of Monin-Obukov Similarity Theory for Scalar Quantities. *Journal of the Atmospheric Sciences*, Vol. 46. No. 14, 2236–2244.
- Konstanzer, G. C., 1994: Sensitivity of AN/SPY-1B propagation to evaporation duct heights. JHU/APL Tech. Rep. F2F-94-U-4-012, 34 pp.
- Monin, A. S., A.M. Obukhov, 1954: Basic laws of turbulent mixing in the surface layer atmosphere. *Tr Akad. Nauk SSSR Geophiz Inst.* 24(151): 163–187
- Musson-Genon, L., S. Gauthier, and E. Bruth, 1992: A simple method to determine evaporation duct height in the sea surface boundary layer. *Radio Sci.*, **27**, 635–644.
- Paulus, R. A., 1985: Practical application of an evaporation duct model. *Radio Sci.*, **20**, 887–896.
- Paulus, R. A., 1989: Specification for Evaporation Duct Height Calculations. *NOSCTech Doc.* 1596, 4 pp [Available from National Technical Information Service, U.S. Department of Commerce, Technology Administration, 5285 Port Royal Road, Springfield, VA 22161.]
- Sullivan, P. P., J. B. Edson, T. Hristov, and J. C. McWilliams, 2008: Large-Eddy Simulations and Observations of Atmospheric Marine Boundary Layers above Nonequilibrium Surface Waves, *J. Atmos. Sci.*, **65**, 1225–1245.
- Turton, J. D., D. A. Bennetts, and S. F. G. Farmer, 1988: An introduction to radio ducting. *Meteor. Mag.*, **17**, 245–254
- Wang, Q. 2017: CASPER: Coupled air-sea processes and electromagnetic (EM) wave ducting research. *Bull. Amer. Meteor. Soc.* Submitted for Review.

Wang, Q. J.A. Kalogiros, S.R. Ramp, J.D. Paduan, G. Buzorius, H. Jonsson, 2011:
Wind stress curl and coastal upwelling in the area of Monterey Bay observed
during AOSN-II J. Phys. Oceanogr., 41, pp. 857-877, 10.1175/2010JPO4305.1

Zuniga, C. A., 2013: *Small Flux Buoy for Characterizing Marine Surface Layers*. M.S.
thesis, Dept. of Oceanography, Naval Postgraduate School.

THIS PAGE INTENTIONALLY LEFT BLANK

INITIAL DISTRIBUTION LIST

1. Defense Technical Information Center
Ft. Belvoir, Virginia
2. Dudley Knox Library
Naval Postgraduate School
Monterey, California